Processing and characterization of metallic glasses prepared by centrifugal atomization

Sasha Alejandra Cegarra Salges

Doctoral thesis by compendium of publications submitted to Universitat Politècnica de Catalunya in partial fulfilment of the requirements for the degree of Doctor of Philosophy

Thesis supervisor

Maria Dolores Riera Colom

Thesis supervisor

Jordi Pijuan

Manresa School of Engineering

March, 2024

UNIVERSITAT POLITÈCNICA DE CATALUNYA BARCELONATECH   DOCTORATS INDUSTRIALS   eurecat

To my dad, who taught me to think independently, even to his own disadvantage

Abstract

The production of metallic glasses presents an opportunity for advancing materials science and engineering applications, offering a unique combination of mechanical characteristics that traditional materials struggle to achieve. Conventional materials often exhibit a trade-off between strength and toughness, but metallic glasses, with their non-crystalline structure, offer a promising solution to this challenge.

Despite their potential, widespread adoption of metallic glasses has been impeded by challenges in the production of these materials. Achieving the necessary cooling rates for amorphization is a demanding task, as they are limited by the time-dependent process of heat transfer, which in turn limit the dimensions of the final product. However, these limitations can be overcome through the production of powder and their subsequent consolidation. In this sense, centrifugal atomization emerges as a promising technique for the production of metallic glasses. By subjecting molten metal to high centrifugal forces, this technique enables the generation of fine spherical droplets with cooling rates in the order of 10^2 to 10^5 K/s, promoting the formation of the desired non-crystalline structure.

This doctoral thesis focuses on characterizing the centrifugal atomization equipment designed at the *Fundació EURECAT*, with the primary objective of enhancing the cooling rates of atomized particles for metallic glass powder production. To carry out this comprehensive study, a complete theoretical and experimental research of the centrifugal atomization process is required. Theoretical efforts involve refining numerical models to understand the thermal behavior of atomized particles, significantly advancing our comprehension of cooling kinetics in this process of atomization. These models are validated through experimental methods to determine their applicability range, ensuring their utility in future investigations. On the experimental front, a systematic study is conducted on the effects of disk rotation speed, melt superheat temperature, and gas composition on the cooling rate of Al-Cu alloys and Al-based metallic glass forming alloys. Furthermore, additional techniques are explored, such as introducing an external gas source into the conventional centrifugal atomization process to investigate the impact of gas flow on the cooling rate of atomized Cu powder.

With the optimal adjustment of the atomization parameters, such as gas composition and disk speed, cooling rates of up to 10^5 K/s are achieved, with amorphous fractions of around 70% for particles smaller than 45 µm, and up to 50% in fractions of up to 125 µm in the Al-based metallic glass forming alloy of composition $Al_{86}Ni_8Y_{4,5}La_{1,5}$. The findings demonstrate that the centrifugal atomization process is well-suited for producing metallic glass powder tailored to meet the requirements of various industrial applications.

By conducting this study, this thesis lays the groundwork for the advancement of metallic glass powder production via centrifugal atomization. Future perspectives include further exploration in other alloy systems, such Fe-based glass forming alloys, making use of the acquired knowledge to continue improving production processes and expanding the application possibilities of these innovative materials across various industries.

Resumen

La producción de vidrios metálicos presenta una oportunidad en el avance de ciencia e ingeniería de materiales, ya que estos materiales presentan una combinación única de características mecánicas con respecto a los materiales tradicionales. Los materiales convencionales a menudo muestran un compromiso entre su resistencia y tenacidad, pero los vidrios metálicos, con su estructura no cristalina, ofrecen una solución prometedora a este obstáculo.

A pesar de su potencial, la adopción generalizada de vidrios metálicos ha sido limitada por los desafíos técnicos en la producción de estos materiales. Lograr las tasas de enfriamiento necesarias para la amorfización es una tarea exigente, ya que estas dependen del tiempo de transferencia de calor, que a su vez limita las dimensiones del producto final. Sin embargo, estos obstáculos pueden superarse mediante la producción de polvo para su posterior consolidación. En este sentido, la atomización centrífuga emerge como una técnica prometedora para la producción de vidrios metálicos. Al someter el metal fundido a altas fuerzas centrífugas, esta técnica permite la generación de gotas esféricas finas con tasas de enfriamiento del orden de 10^2 a 10^5 K/s, promoviendo la formación de la estructura no cristalina deseada.

Esta tesis doctoral se centra en caracterizar el equipo de atomización centrífuga diseñado en la *Fundació EURECAT*, con el objetivo principal de mejorar las tasas de enfriamiento de las partículas atomizadas para la producción de polvo de vidrio metálico. Para llevar a cabo este estudio se requiere una investigación exhaustiva tanto teórica como experimental del proceso de atomización centrífuga. En el ámbito teórico, se perfeccionan modelos numéricos con el fin de comprender el comportamiento térmico de las partículas atomizadas, lo que supone un avance significativo en la comprensión de la cinética de enfriamiento en este proceso de atomización. Estos modelos se validan con métodos experimentales para determinar su rango de aplicabilidad, garantizando así su utilidad en futuras investigaciones. A nivel experimental, se lleva a cabo un estudio sistemático de los efectos de la velocidad de rotación del disco, la temperatura de sobrecalentamiento del metal fundido y la composición del gas en la tasa de enfriamiento de las aleaciones de Al-Cu y las aleaciones en base a aluminio formadoras de vidrio metálico. Además, se exploran técnicas adicionales, como la introducción de una fuente de gas externa en el proceso convencional de atomización centrífuga, para investigar el impacto del flujo de gas en la tasa de enfriamiento del polvo de cobre atomizado.

Con el ajuste óptimo de los parámetros de atomización, como la composición del gas y la velocidad del disco, se logran alcanzar tasas de enfriamiento de hasta 10^5 K/s, con fracciones amorfas de alrededor del 70% para partículas de tamaño inferior a 45 μm, y hasta un 50% en fracciones de hasta 125 μm con una aleación de aluminio formadores de vidrio metálico de composición $Al_{86}Ni_8Y_{4,5}La_{1,5}$. Estos resultados muestran que el proceso de atomización centrífuga es adecuado para producir polvo de vidrio metálico diseñado para satisfacer las exigencias de varias aplicaciones industriales.

Al realizar este estudio exhaustivo, sienta las bases en el avance de producción de vidrio metálico mediante atomización centrífuga. Las perspectivas futuras incluyen una exploración con otros sistemas de aleaciones, como las aleaciones en base de hierro formadoras de vidrio metálico. aprovechando los conocimientos adquiridos para seguir mejorando los procesos de producción y ampliando las posibilidades de aplicación de estos materiales innovadores en la industria.

Acknowledgement

List of publications and conference contributions

List of publications

1. Cegarra, S. A.; Pijuan, J.; Hernández, R.; Riera, M.D. Effect of processing parameters on copper powder produced by novel hybrid atomisation technique, Powder Metallurgy. 2020, 63:2, 142-148. https://doi.org/10.1080/00325899.2020.1724431

2. Cegarra, S.A.; Pijuan, J.; Riera, M.D. Cooling Rate Modeling and Evaluation during Centrifugal Atomization Process. J. Manuf. Mater. Process. 2023, 7, 112. https://doi.org/10.3390/jmmp7030112

3. Pijuan, J.; Cegarra, S.A.; Dosta, S.; Albaladejo-Fuentes, V.; Riera, M.D. Centrifugal Atomization of Glass-Forming Alloy Al86Ni8Y4.5La1.5. Materials 2022, 15, 8159. https://doi.org/10.3390/ma15228159

Conference contributions

1. Cegarra, S. A.; Pijuan, J.; Hernández, R.; Riera, M.D. Fabricación de polvo de cobre por atomización híbrida. Congreso Español Iberoamericano de Pulvimetalurgia CEIPM2019, Madrid, Spain, 24-26 June 2019.

2. Cegarra, S. A.; Pijuan, J.; Riera, M.D. Production and microstructure of Al-Ni-Y and Al-Ni-Y-La powder by centrifugal atomization. EURO PM2020 Virtual Congress, 05-07 October 2020.

3. Cegarra, S. A.; Pijuan, J.; Riera, M.D. Centrifugal atomization and characterization of glass forming alloys ($Al_{86}Ni_8Y_6$ & $Al_{86}Ni_8Y_{4.5}La_{1.5}$). PowderMet2021, AMPM2021, and Tungsten2021 Technical Hybrid Conferences, Orlando, USA, 20-23 June 2021.

4. Cegarra, S. A.; Pijuan, J.; Riera, M.D. Cooling Rate Evaluation Of Al-4%Cu Alloy Powders During Centrifugal Atomization. EURO PM2023 Congress and Exhibition, Lisbon, Portugal, 01-04 October 2023.

Table of Contents

List of Figures

List of tables

List of symbols

Symbol	Description	Unit
A_s	Total surface area of a droplet	m^2
α	Factor dependent on the atomic arrangement	-
ΔS_f	Change in entropy per mole	$J\ mol^{-1}$
ΔH_m	Latent heat of fusion	$J\ kg^{-1}$
C_d	Drag coefficient	-
C_{pg}	Specific heat capacity of the gas	$J\ kg^{-1}\ K^{-1}$
$C_{p,l}$	Specific heat capacity of the material in the liquid state	$J\ kg^{-1}\ K^{-1}$
$C_{p,s}$	Specific heat capacity of the material in the solid state	$J\ kg^{-1}\ K^{-1}$
d	droplet diameter	m
d_{50}	Mass median particle diameter	m
d_k	Disk diameter	m
C_{DF}	Drag coefficient	-
f	Fraction of the nucleation sites	-
F_c	Centrifugal force	N
F_s	Surface force	N
h_c	Heat transfer coefficient	$W\ m^{-2}\ K^{-1}$
I	Homogeneous nucleation rate	$m^{-3}s^{-1}$
L	Distance between first adjacent arm to the last	m
k_p	Thermal conductivity of the droplet	$W\ m^{-1}\ K^{-1}$
m_d	Mass of the droplet	kg
n	Constant to calculate the cooling rate through SDAS	-
Nu	Nusselt number	-
Nu_{lam}	Laminar Nusselt number	-
Nu_{turb}	Turbulent Nusselt number	-
n_{arms}	Number of counted arms to calculate SDAS	-
η	Viscosity at the temperature T	Pa s
ρ	Droplet density	$Kg\ m^{-3}$
Pr	Prandtl number	-
Q	Melt flowrate	$m^3\ s^{-1}$
Q_c	Convective heat transfer	$W\ m^{-2}\ K^{-1}$
Q_r	Radiative heat transfer	$W\ m^{-2}\ K^{-1}$
R	Universal gas constant	$J\ mol^{-1}\ K^{-1}$
Re	Reynolds number	-
r_c	Hydraulic jump radius	m
RC	Cooling rate	$K\ s^{-1}$
R_c	Critical Cooling Rate	$K\ s^{-1}$
θ	Surface tension	$N\ m^{-1}$

T_A	Ambient temperature	K
T_d	Droplet temperature	K
T_f	Film temperature	K
T_g	Glass transition temperature	K
T_{rg}	Reduced glass transition temperature	k
T_l	Liquidus temperature	K
T_s	Solidus temperature	K
T_w	Wall temperature	K
t	time	s
U	Homogeneous growth rate	m s^{-1}
v	Droplet velocity	m s-^{1}
λ	Secondary dendrite arm spacing	μm
λ_0	Constant to calculate the cooling rate through SDAS	-
μ_g	dynamic viscosity of the gas	Pa s
μ_A	Ambient temperature viscosity	Pa s
μ_s	Viscosity at the droplet surface	Pa s
ρ_g	Density of the gas	Kg m^{-3}
σ	Lognormal standard deviation	-
σ_{ti}	Relative turbulent intensity	-
ω	Angular velocity	rad s^{-1}
X	Fraction of transformed phase	-

<div align="right">

CHAPTER 1

</div>

Introduction

1.1 Background and Motivation

In our daily lives, we encounter a diverse array of products made from various materials, each tailored to specific applications and requiring distinct material properties. The modern design and selection of high-performance structural engineering materials are guided by an intricate relationship of mechanical characteristics, encompassing strength, ductility, toughness, and elasticity, alongside the imperative need for predictable failure modes [1].

Finding a balance between strength and toughness poses a formidable challenge, as these attributes traditionally exhibit a trade-off. Ductile crystalline materials such as low carbon steels may boast high fracture toughness but often at the expense of a relatively lower yield strength, whereas ceramics typically exhibit higher strength but lower fracture toughness [2]. In this sense, metallic glasses enter as an integration of material classes. Unlike their crystalline counterparts, metallic glasses lack a regular atomic structure, granting them a unique fusion of characteristics found in both brittle and tough materials. These characteristics also include elevated hardness, wear resistance, and corrosion resistance, positioning metallic glasses as promising materials with a significant technological interest [3].

While metallic glasses have gained interest for their unique properties, their commercial adoption has been impeded by challenges in scaling up production [4]. Despite substantial research efforts aimed at enhancing our understanding of metallic glasses, significant knowledge gaps persist, indicating that widespread adoption may still be several years away [4]. Nonetheless, to date, Fe-based metallic glasses have found a niche in the market due to their soft magnetic properties [5,6], and the potential of metallic glasses to emerge as a disruptive technology, potentially supplanting traditional materials, and machining methods, continues to make them a promising material [4].

The primary challenge associated with metallic glasses lies in their production, as they are not easy to fabricate. Metallic glasses are materials with a disordered atomic structure [7]. Consequently, their production requires rapid cooling, which is essential to surpass the crystallization temperature. Only through rapid solidification can the atoms "freeze" into irregular patterns, resembling liquids, rather than the regular patterns found in conventional metals. Therefore, techniques like melt spinning or copper mold casting have been employed for their ability to facilitate rapid rates of solidification [8]. However, a notable limitation for certain alloys lies in the size of the final product since a high cooling rate in bulk is difficult to achieve [9]. These geometric limitations can be overcome through alternative production routes, such as the combined application of powder production and consolidation methods [10].

Gas atomization and water atomization has proven successful in the production of Al-based and Fe-based metallic glasses powder [10–20]. However, these techniques often yield irregular droplet formations, an abundance of satellite particles, and powder agglomeration, presenting limitations for the powder consolidation process [21]. In this sense, single fluid atomization

techniques such as centrifugal atomization become more appealing as it has demonstrated numerous advantages, including a relatively small particle size range, spherical shapes, free-satellite particles, cost-effectiveness, and high yield [22].

The centrifugal atomization process involves dispersing molten metal using centrifugal forces generated by a high-speed rotating disk that finally solidify in the form of powder. This technique is commonly employed in the production of powders from typical materials like Sn, Al, Mg, Zn, Cu, and their corresponding alloys [23]. Generating liquid droplets across a broad size spectrum, this process undergoes high cooling rates ranging from 10^3 to 10^6 K/s, with the values varying based on droplet size and influenced by the specific surface area of the droplets [24]. The significant rapid solidification rates of the droplets make centrifugal atomization a promising route for the synthesis of amorphous material. Remarkably, to date, there is no literature available concerning the production of glass-forming alloys using centrifugal atomization. Given the significant advantages offered by this technique for producing metallic powders and the lack of prior research in this field, it is imperative to thoroughly investigate, study, and refine the centrifugal atomization process for the production of amorphous metal powders. Therefore, this PhD delves into the science and technology of centrifugal-atomized glass-forming alloys, with a particular focus on the solidification processes that influence the potential production of Al based amorphous powders, as the production of metallic glasses can be facilitated not only by the process but also by the alloy composition chosen for production.

The selection of alloy composition plays a pivotal role in the formation of metallic glasses, often referred to as glass-forming alloys. For instance, the process of glass formation is facilitated by increasing the number of components in the alloy system. Additionally, the presence of significant atomic size differences among these components further promotes the formation of metallic glasses [25]. In this regard, the existing literature shows plenty of compositions capable of producing metallic glasses. The initial glass former compositions, developed in the 1970s, relied on highly expensive elements such as Pd, Pt, and Au [26–28]. However, contemporary compositions use more common and cost-effective elements such as Cu, Mg, Al, Ni, Fe, Zr, among others [26,27,29–33]. This shift has enabled the commercialization of metallic glasses, making them more accessible for various applications.

Within the scope of powder production, most of the research efforts have been predominantly conducted on Al-based, Zr-based, and Fe-based alloy systems [34–36]. Among these, Al-based metallic glasses have significant desirable attributes like high specific strength, good ductility, and effective corrosion resistance [36,37]. However, the production of amorphous metal powders presents several challenges due to their low glass-forming ability (GFA) compared to other metallic glasses [37]. Nonetheless, ternary compositions comprising AL-RE-TM (RE = Rare Earth, TM = Transition Metal), designed strategically, have proven to be good formers of Al-based metallic glasses, while possessing the advantageous properties sought after the aluminum amorphous alloys [36].

In the realm of centrifugal atomization, aluminum alloys are commonly atomized with this technique, and is known to be a well-established and straightforward atomization process [24,38,39]. The typically low melting temperature of these alloys provides an advantage by ensuring stable contact with the rotating disk, thereby minimizing instabilities in the atomization process. Taking this into account, Al-based metallic glasses were selected for this PhD thesis.

Within the context outlined above, the start of this PhD thesis arose to address the identified challenges. This research pursuits to enhance the production of Al-based metallic glasses

through centrifugal atomization, thereby paving the way for a novel technique in metallic glass powder production. The goal is to introduce a method that yields metallic glasses with the desired properties sought after by the powder metallurgy industry and other emerging consolidation technologies.

1.2 Aims of the study

The primary objective of this PhD thesis is to broaden the production scope of metallic glasses by incorporating the centrifugal atomization technique. This requires a thorough exploration, incorporating both theoretical and experimental aspects into the centrifugal atomization process, encompassing various elements such as the mechanisms of melt disintegration and droplet formation, fundamentals of atomization disk operation, and thermal transport within the atomized droplets. The focus lies on investigating the influence of various operating parameters, particularly emphasizing the understanding of the centrifugal atomization process to identifying strategies to enhance cooling rates. Therefore, the central research question formulated for this PhD thesis is:

Can the centrifugal atomization process achieve the required cooling rates to produce metallic glasses powder?

To address this question and achieve the primary research objective, the following specific objectives were defined:

Specific objectives

1. <u>To experiment with a hybrid atomization strategy aimed at increasing cooling rates and achieving finer particle sizes</u>. This entails designing a hybrid system to incorporate into the traditional centrifugal atomization system. Subsequently, the selected composition is atomized, followed by a thorough study of the results in terms of cooling rate.
2. <u>To develop and refine a numerical model for the solidification of droplets in centrifugally atomized powder.</u> Establishing a validated numerical model is crucial for providing a benchmark for all experimental findings and validating results. It is anticipated that a model will be developed to suit the centrifugal atomization process, supported by experimental findings for validation.
3. <u>To experiment with different atomization parameter configurations</u>, aiming to identify the ones that significantly boost the increase of cooling rate values in the atomized particles.
4. <u>To centrifugally atomize Al-based glass-forming alloys under various parameter conditions.</u> The objective is to illustrate the proportion of amorphous powder obtained under various atomization conditions and establish the optimal parameters for achieving this powder.

1.3 Scope of the research

This thesis primarily focuses on characterizing the centrifugal atomizer developed at *Fundació EURECAT*, patent number WO2020254365A1, for the production of metallic glasses powder. The applications and the detailed analysis of the properties of the produced powders are beyond the scope of this thesis, which focuses solely on the production aspect. The study encompasses metals such as copper, the Al-Cu alloy system, and Al-based glass-forming alloy systems. Other metal alloys are not included in the investigation. However, the findings obtained from this research could potentially be extrapolated to other materials and to other centrifugal atomizer equipment sharing similar characteristics.

1.4 Thesis structure

This thesis is the culmination of a collaborative effort between the Escola Politècnica Superior d'Enginyeria de Manresa (EPSEM) of the Polytechnic University of Catalonia and Fundació EURECAT. This collaboration was made possible through funding provided by the Pla de doctorats industrials per la Agència de Gestió d'Ajuts Universitaris i de Recerca of the Generalitat de Catalunya, under file number 2019 DI-19. The project is titled: *"Fabricación de metal en polvo a través de atomización centrífuga e híbrida de metales amorfos".* The thesis is presented as a compendium of papers published in recognized international journals in the field of metallic materials. This approach leads to a structured thesis outlined as follows:

Chapter 1 encompasses the general introductory aspects of the thesis, providing an overview of the general framework and that of the case study. It delves into the principal research motivation, describing the main objectives of the study.

Chapter 2 serves to provide the reader with a comprehensive understanding of the current state of the art in the field. Through an extensive review of relevant literature, this chapter situates the reader within the historical previous studies that have laid the groundwork for the present thesis. By examining past research, key concepts, and significant advancements, chapter 2 offers valuable context and insight into the evolution of ideas and methodologies leading up to the research presented in this thesis.

In Chapter 3, a thorough explanation is provided regarding the experimental design of each experiment conducted for every paper included in this thesis. This chapter aims to clarify details that may not be explicitly outlined in the papers, thereby offering additional information to the experimental procedures. Care is taken to avoid redundancy by minimizing repetition of information already present in the papers, ensuring that this chapter serves as a comprehensive companion to the research presented.

Chapter 4 presents the results in the format of the three following published papers:

PAPER I. Cegarra, S. A.; Pijuan, J.; Hernández, R.; Riera, M.D. Effect of processing parameters on copper powder produced by novel hybrid atomisation technique, Powder Metallurgy. 2020, 63:2, 142-148. https://doi.org/10.1080/00325899.2020.1724431. The influence of operating parameters in a novel centrifugal atomization process are investigated. The effects of gas flow

rate and rotational speed on the median particle size, microstructure, and cooling rate of pure copper powder produced using the hybrid atomization system are presented in the results.

PAPER II. Cegarra, S.A.; Pijuan, J.; Riera, M.D. Cooling Rate Modeling and Evaluation during Centrifugal Atomization Process. J. Manuf. Mater. Process. 2023, 7, 112. https://doi.org/10.3390/jmmp7030112. A comprehensive mathematical model to describe the thermal behavior of centrifugally atomized Al-4% Cu particles is developed. Valuable insights into heat transfer phenomena in the centrifugal atomization process are provided by this model, contributing to a deeper understanding of the cooling kinetics of molten metal droplets.

PAPER III. Pijuan, J.; Cegarra, S.A.; Dosta, S.; Albaladejo-Fuentes, V.; Riera, M.D. Centrifugal Atomization of Glass-Forming Alloy Al86Ni8Y4.5La1.5. Materials 2022, 15, 8159. https://doi.org/10.3390/ma15228159. The possibility of producing metallic glass alloy powders through centrifugal atomization is explored. The glass formation ability of the $Al_{86}Ni_8Y_{4.5}La_{1.5}$ alloy is analyzed, and the cooling capabilities of the process are investigated in the study.

In Chapter 5, a comprehensive analysis is provided, encompassing both general and specific conclusions drawn from the collective body of work, synthesizing key findings and insights. Additionally, the chapter offers future perspectives for advancing research in this field, resulting from the groundwork laid out in this PhD thesis. Through a complete examination of the research outcomes, Chapter 5 seeks to provide a cohesive narrative that underscores the significance and implications of the study's findings.

Literature Review

2.1 Metallic glasses

A glass material takes shape as a cooled liquid gradually solidifies without the formation of crystalline structures [7]. It is widely acknowledged that glasses can originate from materials with a range of bonding types, including covalent, ionic, metallic, Van der Waals, and hydrogen bonds [11]. While crystalline solids represent the stable state of matter at low temperatures, their formation involves the nucleation and growth of a new phase, processes that unfold over time, and are controlled by diffusion [40]. If the cooling rate is sufficiently rapid compared to the kinetics of crystallization, the liquid phase can be cooled without crystallization, leading to the formation of an amorphous atomic structure without discernible patterns [8].

The ability to form glasses hinges not only on cooling rates but also on other crucial factors. A selection of these factors will be briefly defined, with an emphasis on the formation of glass from the liquid state. It's worth mentioning that this PhD thesis does not cover all the methods for designing, processing, and consolidating metallic glasses (Ref. [25] gives very interesting additional details).

2.1.1 The concepts of metallic glasses

An undercooled liquid is one that successfully descends below its melting point T_m without undergoing crystallization. The extent of undercooling attained depends on various factors, which encompass the applied cooling rate or the removal of heterogenous nucleating sites [8].

Within a glass-forming metallic alloy, the liquid can undergo significant undercooling. As the temperature decreases, the viscosity of the liquid steadily rises, causing the constituent molecules to move at increasingly sluggish rates. When the temperature reaches a critical point, these molecules move so slowly that they lack the opportunity to undergo significant rearrangement before further cooling occurs [41]. At this juncture, the material's structure effectively becomes "frozen," and it is commonly referred to as an amorphous solid or glass. The specific temperature at which the viscosity reaches a critical high value, approximately 10^{12} Pa·s such that the liquid effectively "freezes in" is denoted as the glass transition temperature T_g [25].

The glass transition is intrinsically a kinetic phenomenon. T_g and the resultant glass structure exhibit a dependency on the cooling rate and are not constants inherent to the material. As illustrated in **Figure 1**, the T_g value increases as the alloy is rapidly solidified from the liquid state, highlighting the significant influence of cooling rates on this critical parameter. Furthermore, T_g manifests as a shift in heat capacity without any associated latent heat of fusion. This phenomenon characterizes a second-order transition, which is not a phase change but a kinetic event which depend upon the crossing of an experimental time scale and the time scales for molecular rearrangements [42]. Alterations in the specific heat and viscosity indicate that

metallic glasses often undergo a reversible glass-liquid transition at T_g. This suggests a close connection between the atomic arrangement of the glass and that of the liquid state [8].
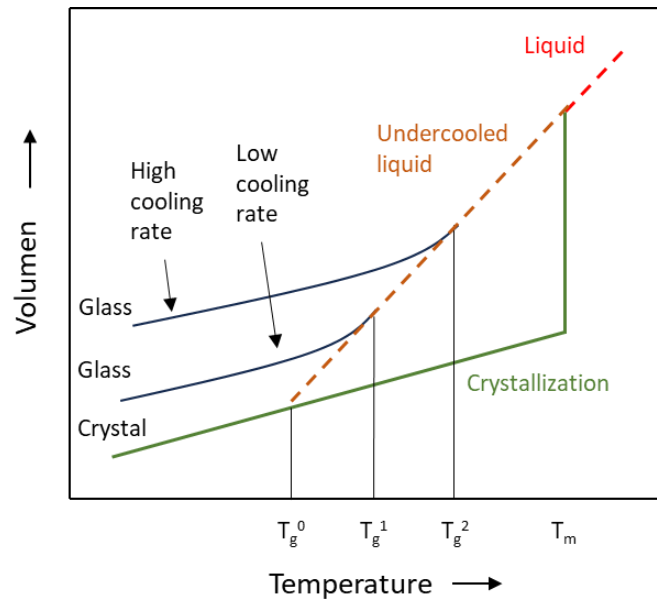
Figure 1. *Schematic representation on the variation of specific volume with temperature for a crystalline and a glass-forming material, adapted from Suryanarayana et al. [8].*

Metallic glasses are metastable in two respects: first, different cooling rates applied to the same alloy result in distinct glassy states with varying T_g values; second, at any given temperature, given enough time, the glass will relax and transition into the crystalline state [42]. However, considering that metallic glasses, formed through rapid quenching, exhibit glass transitions well above room temperature, they can be regarded as thermodynamically stable at room temperature. Consequently, thermodynamic principles applicable to equilibrium systems can be applied in these situations as well [43].

2.1.2 Glass forming ability

Most of the research focused on predicting glass-forming ability (GFA) relies on the classical nucleation and growth theory, which offer valuable insights [40]. This theory revolves around the idea that crystallization and amorphous formation are competing processes, determined by the relative thermodynamic and kinetic stabilities of the liquid phase and the resultant crystalline phases.

The homogeneous nucleation rate, *I*, and the growth rate, *U*, of a crystalline phase formed from an undercooled liquid can be expressed by means of Equation (1) and (2), according to Cheng et al. [44]:

$$I = \frac{10^{30}}{\eta} exp\left[\frac{-16\pi}{3} \frac{\alpha^3 \Delta S_f T^2}{R(T_{liq}-T)^2}\right] \tag{1}$$

$$U = \frac{10^2 f}{\eta}\left[1 - exp\left(\frac{\Delta S_f(T_{liq}-T)}{RT}\right)\right] \tag{2}$$

where η is the viscosity at the temperature T, f is the fraction of nucleation sites at the growth interface, α is a factor that depends on the atomic arrangement at the interface and has a value close to 1, ΔS_f is the change in entropy per mole due to melting, R corresponds to the universal gas constant and T_{liq} is the liquidus temperature.

The GFA of the alloy directly correlates with η, S_f, and $T/(T_{liq} - T)$. In the case of alloys primarily composed of metallic elements, it is worth noting that S_f remains relatively consistent across various alloys [44], allowing to treat it as a constant for the sake of simplicity. Consequently, the key parameters governing the GFA of an alloy can be simplified to η, the kinetic factor that increases with decreased temperatures, and $T/(T_{liq} - T)$, influencing the thermodynamic factor which increases by decreasing temperature [45]. The shear viscosity η in glass-forming alloys undergoes a substantial change, typically changing around 15 orders of magnitude as the temperature decreases from elevated levels to the glass transition temperature [46].

The classical nucleation theory is widely used to describe this phenomenon, though it is well known that considerable discrepancies exist with experimental results [47]. Nonetheless, it provides a simplistic description of the complex process of nucleation in metallic glass forming from liquid state. Nucleation rate varies within many orders of magnitude between the liquidus temperature and the glass transition temperature, and the classical nucleation theory does capture the essential features of this temperature dependence.

Figure 2 illustrates a schematic representation of plotting Eq. 1 and 2 for a hypothetical alloy. It becomes evident that the maximum growth kinetics rate generally occurs at higher temperatures, whereas nucleation is favoured at lower temperatures. The formation of a glass can occur when there exists a temperature range in which nucleation and growth rates do not overlap. Even if some nuclei are present, but no growth has occurred, the solid is, for all practical purposes, still a glass.

By knowing I, U at various temperatures, according to Suryanarayana [25] , it is possible to calculate the fraction of transformed phase X in a time t by means of equation (3):

$$X = \frac{1}{3}\pi I U^3 t^4 \tag{3}$$

A solid is considered a glass only when the volume fraction of crystal nuclei formed is below the detection level, typically taken as 10^{-6} [25]. Knowing these values, it is possible to measure the time it will take to form a nucleus to finally obtained the value of the Critical Cooling Rate R_c, which is the most important criterion to achieve glass formation.
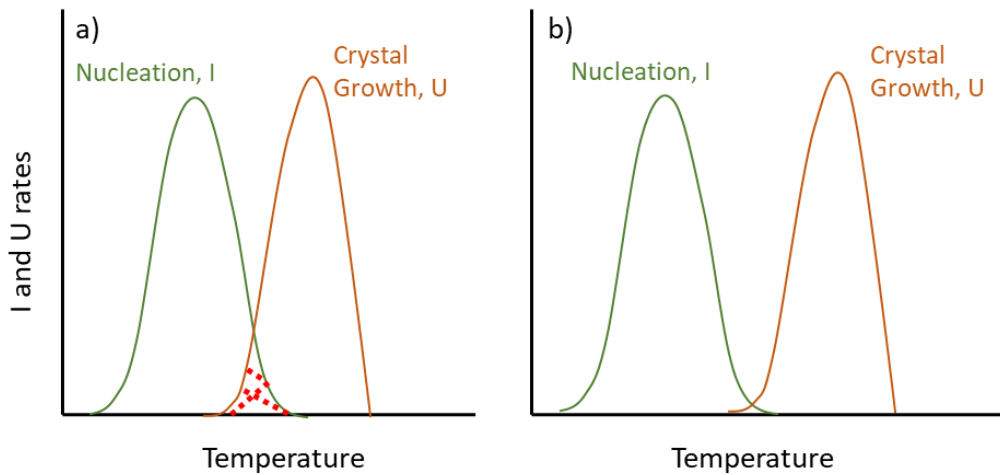
Figure 2. *Schematic representation of nucleation and growth rates: (a) overlapping leading to crystallization; (b) non-overlapping facilitating the glass formation, adapted from Steenberge* [48] *.*

A time-temperature-transformation (T-T-T) diagram (**Figure 3**) provides the quantification for crystallization under isothermal conditions, and it is known to be the best way to experimentally determine R_c. These curves have been thoroughly examined in previous discussions by Uhlmann and his co-workers [49–53]. These T-T-T diagrams serve as a tool to estimate the temperature-dependent initiation time of crystallization, aiding in the prediction of critical cooling rates, and they help in assessing the necessary processing time for shaping or consolidating glass-forming alloys [54]. The shape of the T-T-T curve, as well as the temperature and time at the nose, are determined by the interplay between two opposing factors: the growing impetus for nucleation due to greater undercooling and the declining atomic mobility caused by lowering the temperature [53].
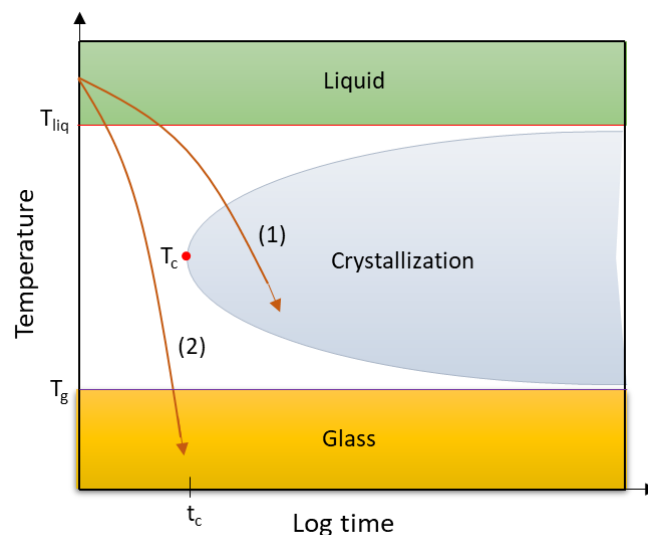
Figure 3. *Schematic time-temperature-transformation (T-T-T) diagram for a hypothetical alloy system quenching from the melt, adapted from* [19].

According to **Figure 3** a liquid can follow one of two solidification paths: when it traces the solidification path represented by curve 1, it passes through the crystallization nose, indicating that it is solidifying under equilibrium conditions. This process takes a considerable amount of

time, leading to the formation of a crystalline solid. In contrast, if the liquid adheres to the solidification path depicted by curve 2, the solidification rate is faster. As a result, it avoids the crystallization nose, resulting in the formation of a glassy solid. The temperature T_c at the tip of the nose corresponds to the critical temperature at a specific time t_c, which is the point at which glass formation becomes possible.

Additionally, as the crystalline nose depicted in the curves shifts to the right, the undercooled liquid becomes increasingly stable [55]. Consequently, the required cooling rates for producing a metallic glass decrease. Taking into consideration both thermodynamic and kinetic aspects, the required cooling rates to form a metallic glass can be reduced from 10^6 K/s to even 10 K/s [33,56], allowing the synthesis of metallic glasses with a thickness of up to 30 mm [57], commonly known as "bulk metallic glasses".

2.1.3 Metallic glass formation criteria

Since the first-time metallic glasses were successfully made with cooling rates exceeding 10^6 K/s [58], there has been notable advancement in the exploration of novel alloy systems with strong glass forming ability. However, the process of designing new compositions of metallic glasses is laborious, slow, and expensive process, which limits the ability of using the exceptional properties these materials can offer.

In addition to the critical cooling rate R_c mentioned earlier, which is widely regarded as one of the most crucial criteria for assessing the glass-forming ability of alloys, it's worth noting that other empirical criteria have been proposed and are worth mentioning.

- Turnbull's theory [59], grounded in the dynamics of crystal nucleation and the viscosity of molten alloys, proposes that the ratio of an alloy's glass transition temperature T_g to its liquidus temperature T_{liq} can offer insight into its GFA. In practical terms, a higher T_g/T_{liq} ratio indicates increased viscosity in the alloy's molten state, making it more conducive to solidifying into a glassy structure even with a lower R_c. This temperature ratio, known as the reduced glass transition temperature T_{rg}, is a key parameter. According to nucleation theory, it has been proposed that when T_{rg} reaches approximately 2/3, the occurrence of homogeneous nucleation for the crystalline phase is completely inhibited [60].

- Additionally, a strong GFA is associated with a decrease in the liquidus temperature T_{liq} [19], a phenomenon referred to as "deep eutectics", which is a system in which the eutectic temperature is significantly lower than the melting points of the individual components. This characteristic is frequently observed in alloys comprising multiple components and the value of T_{rg} is a strong function of the alloy composition. Therefore, the Turnbull criterion and deep eutectics converge at the deep eutectic compositions [8].

- Experimental observations of various glass-forming compositions led to the famously known as Inoue's empirical rules which comprises [45]: i) multi-component systems that consist of more than three components are favorable for glass formation, typically characterized by equilibrium diagrams with deep eutectics or low liquidus

temperatures; ii) a significant contrast in atomic sizes among the alloying elements plays a vital role, influencing both structural and electronic factors in facilitating glass formation; and iii) large negative values for the heat of mixing in the liquid phase, a factor rooted in thermodynamics, favors the glass formation. Such a rules are useful as a starting point to find elements that should be used to design a glass forming composition; however, it gives no information about the proportion among the elements.

Various criteria have been proposed in addition to these rules [8,25], but none offer universal applicability. Despite all these models, there is consensus among the researchers that a unique criterion to predict glass forming ability does not exist so far. Most of the presented criteria can be applied for a particular system with relative success, however, failing to predict GFA in other systems.

2.2 Centrifugal atomization of glass-forming alloys

2.2.1 Centrifugal atomization process

The key feature of centrifugal atomization involves the breakdown of a liquid molten stream under the influence of centrifugal forces generated by a rotating disk (**Figure 4**) [23].
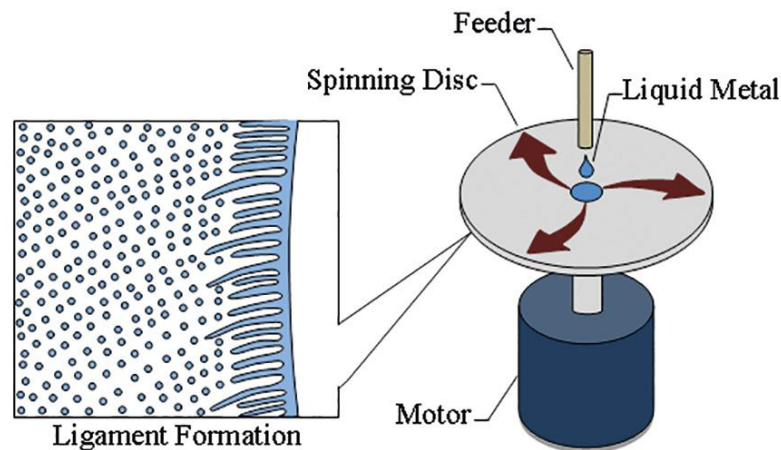
Figure 4. *Schematic illustration of the centrifugal atomization process* [61]*.*

As the disk rotates, centrifugal forces cause the molten metal to spread radially outward from the disk's center towards its edge, resulting in the formation of a liquid film on the disk's surface. As the film thickness decreases moving away from the center, instability near the edge results in wave or ripple formation, driven by the competition between outward spreading from centrifugal force and inward surface tension forces [22,23]. Eventually, the film breaks into droplets at the edge, which solidify in flight forming metal powder.

The melt disintegration process is influenced by the atomizing disk system, melt properties, and the consistent delivery of the melt, as highlighted in previous studies [62–64]. Moreover, the configuration of the atomizing disk not only shapes the droplet break-up process but also influences cooling conditions [24,65]. The subsequent solidification of droplets relies on the characteristics of the surrounding medium, where the gas acts as a heat-absorbing medium to cool the melt droplets through convection and radiation [66]. Further discussion on these aspects is presented in the following sections.

2.2.2 Flow melt on a rotating disk and droplet formation

The cooling rate of melt droplets is primarily influenced by droplet size [65]. This discussion covers the fundamental aspects of molten metal flow on a rotating disk, the formation of droplets, and highlights significant empirical insights for predicting particle size.

Hinze and Milborn [67], conducted a comprehensive study on the atomization of water and oils generated by rotating cups, incorporating a theoretical framework for the development of the liquid film along the cup wall. Depending on the melt flow rate on the rotating cup, three predominant modes of droplet formation were identified. **Figure 5** shows a schematic illustration of the primary modes observed during the centrifugal atomization process: direct droplet formation, ligament disintegration and sheet/film disintegration [62,68].

(a) DDF   (b) LD   (c) FD
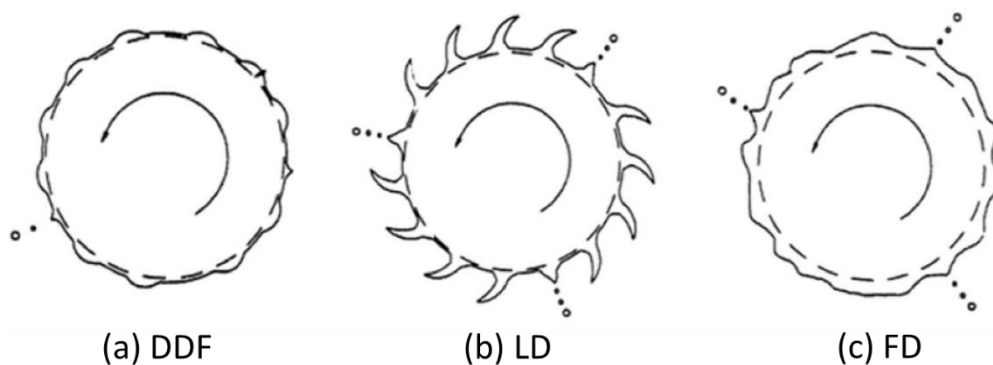
Figure 5. *Schematic diagram showing the three regimes of centrifugal atomization: (a) direct droplet formation; (b) ligament disintegration; and (c) film disintegration* [68]*.*

Increasing the liquid flow rate can facilitate the transition from one mode to another, given the same liquid, disk diameter, and rotational speed. [69]. The direct droplet formation mode takes place when the liquid feed rates and rotating speed are relatively small. During this mode, the molten metal spreads outward on the disk's surface and breaks up into discrete droplets directly off the disk. Continued increase in the flow rate, as the molten metal spreads on the rotating flat disk, it undergoes thinning and stretching, resulting in the formation of ligaments which further breaks into droplets. A higher melt flow rate will lead to the creation of a continuous film or sheet that extends beyond the disk, displaying irregularities or disturbances that break into droplets.

Champagne and Angers [62] investigated the atomization of aluminum (Al), copper (Cu), iron (Fe), and zinc (Zn), proposing that the group X value serves as an indicator for the atomization regime. Their work resulted in the development of a centrifugal atomization map for metallic melts, shown in **Figure 6**.
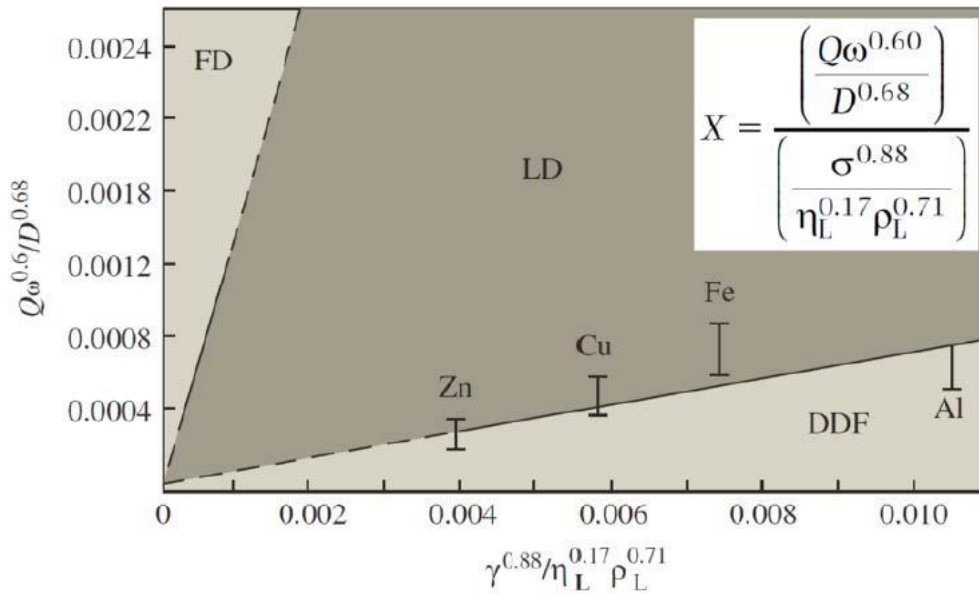
Figure 6. *Modes of centrifugal atomization. FD: film disintegration, LD: ligament disintegration, and DDF: direct droplet formation. Figure modified from* [62].

The specific mode observed during the centrifugal atomization process directly impacts the size of the atomized droplets [70]. Over the past five decades, numerous correlations have been proposed to predict the droplet size produced by a rotating disk associated with different break up regimes.

The following studies have been carried out on the ligament formation regime: Eisenklam [71] found that the disintegration of ligaments was attributed to the growth of waves. Subsequently, they derived an equation for the wavelength of ligaments based on the experimental data [72]. Boize and Dombrowski [73] explored the impact of viscosity on the atomization characteristics of a spinning disk. Their conclusion highlighted that the droplet size is effectively regulated by disk speed alone, irrespective of flow rate and viscosity. Frost [74] investigated the phenomenon of ligament formation induced by a rapidly rotating flat disk, establishing criteria for ligament occurrence, and developing an expression to predict drop size. In 1982, Kawase and De [75] examined the correlations governing the generation of ligaments by a spinning disk, providing an expression for the number of ligaments formed by both Newtonian and non-Newtonian fluids on a spinning disk. Ahmed and Youssef [69] explained the disintegration modes and their transitional behavior, observing that drop and sheet modes exhibit instability, while the ligament mode represents an almost quasi-stable state of atomization. In more recent research, Wang et al. [76] experimentally investigated the ligament formation breakup process. They introduced models for ligament numbers, the tail end diameter of ligaments, and the mean diameter of droplets. Their findings indicated that the tail end diameter of ligaments and the size of droplets decrease with increasing rotational speed, while the flow rate has a relatively smaller impact.

Regarding the sheet formation regime Fraser et al. [72] explored the flow characteristics of sheets generated by spinning cups, identifying two primary mechanisms for sheet disintegration. The first occurs at relatively low peripheral speeds and liquid flow rates, while the second occurs

at higher peripheral speeds and liquid flow rates. Dombrowski and Lloyd, [77] investigated the spreading of viscous liquids on a rotating vane, deriving a theoretical relationship for the film profiles. Applying the theory of wave disintegration, Dombrowski and Johns [78] developed a drop-size equation for calculating the diameter of drops produced from liquid sheets, which are generated by a fan-spray nozzle. Kamiya and Kayano [79] formulated an equation for the maximum drop diameter by conducting atomization experiments on film-type disintegration using a rotating disk, with their investigation concentrating on film extension and the thickness of the liquid film at the leading edge.

In the realm of direct drop formation, numerous studies have investigated the calculation of droplet diameter through theoretical equations. In 1981, Champagne and Anger [62] proposed the empirical Equation (4) to predict the median particle size from centrifugal atomization, accounting for the effects of liquid flow rate:

$$d_{50} = \frac{3.65}{\omega d_k^{0.58}} \left(\frac{\theta}{\rho}\right)^{0.46} Q^{0.06} \tag{4}$$

where d_{50} is the (mass based) median particle size (m), d_k is the disk diameter (m), ω is the angular velocity (rad/s), θ is the surface tension (N/m), ρ is de density (Kg/m^3), and Q is the liquid flow rate (m^3/s). Shemayakina et al. [61] proposed in 1992 the empirical equation:

$$d_{50} = \frac{3.65 \ x \ 10^6}{(2\pi\omega/60)^{0.95} d_k^{0.61}} \left(\frac{\theta}{\rho}\right)^{0.42} \left(\frac{Q^{0.12}}{10^6}\right) \tag{5}$$

Of particular interest is Liu's et al work [80], where they examined the mechanism of drop formation in rotary cups using a high-speed camera. The three distinct disintegration formations where identified that emerged with increasing angular speed while maintaining a constant flow rate. The study also involved the development of theoretical equations for calculating the diameter of liquid drops generated during both direct drop and ligament formation.

During direct drop formation, equilibrium is established when the centrifugal force F_c and the surface force F_s are balanced [80]. The centrifugal force can be expressed using the following equation [23]:

$$F_c = \frac{\omega^2 R\rho\pi d^3}{6} \tag{6}$$

On the other hand, the surface tension is expressed by the following expression [23]:

$$F_s = \pi d\theta \tag{7}$$

By combining both forces, one arrives at the following expression that defines the average particle diameter generated through centrifugal atomization [80]:

$$d_{50} = \sqrt{\frac{6\theta}{\rho r \omega^2}} \tag{8}$$

15

where r is the disk radius (m). This simple expression proves inadequate for high metal feed rates, where ligament and sheet formation become the dominant disintegration modes. Its limitation lies from the omission of factors such as the intricate bulging film, aerodynamic forces, and slippage on the atomizer itself, among others [23]. However, it is still used as it gives a good indication of the importance of the major parameters.

Although numerous studies have been conducted on the topic, there is still a lack of comprehensive understanding regarding the transition characteristics of droplet formation. Furthermore, existing correlations vary among investigators and often lack consistency, which can be attributed to variations in operating conditions, disc configurations, and the inherent challenges associated with precise droplet size measurements [70]. Consequently, relying on predicted droplet sizes obtained from these correlations may be inadequate, and the extended recommendation is to measure the particle size distribution experimentally. In general terms, it is safe to say that the resulting particle sizes generally conform to a lognormal distribution, with smaller powder particles obtained through lower melt flow rates, higher rotation speeds of the atomizer, and larger diameters of the atomization disk [22,81,82]. Centrifugally atomized powders distribution curves typically have a standard deviation of 1.3-1.5 [81], which implies achieving a yield within a limited particle size range [23].

2.2.3 Atomization disk

While various factors influence the resulting atomized powders, the atomizer disk stands as the pivotal component in the centrifugal atomization process, and the quality of the resulting powder depends strongly on the characteristics of the disk in terms of disk velocity, size, shape, and material.

Rotating speed

Evidence from experiments indicates that elevating the rotational speed leads to a reduction in droplet size [81,83–87]. Sungkhaphaitoon et al. investigated the impact of atomizing disk speed on the median particle size, employing three equations from existing literature: the theoretical equation by Li et al. [80], the empirical equation proposed by Champagne and Angers [62], which considers liquid flow rate, and an empirical equation proposed by Shemyakina [81], The three equations consistently depict a reduction in median particle size as the atomizing disk speed increases. It is noteworthy to observe that Equation (8) by Liu, despite its simplicity, effectively captures this refinement. As a result, authors commonly favor this equation as a reliable estimate for predicting the median particle size to be achieved.

Figure 7 depicts the theoretically possible particle sizes at various rotation speeds for different pure metals at their liquidus temperatures from Equation (8), revealing that higher rotation speeds generally result in smaller particle sizes due to increased centrifugal forces, with the material parameters of density and surface tension influencing this outcome. This trend holds true even when applying different correlations found in the literature, as they exhibit an inverse relationship with the angular velocity of the disk.
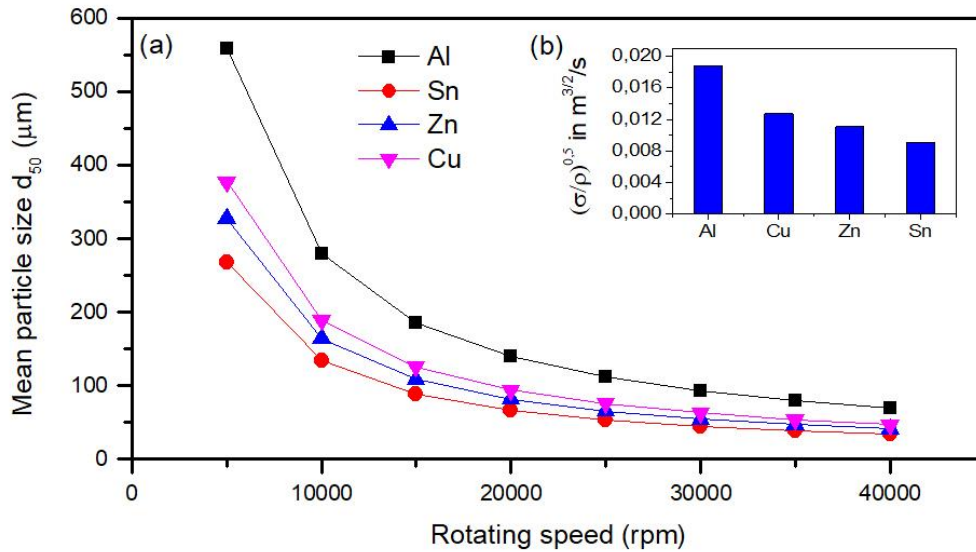
Figure 7. *(a) Theoretical particle size dependent on the rotation speed of various pure metals, for a disk radius of 40 mm; and (b) square rooted surface tension to density ratio at the melting point.*

Typically, in prior investigations comparing theoretical and empirical equations for predicting the median particle size in centrifugal atomization with experimental results, it is common to observe that the experimental median particle size tends to be larger than the values predicted by the models [61,86]. There are numerous explanations for this phenomenon, as the resultant median particle size is influenced not only by the disk velocity but also by various factors that are either not accounted for or cannot be fully considered by the models. These factors include aspects such as the slippage of the melt, associated with the optimal wettability of the disk, as well as the disk's shape, size, melt flow rate, among others, which will be further discussed in the subsequent sections.

Disk atomizer configurations

Empirical and theoretical correlations aiming to predict the median particle size of the resulting powder, within the various modes they are applied, typically rely on specific disk configuration parameters. Consequently, these correlations are often tailored to a particular setup and lack the flexibility to extrapolate to different configurations. While certain parameters like disk speed or melt flow rate might be adjustable, one critical parameter that cannot be changed in most of the formulations is the disk shape. Therefore, the impact of disk shape on the resulting particles is often experimentally investigated.

The investigation of disk configuration has been investigated in numerous applications where it becomes essential to atomize a liquid body and break it down into small, preferably uniform droplets [82,88–90]. Different atomizers, including flat discs, vaned wheels, inverted bowls, and cups, have been subjects of study over an extended period. In the context of centrifugal atomization of metal powder, it is worth highlighting several significant studies.

17

Osturk et al. [24,39,83] produced Sn, Al, Pb, Zn, and AA2014 by a novel water-cooled rotating disk atomization and studied three disk configurations—flat, flat with fins, and cone with fins. **Figure 8** displays the various designs utilized in their study. They reported that the flat-type disc exhibited a finer mean particle size and higher yield rate than the conical disc, attributed to incomplete energy transfer on the inclined surface. Furthermore, using a flat disk geometry with two fins resulted in fine particles size compared to configurations with four and six fins.
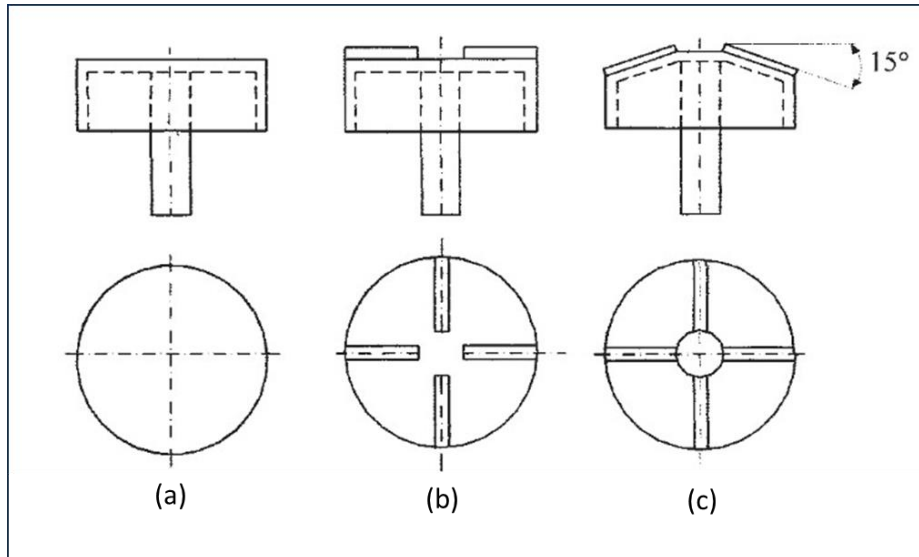
Figure 8. Disks with different configurations: (a) flat disk; (b) flat disk with fins; and (c) cone with fins. Figure taken from [83].

Xie et al.[81] investigated different atomizing disk designs on tin atomization, using two types of disk geometries—a flat disk and cups with wall slopes at angles of 45°, 67.5°, and 90° degrees—each with an 80 mm diameter. They reported that under their experimental conditions, using a cup instead of a flat disk resulted in a reduction of particle size by up to 25% at higher speeds and 20% at lower speeds, with a discernible trend towards finer powder as the cup wall angle increased to 67.5° relative to the horizontal. In a subsequent study in 2017 [85] they replicated their earlier investigation, aiming to comprehensively analyze the particle size distribution of powders produced through the rotation of cups. They observed that the median particle size generated by the 45° cup closely resembled that produced by a flat disk across various combinations of rotation speed and melt flow rate. In contrast, the 67.5° cup exhibited superior performance under all conditions, yielding powder particles 40% to 60% smaller compared to those produced by both the flat disk and the 45° cup.

In 2011, Plookphol et al. [86] examined the impact of disk shape and diameter on the atomization of SAC305 lead-free solder powder, using cup-shaped and flat disk-shaped atomizer configurations with diameters of 30, 40, and 50 mm respectively. They observed that SAC305 powder atomized with a cup-shaped atomizer is roughly 11% smaller in size than when using a flat disk-shaped atomizer. Additionally, they noted a decrease in median size with the use of the larger atomization disk but this was conditioned on an increase in rotating speed and melt feed rate.

In line with the ongoing exploration of the impact of cup-shaped and flat disks on resulting powder characteristics, Sunghapahitootn [91] conducted a study on zinc atomization in 2013. The study encompassed both designs, with each having diameter sizes of 30 and 50 mm. It was observed that the median particle size of zinc powders produced by both the flat disk and the cup-shaped atomizers decreased with increasing atomizer disc size. When comparing results for the same disc sizes, the cup-shaped disc yielded a smaller median particle size than that produced by the flat disc. This finding aligns with results previously documented by Xie et at. [81,85] and Plokphol et al. [86] mentioned in the previous paragraphs. **Figure 9** illustrates the disk designs employed in the studies focusing on flat disks and cup-shaped disks.
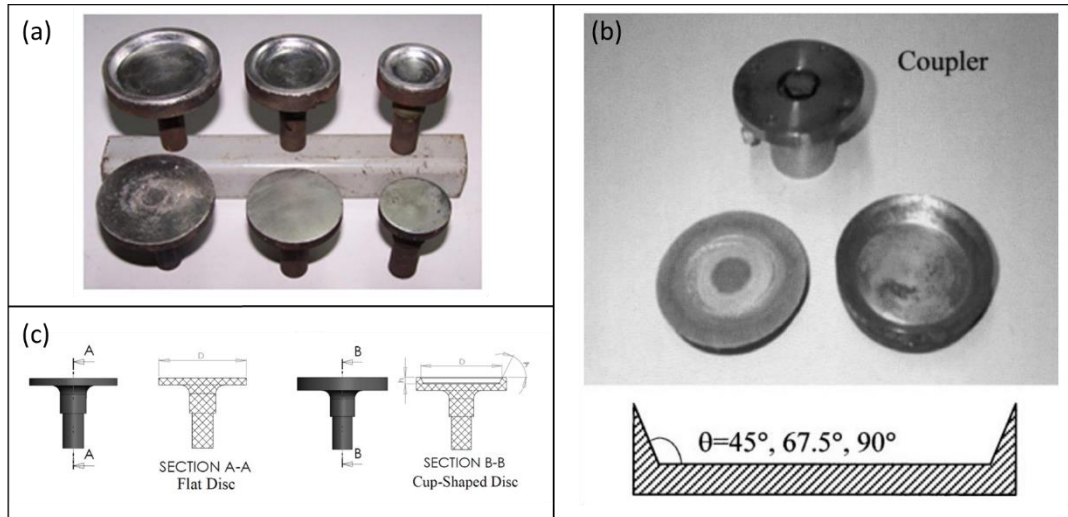
Figure 9. *Rotating atomizers with various configurations from different studies on flat disks and cup-shaped disks: (a) cup shaped (top row) and flat disk shaped (bottom row) with the diameter of 30, 40, and 50 mm (from right to left) taken from* [86].*; (b) atomizer coupler and typical discs used in* [81]*; and (c) atomizer discs: flat disc (left) and cup-shaped disc (right) taken from* [91]*.*

It is noteworthy to highlight the study conducted by Mahmoud and Youssef [92]. They investigated the impact of different configurations of rotating disks and cups on droplet size, shown in **Figure 10**, with experiments consistently carried out at a rotating disk speed of 12,000 rpm using water as the atomization liquid. They compared measurements of Sauter mean diameter and average droplet velocity for the studied cups and disks with those produced by a standard flat disk atomizer. They did not observe significant differences among the various configurations, suggesting a preference for using a flat rotating disk over more complex shapes such as rotating disks or cups.
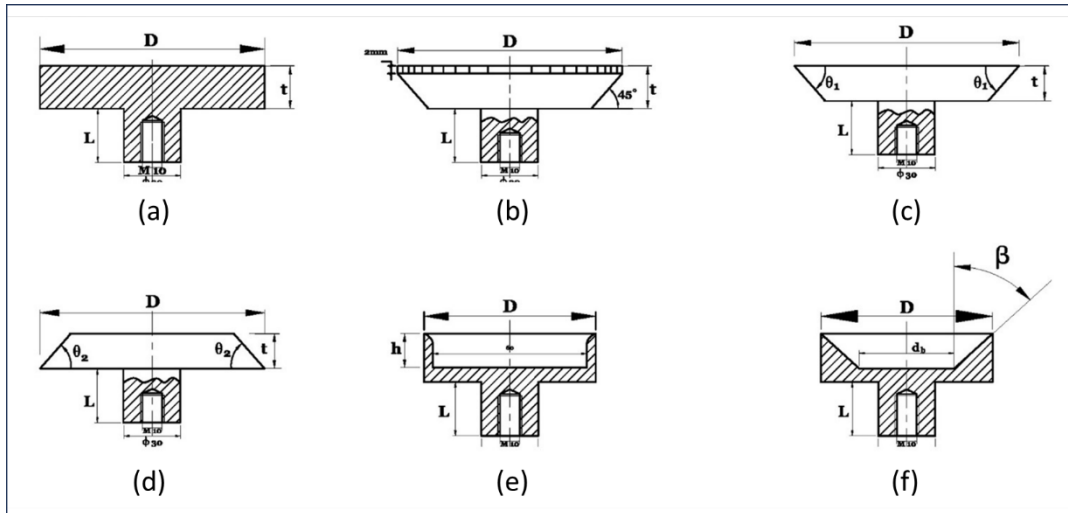
Figure 10. *Disks and cups with different configurations as follow: (a) regular flat disk, (b) disk with serrated edge, (c) disk with different upper edge angles, (d) disk with different lower edge angles, (e) cylindrical cup with different heights, and (f) conical cup with varying cone angle and base diameter. Figure taken from* [92].

Numerous studies have explored the impact of atomizer disk shape on mean particle size in slag granulation. It is worth mentioning that these studies also arrive at a similar conclusion as the studies mentioned above, indicating that the geometry of the disk does indeed impact the resulting particle size. For further details, refer to references [93–96].

As can be seen, over time, various studies have delved into the influence of atomizer shape and diameter on the resulting particle size, especially when comparing a flat disk with a cup-shaped disk. However, these studies have yielded varying results. On the surface, a cup atomizer appears to promote finer particle sizes by subjecting the liquid to a substantial force toward the cup wall, leading to effective spreading of the liquid film and delaying film disintegration into ligaments [85]. Yet, there seems to be an optimal wall angle for this phenomenon to occur, and the observed differences in particle sizes may not be significant enough to justify the use of complex disk designs [69]. Additionally, variations in results are often influenced by the specific application and other parameters such as disk speed, disk material, or the type of liquid being atomized. Isolating the effect of disk design from these multifaceted factors proves challenging.

Wettability and feed rate

As mentioned in the previous sections, with the development of various models to characterize the disintegration of the melt on a rotating disk, it has become evident that, for an ideal atomization, the film thickness and the radial and tangential velocity distribution of the melt on the rotating disk play a crucial role [85]. To improve the spreadability of the melt, it is essential for the disk to exhibit excellent wetting conditions, coupled with low heat capacity and thermal conductivity [68].

Wettability is determined by the contact angle formed by the melt on the disk, and simultaneously, this contact angle is influenced by the interfacial tensions at the boundary

between the liquid, the disk, and the atmosphere [97]. When the melt completely wets the disk, it spreads uniformly, and the flow exhibits axi-symmetry with a consistent film thickness throughout its circumference. Conversely, if the melt fails to achieve full wetting on the disk, the surface tension can surpass the centrifugal forces, leading to retraction from the disk surface. As a consequence, the film begins to disintegrate before reaching the disk's edge [63].

The lack of complete wetting, along with a low superheating of the melt, can contribute to the formation of a skull on the disk [98]. A skull refers to the amount of premature solidification of the molten metal on the disk's surface [81]. This skull diminishes the effective radius of the atomization disk, resulting in larger droplet sizes since atomization occurs at the edge of the skull rather than the disk edge [68]. Additionally, the skull may detach from the atomization disk during operation, posing a potential risk to the facility. Therefore, it is preferable to prevent the formation of the skull in most cases.

To improve wettability, various coatings are commonly applied to the disk surface. Ideally, the coating should exhibit corrosion resistance and serve as a thermal insulator to minimize the solidification of molten metal on the surface of the rotating disk [38]. Moreover, the coating should have strong bonding capabilities with the disk, high resistance to thermal shocks, and relative inertness with respect to the atomized metal [63,68].

Angers et al. investigated the corrosion resistance of various coatings, including TiB2-based, alumina, mullite, chromite, graded alumina, and graded partially stabilized zirconia (PSZ), plasma-sprayed on 1020 steel rods against molten aluminum and magnesium [38]. Their results showed that the disks coated with graded PSZ gave the best performance in terms of corrosion resistance, thermal conductivity, and thermal insulation. Osborne et al. and Xie et al. [81,99] have improved the wettability of stainless-steel atomization disks by applying a thin coating of other metals, such as tantalum and tin, respectively. Similarly, optimal wetting can be attained when the liquid metal comes into contact with a coating possessing a composition resembling that of the molten metal [86]. Other authors have successfully used coatings such as graphite, zirconia, and copper [39,65,100–102]. Overall, the decision on the type of coating to use will largely depend on the characteristics of the melt being poured onto the disk.

Hydraulic Jump

Upon impact with the disk, the liquid metal stream experiences high centrifugal force, causing it to flow radially with accelerating tangential and radial velocities. However, these increases in radial velocity are not sustainable indefinitely, often leading to a hydraulic jump, meaning that there is a sudden increase in the thickness of the liquid metal on the disk, often accompanied by a reduction in radial velocity [103].

Zhao et al. [97] developed a mathematical model to predict both the occurrence and location of the hydraulic jump. The model also addresses the associated changes in the height profile, as well as the radial and tangential velocities of the liquid metal on the disk. According to their model, the hydraulic jump for a flat disk occurs at a radius approximated by:

$$r_c = 0.55 \left(\frac{\rho Q^2}{\mu \omega} \right)^{1/4} \tag{9}$$

where ρ is the specific density, μ is the viscosity, Q is the volume flow rate of the melt and ω is the rotation speed of the disk. The schematic representation of the liquid profile is depicted in **Figure 11**. As illustrated, the height of the liquid metal on the disk, denoted as h_1 before the hydraulic jump and h_2 after the hydraulic jump, exhibits variations with respect to the radius. Similarly, the radial, tangential, and axial components of the liquid velocity, denoted as u, v, and w, respectively, exhibit variations both in radius r and axial distance z from the disk surface.
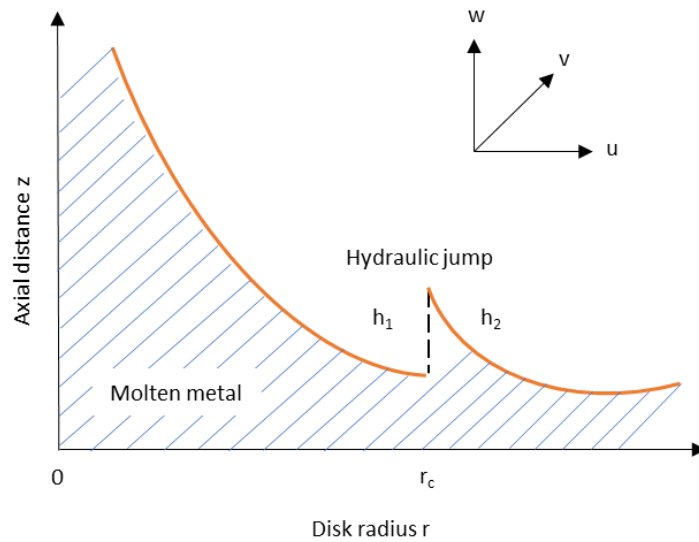
Figure 11. *Schematic representation of the liquid metal's height profile on an atomizing disk, with the assumption that a hydraulic jump occurs at a radius of r_c* [97].

From Zhao´s work [97], it was also concluded that an increase in the flowrate leads to an increase in the liquid metal height on the disk, as well as the critical hydraulic jump radius. Zhang et al. [85] established a correlation between the median particle size observed in the atomization of tin and the thickness of the tin melt film beyond the atomizer edge, as calculated by Zhao's model. The findings indicated a linear relationship between the median particle size and the theoretical film thickness. Furthermore, the predicted film thickness decreased with a decrease in the melt flow rate and an increase in the atomizer rotation speed.

2.3 Thermal aspects in the process of droplet solidification

In this section, the fundamental aspects of rapid solidification are described. A comprehensive review of the literature is revised, shedding light on methodologies for both measuring and modeling the cooling rate for atomization techniques. For the sake of simplicity, the detailed description of the model used in this research is deferred to Paper II within this thesis, enabling redundancy to be avoided.

In the scientific literature, a rapid solidification process is defined as the rapid heat extraction of thermal energy occurring during the transition from a liquid state to a solid material [104]. There are three fundamental approaches to achieve rapid solidification [105]. The first involves imposing a high degree of undercooling before the initiation of solidification. The second method entails maintaining a high front velocity during continuous solidification. The third approach is characterized by imposing a high cooling rate throughout the solidification process.

Given that the technique employed for producing amorphous particles in this PhD thesis is centrifugal atomization, the rapid solidification process is achieved by imposing high cooling rates. This method refers to any solidification process characterized by cooling rates within the range of 10^2 to 10^7 K/s [106].

2.3.1 Methods for measuring the cooling rate

Several approaches exist for measuring cooling rates, encompassing direct measurements, indirect measurements, and numerical models.

Direct methods for measuring cooling rates involve the immediate assessment of temperature changes during a material's solidification process. These in-situ measurements have depended on optical sensing, thermal radiation sensing, and light scattering sensing techniques [107]. While direct measurements have been attempted [107–109], their difficulty arises from the challenging conditions and chaotic nature of atomization processes. Hence, experimental indirect measurements and numerical models have been the most employed and reliable methods for estimating cooling rates, despite their inherent limitations.

The indirect method for measuring cooling rates involves examining microstructural features, such as grain size [110], dendrite arm spacing [111], and eutectic interlamellar spacing [112], effectively characterizing parameters in the rapid solidification process. This is a well-known process first studied by Flemings et al. [113]. The microstructural features are directly influenced by the rate of heat extraction, and consequently, the solidification rate during the solidification process. In the liquid-solid ("mushy") zone of binary alloys, new dendrites form with random orientation. Initially, as the dendrite arm spacing grows in the melt, it appears very fine. However, as solidification progresses, only certain arms continue to grow, while others dissolve. The final dendrite arm spacing is then determined by the coarsening process [114]. Notably, the finer the spacing observed indicates that the coarsening process occurred over a shorter period. Cahn and Greer [19] highlighted certain limitations of indirect measurements, noting that such methods can provide estimates only within the temperature range of solidification, neglecting the subsequent cooling rate in the solid state. They emphasized that each family of alloys need a

separate calibration, and cautioned that dendrites may undergo coarsening after solidification, potentially leading to misleading results.

Nevertheless, despite its limitations, this method remains the most trusted approach for indirectly measuring cooling rates. The microstructural refinement achieved through atomization techniques is frequently assessed using the Secondary Dendrite Arm Spacing (SDAS) method [111]. This method relies on the following formula:

$$\lambda = \lambda_0 C R^{-n} \qquad (10)$$

where the constants λ_0 and n are experimentally derived and are dependent on the solidification time Δt and the cooling rate C_R. The actual value of n often falls within the range of 0.3 to 0.5 [115].

Secondary dendrite arm spacing measurements in aluminum alloy powders

Despite over 30 years of research on SDAS measurements, significant discrepancies in the technique persist among researchers [116–118]. In their study, Eli et al. [119] evaluated various measurement methods for castings produced at different solidification rates, finding inconsistencies that may arise when using different methods. This comparison analysis was performed on the centrifugal atomization process for Al4%Cu powders [120]. The different methods employed are shown in **Figure 12**.
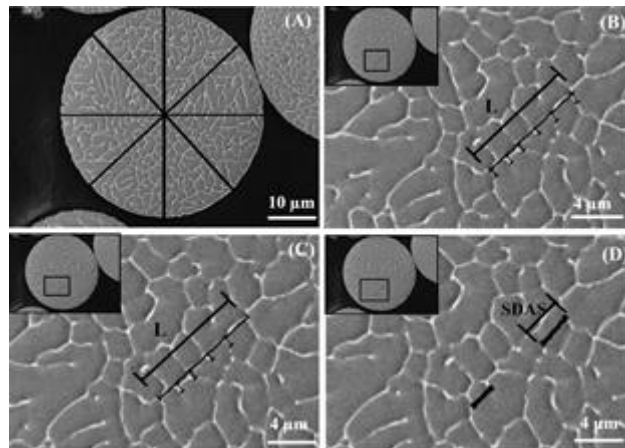
Figure 12. *Schematic representation of SDAS measurement methods* [120]*.*

In method A, the line intercept method was used to measure the cell spacing in a particle [121]. In alloys with a small amount of interdendritic phase, such as Al4%Cu, it is recommended the use of dendrite cell size as the most desirable value for describing dendritic microstructure, being equivalent to dendrite arm spacing. The representative particles were traversed along 4 straight lines counting the number of cell intercepts over known distances in each one of them.

In method B, L (µm) represents the length of the primary dendrite arm, whereas in method C, L represents the length of the primary arm just between the first and the last secondary dendrite arms. N_{arms} is the number of secondary dendrite arms counted [116,119]. For these methods, the secondary dendrite arm spacing was determined according to the relationship between primary and secondary dendrite arms, represented in the following equation [121]:

$$SDAS = \frac{2}{N_{arms} - 1} \tag{11}$$

Finally, method D consists of making direct measurements between secondary arms of adjacent dendrites.

The findings revealed that while each method observed a decrease in SDAS with decreasing particle sizes, Methods C and D emerged as the most accurate and precise among the four methods [120]. Consequently, in this PhD thesis, Method C was employed to measure the secondary dendrite arm spacing in Paper II due to its demonstrated accuracy and efficiency, considering the number of particles to be measured.

Grain size measurement in copper powders

Regarding the grain size analysis of copper powder, according to ASTM E112 standards [122], three widely recognized techniques are employed to assess the grain size of ground, polished, and etched cross-sections of metallographic specimens. These techniques include a) the comparison procedure, b) the planimetric procedure, and c) the linear intercept procedure. The comparison procedure entails evaluating the grain structure against a series of graded images; the planimetric method involves a direct count of the number of grains within a known area; and finally, the intercept procedure requires counting the number of grain boundary intersections with a line traversing the sample.

It is noteworthy that to employ any of these techniques, certain criteria must be met in selecting the micrograph for analysis. One crucial criterion is that the polished surface area should be sufficiently large to enable the measurement of at least five fields at the desired magnification [122]. Given the small size of powders produced by atomization techniques, meeting this criterion for a single particle is unlikely. Therefore, in the research detailed in Paper I, a different approach was used for calculating average grain sizes in copper powder. For each particle size range, five distinct micrographs were chosen, and the mean surface area of the grains in the particles corresponding to each micrograph was measured. For further insights, refer to Paper I.

2.3.2 Numerical models for measuring the cooling rate

As mentioned previously, the measurement of cooling rates can also be approached through numerical models. Levi and Mehrabian [123] were among the pioneers in investigating the solidification behavior of undercooled droplets, employing both Newtonian and Non-Newtonian heat transfer models, and developing a comprehensive mathematical formulation that incorporates atomization process parameters, growth kinetics, interface velocity, undercooling, and other significant solidification factors. They observed that the solidification of melt droplets can follow distinct scenarios: first, solidification occurs without notable undercooling; second, nucleation is suppressed, leading to complete solidification of the system; and third, a significant undercooling is followed by rapid heat extraction of the latent heat, causing a rapid increase of temperature almost to the melt temperature (recalescence). Recently developed models integrated droplet dynamics and thermal profiles during molten metal atomization, consistently predicting size distribution, velocity, history, temperature, cooling rates, and microstructural features, particularly secondary dendrites, as a function of process conditions [12,124–126].

In the process of rapid solidification, as observed in atomization processes, different solidification paths are typically detected as seen in **Figure 13** [114]. These paths include: (a) the liquid state before reaching the primary nucleation temperature, (b) recalescence of the undercooled melt, (c) post-recalescence/segregated solidification, (d) eutectic solidification, and finally, (e) cooling in the solid state. The nucleation of the solid phase at the nucleation temperature $T_{nuc.}$ initiates the release of latent heat, leading to rapid heating of the undercooled droplet and the onset of the recalescence process. However, the first dendrites form in the mushy zone, surrounded by residual melt, and solidification continues in the segregated region (c), where secondary dendrite arms are formed through coarsening.
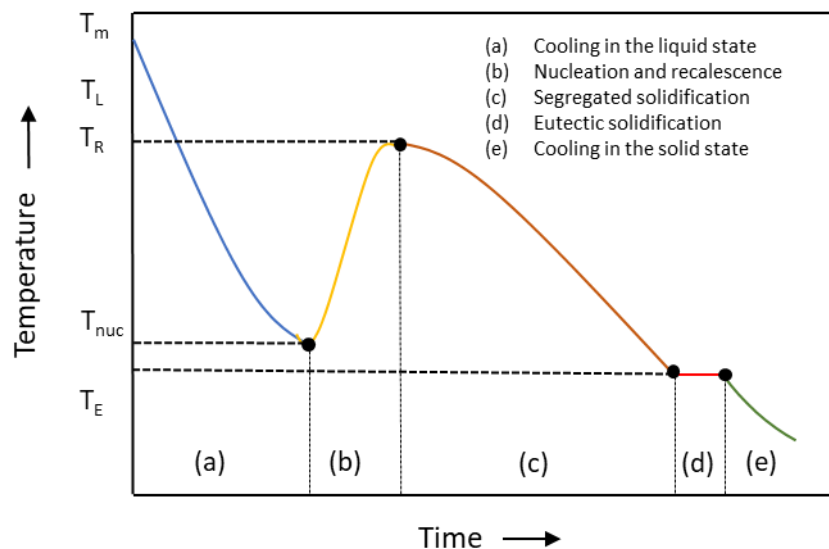
Figure 13. *Schematic illustration describing the droplet solidification process, adapted from Lee et al.* [126].

Estimating droplet temperature across various solidification paths requires making assumptions to establish the boundary conditions for the differential equations, thereby

26

simplifying the thermal analysis of the droplet. Therefore, the calculation of the local solidification process varies depending on the assumptions considered, which will determine the model employed. For models incorporating undercooling, recalescence, segregation, and eutectic solidification, a thermal model with kinetics is applied [127–129]. In contrast, a thermal model without kinetics determines the local solidification time under equilibrium conditions [124,130]. Additionally, thermal models without phase change characterize scenarios without a solidification interval, as in the case of amorphous materials [19].

For the sake of simplicity and to avoid repetition, all assumptions made in this PhD thesis are presented and explained in Papers II and III. In general terms, no undercooling is considered since it has been demonstrated that the use of microsegregation models does not make a significant difference in the cooling rate analysis [131], given that the rate of heat generation during recalescence period is well balanced by the rate of heat removal at the droplet surface [126,130]. In Paper II, the cooling rate was determined for the crystalline Al-Cu alloy. In this context, the cooling rate is computed as the difference between liquidus and solidus temperature with respect to the local solidification time:

$$CR = \frac{T_{liq} - T_s}{t_{ls}} \tag{12}$$

where T_{liq} and T_s are the liquidus and solidus temperature and t_{ls} is the time required for an alloy to pass the solidification range.

In Paper III, the cooling rate was computed for an Al-based amorphous alloy. Consequently, the cooling process without phase change is characterized by the duration during which primarily crystallization occurs. It was therefore assumed that crystallization occurs between the liquidus temperature T_{liq}, and the glass transition temperature, T_g:

$$CR = \frac{T_{liq} - T_g}{t_{liq} - t_g} \tag{13}$$

2.3.2.1 Model considerations to describe the cooling rate during centrifugal atomization

Assessing the cooling rate is accomplished by employing the well-established heat transfer theory [132]. This involves using models that quantify the heat exchange between a droplet and the surrounding gas within an environment characterized by high-temperature gradients. Numerous studies on droplet solidification models have been thoroughly detailed in the literature, particularly in the context of gas and impulse atomization [12,125,130,132–135]. The assessment takes into account heat removal mechanisms such as conduction, convection, and radiation. These models describe the solidification rate of a spherical droplet undergoing atomization under Newtonian cooling conditions. Heat conduction is neglected, as a uniform temperature distribution is considered. The convective heat transfer is expressed by the following equation:

$$Q_c = A_s h_g (T_d - T_A) \tag{14}$$

where Q_c is the heat flow, A_s is the total surface area of a sphere particle, T_d is the temperature of the droplet, T_A is the ambient gas temperature inside the atomizer, and h_g is the total heat transfer coefficient. And the radiative heat transfer is expressed by:

$$Q_r = A_s S_t \varepsilon \left(T_d{}^4 - T_w{}^4\right) \tag{15}$$

where S_t is the Stefan-Boltzmann constant, ε is the emissivity, and T_w is the wall temperature.

Most cooling models neglect radiation since the heat loss accounted by radiation is insignificant, so the heat transfer coefficient is evaluated in terms of the convective heat transfer h_c [136]. In the context of molten metal droplet cooling during gas atomization, the convective coefficient h_c becomes a complex function influenced by the thermophysical properties of the gas medium, the droplet size, and its relative velocity with the gas[137]. A common approach to quantify h_c has been the utilization of semi-empirical equations [4-10], wherein the Nusselt number Nu is averaged across the entire droplet surface. The comprehensive structure of these semi-empirical equations for calculating the effective heat transfer coefficient includes the Reynolds number Re, which describes the flow field, and the Prandtl number Pr, which is the ratio of momentum and heat transport, such as:

$$Nu = h_c \frac{d}{k_g} = a + cRe^m Pr^n \tag{16}$$

where h_c is the convective component of the heat transfer coefficient, and k_g is the thermal conductivity of the gas. Further details regarding the Reynolds number (Re) and the Prandtl number (Pr) are detailed in Paper II. The coefficients a and c, as well as the exponents m and n, are inherent to each system and must be determined experimentally.

As shown in **Table 1**, numerous Nusselt number correlations for spheres and droplets have been established in diverse studies, each equation incorporating constants derived from experimental data [138]. Hence, a comprehensive examination of the experimental conditions related to the diverse Nusselt number empirical correlations is crucial for determining their applicable range and validity. The variables included in each equation are presented in the subsequent paragraphs.

Table 1. *Empirical correlations used for calculating the Nusselt number.*

Ranz and Marshall [139]	$Nu = 2.0 + 0.6Re^{1/2}Pr^{1/3}$
Whitaker [140]	$Nu = \left(0{,}4Re^{1/2} + 0{,}06Re^{2/3}\right)Pr^{1/4}\left(\dfrac{\mu_A}{\mu_s}\right)^{1/4}$
Lewis and Gauvin [141]	$Nu = (2 + 0.515Re^{0.5})\left(\dfrac{\rho_A \mu_A}{\rho_s \mu_s}\right)^{-0.15}$
Fiszdon [142]	$Nu = (2 + 0.6Re^{0.5}Pr^{0.33})\left(\dfrac{\rho_A \mu_A}{\rho_s \mu_s}\right)^{0.6}$

Lee and Pfender [143]	$Nu = (2 + 0.6Re^{0.5}Pr^{0.33})\left(\dfrac{\rho_A \mu_A}{\rho_s \mu_s}\right)^{0.6}\left(\dfrac{c_{p,A}}{c_{p,s}}\right)^{0.38}$
Gnieliski [143]	$Nu_{lam} = 0.644Re^{1/2}Pr^{1/3}$; $Nu = \dfrac{0.037Re^{0.8}Pr}{1 + 2.443Re^{-0.1}(Pr^{2/3} - 1)}$
Yearling and Gould [143]	$Nu = 2 + 0.584Re^{1/2}Pr^{1/3}\left(1 + \sigma_{ti}^{0.843}\right)$
Duan [144]	$\dfrac{Nu_\infty}{Pr^{0.4}} \cong \dfrac{Rec_{DF}}{12\left(1 + \dfrac{0.11Re}{1 + 5000/Re}^{0.4}\right)}$
Wiskel [134]	$Nu = \dfrac{2B}{K_s(m+1)}\dfrac{T_s^{m+1} - T_A^{m+1}}{T_s - T_A} + \left(0.4T_s^{1/2} + 0.06Re_s^{2/3}\right)Pr_s^{2/3}\left(\dfrac{\mu_A}{\mu_s}\right)^{1/4}$

Symbols:
Nu = Nusselt number; Re = Reynolds number; Pr = Prandtl number; Nu_lam= laminar Nusselt number; Nu_turb= turbulent Nusselt number; T = temperature; μ = dynamic viscosity; ρ = density; C_p = specific heat; C_DF = drag coefficient; σ_ti = relative turbulence intensity.
Index:
A = property calculated at ambient temperature; S = property calculated at sphere surface temperature;

Ranz and Marshall correlation

One of the widely adopted correlations is the Ranz and Marshall correlations [139]. This correlation was established by measuring water droplet temperatures in an air atmosphere at ambient temperatures ranging from 85°C to 200°C. The Nusselt number *Nu* was determined by balancing heat loss from droplet evaporation with heat gain from hot air at a constant droplet temperature. This empirical equation was proposed for Reynolds numbers between 0 and 200 and Prandtl numbers ranging from 0.68 to 0.72. Despite the relatively small temperature difference tested (maximum of 115°C), which may be considered marginal for most metallurgical systems, the Ranz-Marshall equations have been extensively employed [134].

Extensions of the Ranz-Marshall correlation to elevated temperatures have been suggested for plasma spray applications. Fizdon et al. [142] measured the temperature of spherical particles (30-67 μm) in a plasma flame with temperatures reaching up to 8000 K and particle velocities of 540 m/s. They introduced a term to consider changes in density and viscosity. Lee & Pfender [143] adopted a similar approach, proposing the same correlation with an additional correction for specific heat. However, it is important to note that these last two correlations are tailored for plasma properties, limiting their applicability to ideal gases as they significantly impact the Reynolds and Prandtl numbers [145].

Gnielinski [143] introduced a correlation that integrates both laminar (*Nu_lam*) and turbulent (Nu_turb) Nusselt numbers, extending the validity of the Ranz-Marshall correlation to Reynolds numbers up to 10^6 for 0.7 < *Pr* < 600, and Yearling and Gould [143] incorporated a term for the

relative turbulence intensity, denoted as σ_{ti} into a correlation that closely resembles the equation derived by Ranz and Marshall.

Whitaker correlation

An alternative commonly employed correlation is the Whitaker correlation [140]. This correlation addresses both the variability of heat flow around spheres, cylinders, or packed beds and the impact of temperature-dependent viscosity. It assumes that fluid flow around a droplet comprises two phenomena: a laminar flow regime and the wake region. The correlation is valid for $3.5 \leq Re_A \leq 7.6 \times 10^4$, $0.71 \leq Pr_A \leq 380$ and $1 \leq (\mu_A / \mu_s) \leq 3.2$. The largest temperature difference observed in different experiments was 70 K. The ratio of dynamic viscosities at the surface temperature and ambient temperature is also considered. However, to calculate a convective heat transfer coefficient from this Nusselt number, it is suggested to use the thermal conductivity at ambient temperature, which may introduce an error for $T_s \gg T_A$ [145].

In more recent investigations, Duan et al. [12] established a relationship based in the analogy between sphere drag and heat transfer. They derived this relationship by building upon the Whitaker correlation for the Nusselt number and incorporating additional experimental data related to fluid flow and heat transfer.

Wiskel correlation

Many Nusselt number correlations are derived for small temperature differences across the boundary layer between a molten droplet and the surrounding gas. Thus, a critical consideration is where to measure the thermophysical properties of the gas, especially in systems where the gradient across the boundary layer can reach up to 1000 K, as observed in atomization processes. In such cases, the thermophysical properties of the gas vary significantly from the droplet surface to the atmospheric temperature. These variations can substantially influence the thermal transport between the gas and droplet.

This led Wiskel and Henein [134,146] to introduce a correction to address the temperature dependency of thermal conductivity within the boundary layer, particularly for significant temperature disparities of up to 800 K between the droplet and the surrounding gas medium. The authors validated their model by producing aluminum droplets through impulse atomization, and they experimentally and theoretically determined the solidification distance of these droplets.

Finally, it is noteworthy to highlight the recent work by Ellendt et al.[143], who introduced a computational model addressing non-isothermal flow around a sphere under high temperature differences. The study analyzed the average convective heat transfer coefficient and compared it with the correlations mentioned earlier for the Nusselt number. The findings indicated that the data aligns well with the well-established Ranz and Marshall and Whitaker correlations, while other correlations exhibited poor agreement with the results.

2.3.3 Correlation validation in the centrifugal atomization process

The limitations associated with extrapolating the correlations to high-temperature multiphase flow systems are acknowledged by numerous researchers [134,137,145]. Additionally, various authors employ distinct correlations in their atomization systems, with gas thermophysical properties assessed under different conditions, including ambient temperature T_A [147], film temperature T_f [148], or droplet temperature T_d [149]. However, none of these studies have been conducted using the centrifugal atomization technique.

Although all atomization processes are categorized as rapid solidification processes [22], they inherently differ in how they produce particles, necessitating attention to these distinctions. In impulse atomization, particle velocities are generally two orders of magnitude lower than in centrifugal atomization [39,134]. Gas atomization lacks consensus on the droplet formation location due to recirculation near the gas and melt [150,151]. In centrifugal atomization, particles are rapidly expelled to a low gas temperature zone [66]. These intrinsic differences raise concerns about the applicability of models developed for gas or impulse atomization to centrifugal atomization. The pivotal question arises: which model is suitable for centrifugal atomization? Given the diverse approaches, a comprehensive investigation into a theoretical model specific to centrifugal atomization would be beneficial.

2.4 Atomization of glass-forming alloys

To date, numerous studies have investigated the atomization process of glass-forming alloys, with a predominant focus on gas atomization in aluminum-based an iron-based alloys, particularly emphasizing microstructural characterization and magnetic properties [11–13,15,16,18,20,114,152–154]. However, limited attention has been given to the production process of glass-forming alloys. An exception is the recent study by Ciftci et al.[19], which meticulously reported on the gas atomization glass-forming alloy powders, analyzing the physical mechanisms to enhance the cooling rate during this process. The authors used various alloys to develop four strategies to increase the cooling rate: increasing melt superheat temperature, employing hot gas atomization, applying spray cone cooling, and using liquid quenching. The highest cooling rates were achieved for liquid quenched particles with fully amorphous powders up to 200μm. The second-highest cooling rates were achieved with spray cone cooling with Fe-based powders that exhibited amorphous structures up to 125 μm. An elevated melt superheat temperature, ranging from 250 K to 450 K, significantly enhanced particle shape factors such as sphericity and aspect ratio. The FeCoBSiNb glass-forming alloy demonstrated the impact of hot gas atomization on cooling rates, with the relative velocity and temperature gradient compensating for each other and resulting in nearly unchanged cooling rates, consequently, the amorphous fraction remained the same. Ciftci's research has yielded significant findings, particularly in the improvement of cooling rates for atomized particles, aiming to achieve amorphous structures.

Conducting a fundamental analysis of the mechanisms that enhance cooling rates during centrifugal atomization would be highly valuable. As mentioned earlier, one of the advantages of the centrifugal atomization process is the production of spherical-shaped powder, a requirement for subsequent consolidation methods in the additive manufacturing realm.

Achieving this demands an in-depth characterization of the capabilities of the centrifugal atomization technique and a study of the necessary conditions to attain the required cooling rates for producing amorphous powder.

Methodology

The methodology employed in this PhD thesis is classified into three key elements: material selection, powder production, and powder characterization. While the experimental procedures are detailed in the individual sections of each paper, this chapter serves two distinct purposes. Firstly, it presents extra information regarding the material selection which led to the organization of each paper into a coherent sequence of tasks. Secondly, it provides a more comprehensive account of the equipment and procedures employed in the production and characterization of the resulting powder described in each of the individual papers. **Figure 14** shows a chart with the work methodology.
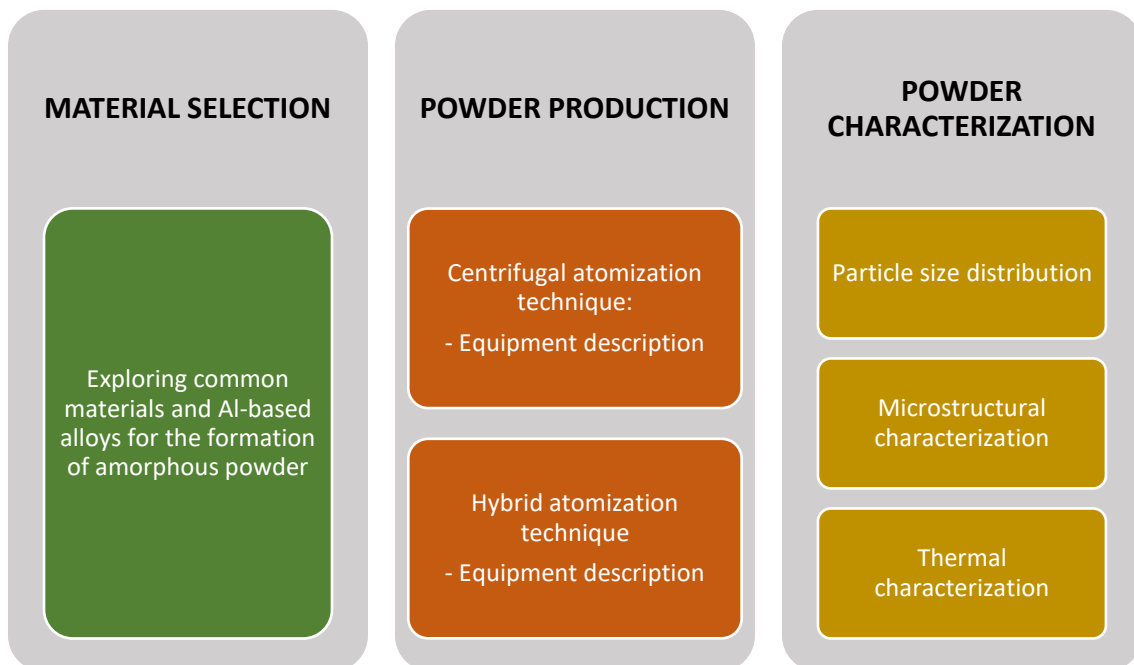
Figure 14. Work methodology chart.

3.1 Materials selection

3.1.1 Exploring common materials and Al-based alloys for the formation of amorphous powder

As discussed in the literature review, achieving an amorphous microstructure in metal powders requires high cooling rates. Before starting tests of alloys with a high potential of amorphous phase formation, it was imperative to conduct a comprehensive analysis of the cooling rates achievable through the centrifugal atomization technique. These preliminary

studies served the dual purpose of establishing the cooling rate range within which the equipment operates and devising control strategies while assessing the likelihood of attaining an amorphous structure.

In an initial approach, the objective was to enhance the cooling rate through the implementation of innovative techniques in centrifugal atomization. This involved introducing an external gas stream, a concept that will be elaborated upon in the following section. For this phase of the research (Paper I), electrolytic copper was selected due to the equiaxed microstructure it produces. This microstructure facilitated the measurement of grain size as a function of gas flow rate, therefore allowing the detection of changes in cooling rates.

In the next step of the research (Paper II), Al4%Cu was used to quantitatively evaluate the cooling rates experienced during centrifugal atomization. This choice was based on the well-documented thermophysical properties of the alloy, as well as the availability of empirical correlations in the existing literature for calculating the corresponding cooling rates.

Finally (Paper III), following an extensive review of the literature, $Al_{86}Ni_8Y_{4,5}La_{1,5}$ alloy was identified as having a high probability of achieving complete amorphous or an amorphous phase formation. This alloy has been previously manufactured using the melt spinning method [155] with the maximum thickness obtained through this process measuring 785 µm. The raw materials used for designing this Al-based amorphous alloy are shown in **Figure 15**.

Figure 15. *Raw materials used for the preparation of $Al_{86}Ni_8Y_{4,5}La_{1,5}$ alloy.*

The nominal composition of the alloys along with the details about the raw materials used, can be found in **Table 2**. The different elements and alloys were chosen to explore the diverse approaches in the investigation of the cooling rate and the amorphous powder formation via centrifugal atomization.

Table 2. *Selected alloys including used in this study.*

Alloy (at%)	Nomenclature	Raw materials used (wt%)
Electrolytic Cu (99,9%)	Cu	Cu (99,9%)
$Al_{98,26}Cu_{1,74}$	Al-4%Cu	Al 1050 (99,5%) Electrolytic Cu (99,9%)
$Al_{86}Ni_8Y_{4,5}La_{1,5}$ (at %)	AlNiYLa	Master alloy Al90Y10 Eutectic La12Ni88 Lump Al12Y88 Ni (99,9%)

3.2 Powder production

3.2.1 Description of the centrifugal atomization equipment

The powders in this PhD thesis were manufactured employing the centrifugal atomization pilot plant designed at *Fundació EURECAT.* A schematic representation as well as a picture of the centrifugal atomization setup can be observed in **Figure 16**. This system comprises four key components: the atomization chamber, the induction melting system equipped with a crucible, the spinning disk, and the vacuum and inert gas system.
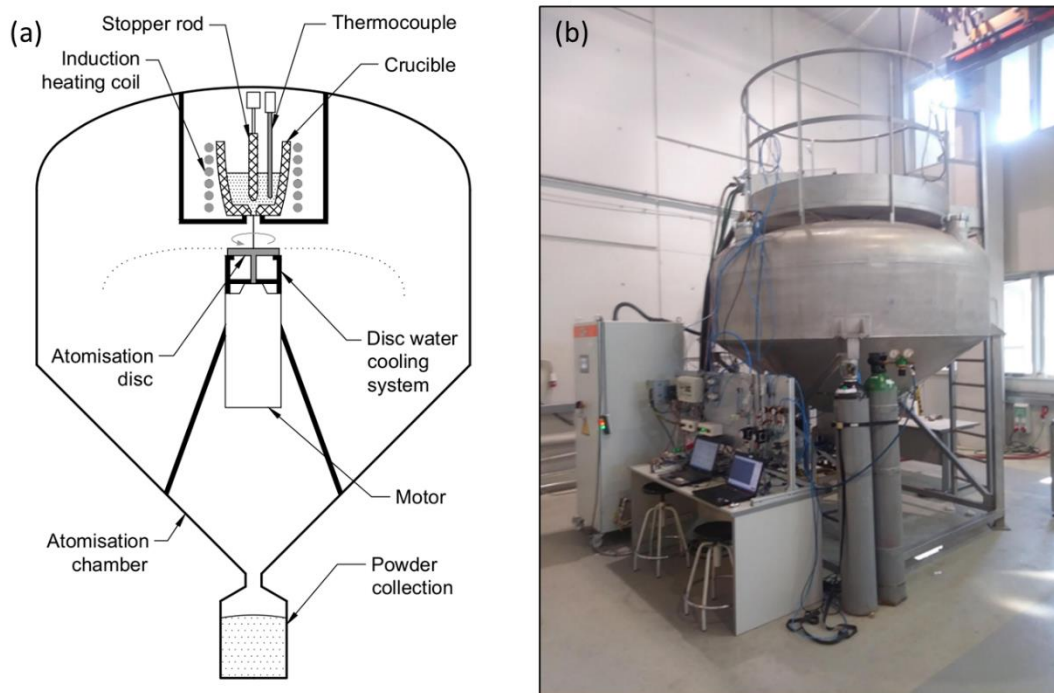

Figure 16. *a) Schematic representation of the centrifugal atomizer; b) centrifugal atomization pilot plant.*

The atomization chamber's dimensions are 2.5 meters in diameter and 4 meters in height, a design intended to ensure that particles, driven by the centrifugal force of the atomization disk,

can adequately solidify prior to making contact with the chamber walls. Additionally, the lower cone of the atomization chamber is inclined to facilitate the seamless sliding of particles towards the collector, situated at the chamber's lower cap. The atomization chamber incorporates two access points, one at the top and another at the bottom, which serve as entryways for maintenance activities. These access points are securely sealed with their respective caps when atomization procedures are conducted, ensuring a closed and controlled atmosphere, which is vital to prevent material contamination and oxidation during the atomization process.

To establish a controlled atmosphere with an inert gas, the first step involves creating a vacuum inside the atomization chamber. **Figure 17** shows the two vacuum pumps in series that are used. This combination is typical for the chamber's volume and the required vacuum level. The pumps are, one from the the Leybold® brand, model D-65B, which serves as the primary pump, and the other from the Aerzen® brand, model GMA 10.1 HV. The maximum vacuum level that can be attained with these pumps is $1 \cdot 10^{-3}$ mbar, which is the level needed in the atomization chamber. Once the vacuum level is achieved, the atomization chamber is backfilled with inert gas.
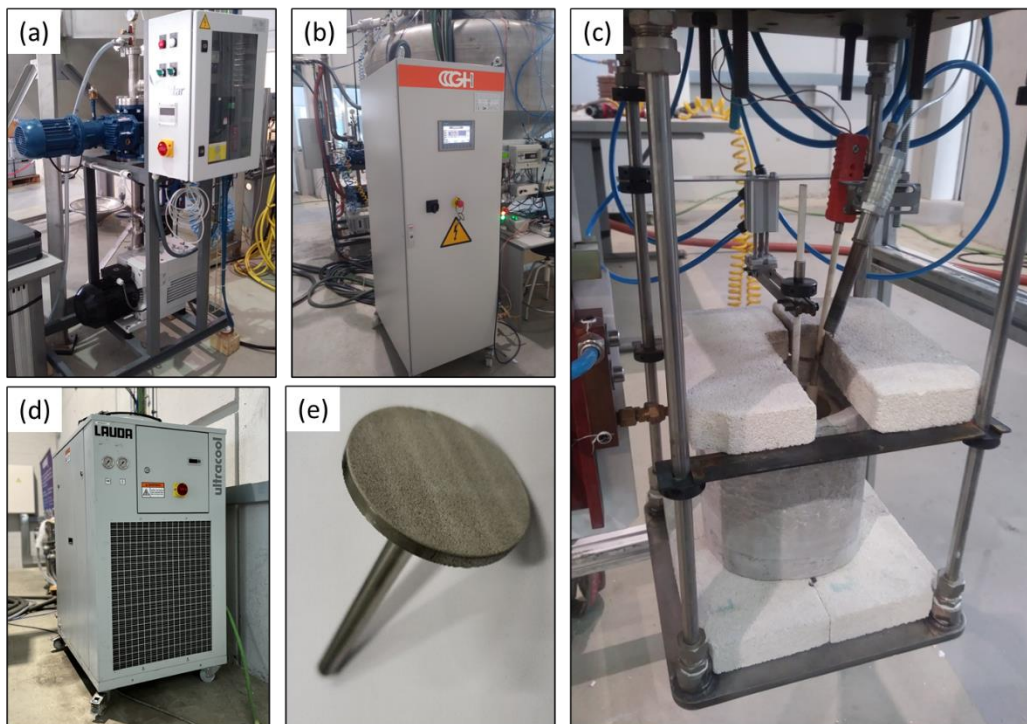
Figure 17. *a) Vacuum pump in series; b) induction heating device; c) coil with crucible system; and d) the water refrigerator system, and e) the atomization disk.*

For melting the metal alloys, an induction-heating device is employed. The metal is placed into a crucible located in the upper part of the chamber inside an induction coil. This integral system is composed of an induction generator, the induction coil and a water chiller system, shown in **Figure 17b**, **17c** and **17d**. The inductor provides a predetermined voltage to the coil, and the flexibility of this voltage is modifiable by adjusting the system parameters. The inductor generator is the 50SM150 model, manufactured by GH Electrotermia® with frequency of 50-150 kHz and a power supply of 62,5 kW. The Ultracool UC Midi chiller water refrigerator from the brand Lauda-brinkmann® is required to refrigerate the induction coil and the inductor generator components.

The induction coil heats the crucible, causing the metal to melt. The crucible is equipped with a hole in the bottom, sealed with a stopper. Once the metal is melted, the stopper is raised, allowing the molten metal to flow downward onto the atomization disk.

The atomization disk, shown in Figure 3.4e is the most crucial component within the atomization system, responsible for breaking the molten metal into small droplets through the application of centrifugal force. Positioned inside the atomization chamber just below the melting equipment, the atomization disk setup is a highly intricate component. It demands precise calibration to withstand high-speed rotations without misalignment or imbalance. Additionally, it must endure elevated temperatures and resist corrosion from de melt. To prevent overheating, the atomization disk is equipped with a cooling system, either water-based or inert gas-based. In general, the water-cooling system is used for metals with a high melting point, while the gas cooling system is employed for metals with a lower melting point. In the case of employing the water-cooling system, the incoming water is split into two streams. One flow is directed to cool the electric motor of the disk, while the other circulates through the disk's own cooling circuit. For the inert gas cooling system, inert gas is obtained from gas cylinders. In the atomization procedures conducted during this PhD, either nitrogen or argon was commonly used.

The rotation of the atomization disk is driven by an electric motor capable of reaching speeds of up to 60,000 rpm, with the disk securely fastened to the motor using a clamp. The motor is the IBAG® HF60.3560 CFP. To protect the internal components of the motor from damage, an air-seal system is employed, expelling air through the motor's seals to prevent the ingress of foreign particles. Furthermore, the motor includes a cooling circuit to prevent overheating. It also features a 3 KVA frequency converter, allowing for adjustments to the input frequency up to a maximum of 1,000 Hz, and a braking resistor.

Following the atomization process, the powder is collected in the lower cone of the atomization chamber within the collector, which can be detached from the atomization chamber. This feature allows for easy transportation of the powder to proceed to the subsequent steps.

3.2.2 Description of the hybrid atomization equipment

The hybrid atomization process outlined in Paper I enhances the conventional centrifugal atomizer by introducing an external gas stream at the disk's periphery. This technique consists of two sequential steps: first, the molten metal is disintegrated into fine particles through centrifugal atomization as explained in the previous section, and subsequently, these particles undergo rapid solidification through the hybrid gas system where the droplets are cooled by a gas stream. The combination of these two techniques results in high cooling rates, prompting modifications in the material's microstructure. It is worth noting that while this process is referred to as a 'hybrid atomization system,' it distinguishes itself from other hybrid systems documented in the literature by its distinct underlying concept. The possibility of patenting the hybrid atomization equipment is being considered, which is why images cannot be shown due to confidentiality.

3.3 Powder characterization

As indicated in Figure 3.1 powder characterization is divided into three parts:

I.   **Sieving and particle size distribution:** In each experiment, the resulting powder was subjected to separation using sieves in accordance with the standard procedure ASTM-B214-07. Filtra® stainless steel sieves with aperture sizes ranging from 20 to 600 μm were employed. These sieves were arranged in a consecutive stack, organized in order of increasing aperture size, with the widest opening at the top and a collection pan positioned beneath the bottom sieve. Approximately 200 grams of a standard test specimen were poured onto the top sieve, and the stacked sieves were placed onto the FTL-0150 digital electromagnetic sieve shaker from the brand Filtra®. Sieving was carried out for a duration of 15 minutes to obtain distinct fractions of each alloy.

II.   **Microstructural characterization:** the samples underwent preparation through conventional metallographic methods, which varied depending on the sample type. For the powders, a cold mounting process was employed, involving a two-component epoxy resin comprising a liquid resin and a liquid hardener. These components were blended in a plastic cup, and the resulting homogeneous mixture was then combined with a small quantity of powder within a mold. Subsequently, the samples were left to harden for a period of 24 hours. The procedures for grinding, polishing, and etching of the powder samples are detailed in their respective papers.

Microstructural analyses were conducted utilizing Light Optical Microscopy (LOM) and Scanning Electron Microscopy (SEM). The optical microscope from the brand Nikon®, and model Epiphot 200, in conjunction with image processing software ANALYSIS was employed to measure the grain size in the copper powder and the Secondary Dendrite Arm Spacing (SDAS) in the Al-4%Cu alloy. Additionally, the Scanning Electron Microscope from the brand ZEISS FESEM® and model Ultra Plus was used to assess the particle morphology and surface characteristics of the powders.

X-ray diffraction analysis was conducted on the sieved Al alloy powder in paper III to confirm the presence of amorphous material, even in high-size powder fractions. XRD patterns were recorded using the difractometrer X'Pert PRO MPD from the brand Malvern PANalytical®, with Cu Kα radiation (λ = 1.5418 Å) within the 5 to 100° 2θ range, utilizing a 0.017° step, and a measurement time of 100 seconds per step.

III.   **Thermal characterization:** The volume fraction of the amorphous (V_f) phase in the different powder fractions produced by centrifugal atomization in paper III, was determined through the differential scanning calorimetry (DSC) technique, using the DSC1 equipment from the brand Mettler Toledo®.

Results

PAPER I

Effect of Processing Parameters on Copper Powder Produced by Novel Hybrid Atomization Technique

Published in: Powder Metallurgy

Impact Factor 2018: 1.149

Journal Quartile: Q2

Effect of processing parameters on copper powder produced by novel hybrid atomisation technique

Sasha Alejandra Cegarra Salges, Jordi Pijuan, Ricardo Hernández & Maria Dolores Riera

Published online: 04 Feb 2020.

Submit your article to this journal

Article views: 31

View related articles

View Crossmark data

IoM³
The Institute of Materials,
Minerals and Mining

Taylor & Francis
Taylor & Francis Group

Check for updates

RESEARCH ARTICLE

Effect of processing parameters on copper powder produced by novel hybrid atomisation technique

Sasha Alejandra Cegarra Salges [a], Jordi Pijuan [a], Ricardo Hernández[a] and Maria Dolores Riera [b]

aDepartment of Processing Modelling and Simulation, Technological Centre EURECAT, Manresa, Spain; bDepartment of Mining, Industrial and ICT Engineering, Technical University of Catalonia-(UPC), Manresa, Spain

ABSTRACT

In the present work, a novel design of centrifugal atomiser for producing pure copper powder was studied. The novel complementary hybrid system provides an external stream of gas to increase the cooling rate of the atomised particles. Effects of the operating parameters, such as disc rotating speed and gas flowrate on the morphology, particle size distribution, cooling rate and microstructure, were analysed. It was evidenced from the experimental results that the median particle size in the novel atomisation process is mainly controlled by centrifugal disintegration. The microstructure of the produced powders was equiaxed and the grain size decreased with increasing gas flowrate. The cooling rate experienced by centrifugal atomised Cu powders was studied via numerical formulation estimated to be 10^4–10^6 K s^{-1}. The results show that the cooling rate is a strong function of particle size and increasing the rotating disc speed also increased the cooling rates.

Introduction

Centrifugal atomisation of melt has been used for metal powder production for decades [1–3]. This process is able to produce spherical particles, with less impurity and narrow size distribution at a low production cost in terms of energy consumption [4]. Centrifugal atomisation is considered a Rapid Solidification Process which involves high rates of cooling during solidification (10^4–10^6 K s^{-1}) [5]. During this process, raw materials are melted in an inert gas atmosphere. The liquid metal stream is ejected onto a high-speed rotating disc which breaks up the liquid into a spray of droplets, which solidify in flight to form powder. Depending on the atomisation parameters, particles are produced either by direct drop formation, by ligament disintegration or by film disintegration from the disc edge [6]. At a low volumetric flowrate and low disc speed, direct droplet formation is observed at the edge of the disc. With increasing volumetric flowrate and disc speed, ligament disintegration is the main mode of flow behaviour. Film disintegration appears at even higher flowrates and disc speeds and the surface of the atomising is covered by a continuous film moving from the centre to the periphery of the disc. The particle diameter has been predicted using the equation [7]:

$$d_{50} = \sqrt{\frac{6\sigma}{\rho\omega^2 R}} \qquad (1)$$

where σ is the surface tension (N m^{-1}), ρ is the density (kg m^{-3}), ω is the angular velocity (rad s^{-1}) and R is

the atomiser disc radius (m). This equation implies that increasing angular speed will result in smaller particle size.

The present work aims to investigate the influence of operating parameters on the new atomisation process. This study reports the effects of the gas flowrate and rotational speed on the median particle size, microstructure and cooling rate of pure copper powder, produced by the novel hybrid atomisation system.

Basic principle

A new complementary hybrid system has been added to the centrifugal atomisation equipment in order to increase the cooling rate of the atomised particles. The high rates of cooling could lead to significant modifications on microstructures. The advantage of this technique is to be able to design new metal powders of alloys beyond the equilibrium. Centrifugal atomisation gives coarse mean powder sizes (>45 μm) that do not meet the requirements for various advanced powder metallurgy manufacturing technologies [8]. Thus, a new way has been thought to promote a high cooling rate and a further break up of the droplets.

The hybrid atomisation process described in this study is the improvement of a conventional centrifugal atomiser with the addition of an external stream of gas at the periphery of the disc. This technique consists of two steps in the following order: the disintegration of the molten metal into fine particles through centrifugal atomisation followed by rapid solidification of these

particles through the hybrid gas system. The advantages of this specific design are that the feed material is first spread out by a spinning disc due to centrifugal forces, and once atomised, the droplets are rapidly cooled by a stream of gas. The combination of both techniques leads to high cooling rates that promote modifications on the material microstructure which results in high-quality powder with an increasing demand as new technology emerge that can make use of their unique characteristics. Although this process is called 'hybrid atomisation system', it is only to remark the combination of two techniques. The concept behind it is different than other hybrid systems documented in the literature [9].

Experimental procedures

The centrifugal spinning disc unit with the hybrid complementary system is shown in Figure 1. This equipment contains four parts: the atomisation chamber, the induction melting system with crucible, the spinning disc with the hybrid system and the vacuum and inert gas system.

Electrolytic copper with a purity of 99.9% was used as a starting raw material. The Cu was induction melted in a crucible. The melt stream flowed through a nozzle under gravity onto the atomisation disc, atomising the melt stream.

The main processing parameters for this study were the disc speed of atomisation and the gas flowrate from the hybrid system. A set of test runs were carried out with the variation ranges of the main parameters as shown in Table 1. 1 kg of Cu was melted for each experiment. In any group of experiments, only one parameter was varied with the others being fixed.

After each atomisation, each of the as-produced powders was sieved and weighed. However, due to a
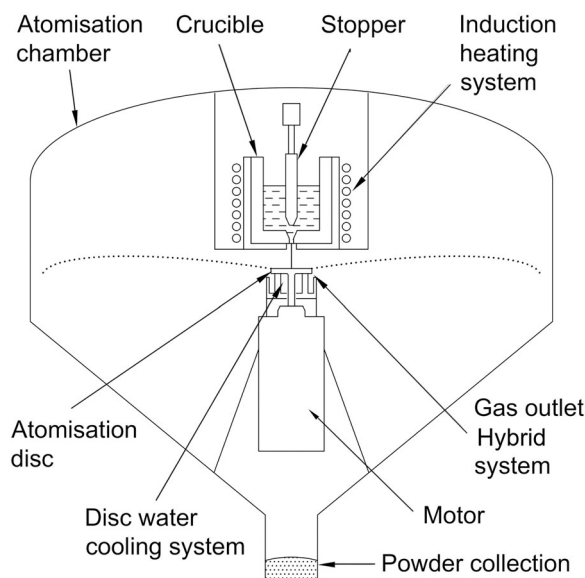
Table 1. Processing experimental parameters of atomisation.

	Pouring temperature of the melt = 1200℃, graphite disc diameter = 40 mm; hybrid gas composition = Nitrogen, chamber gas pressure (N_2) = 0,7 bar; melt flowrate ~ 75 kg h^{-1}
Disc speed (rpm)	Gas (N_2) flowrate (L min $^{-1}$)
15,000	0–100–200
25,000	0–100–200
35,000	0–100–200

large concentration of flakes and splats, all particles larger than 355 μm were discounted, corresponding to approximately 35% of the atomised material. The sampled powder was loaded onto a series of sieves and shaken on a sieve shaker for 15 min. The powder weight retained on each sieve was determined. The sieve data were plotted on a log-normal plot to evaluate its particle size distribution and median particle size. The samples were selected and they were mounted in cold resin and metallographically prepared for microstructural examinations. The samples were polished and etched using a reagent, with the composition of 100 mL H_2O – 100 mL C_2H_5OH – 19 gr $Fe(NO_3)_3$. The morphology of the atomised particles was observed by using Ultra Plus Field Emission Scanning Electron Microscope (SEM). The microstructure and average grain sizes of powders were analysed with a Nikon Epiphot 200 optical microscope. Due to the lack of a standard test method to determine the average grain size in metal powders, the criteria used in this study was to measure the mean grain size area in five different micrographs for each sample from each atomisation.

Results and discussion

Particle size distribution

Figure 2(a) shows the particle size distribution of copper metal powders produced by centrifugal atomisation for different hybrid gas flowrates at a constant disc speed of 25,000 rpm. It can readily be seen that the gas flowrate does not affect the particle size distribution significantly lacking a clear tendency and having a median particle size (dm) from 72 μm to 76.9 μm with a standard deviation of 1.61–1.67. As opposed to Figure 2(a), Figure 2(b) demonstrates that the particle size distribution of the Cu powder tends to be finer with increasing rotational disc speed with a median particle size range between 68.1 μm and 88.3 μm and a standard deviation of 1.53–1.75 [7,10,11].

It is also observed from Figure 3 that the median particle size of produced copper powder decreases with increasing rotational disc speed, with similar values for conventional centrifugal atomisation and hybrid atomisation Thus, the final particle size obtained using the hybrid atomisation system is mainly
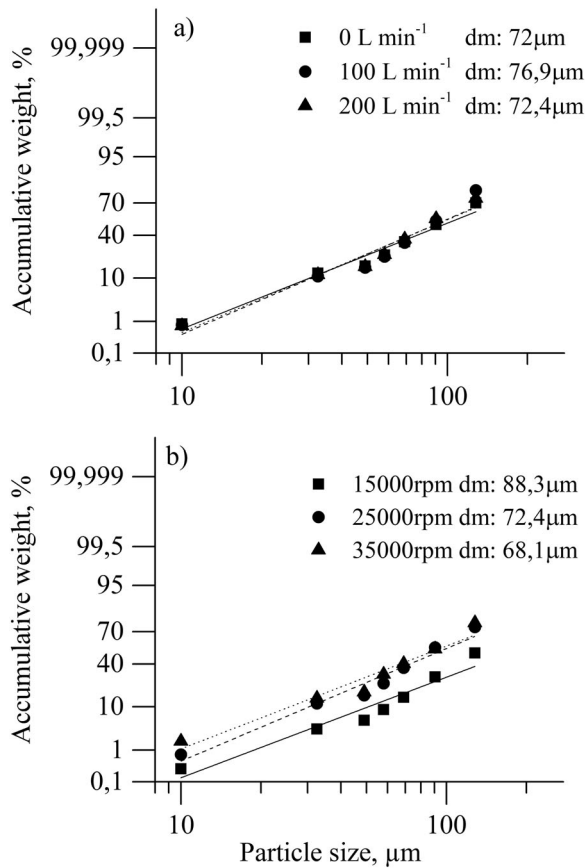

Figure 1. Schematic diagram of the centrifugal atomisation equipment with the hybrid complementary system.

Figure 2. Particle size distribution of copper powder at (a) different hybrid gas flowrate and a rotating disc speed 25,000 rpm and (b) different rotating speed and gas flowrate 200 L min^{-1}.

controlled by the centrifugal disintegration. The medium particle size of produced copper powder from the present study is smaller than that predicted by Equation (1). Thus, the results imply little slippage of melt on the surface of the atomising disc, a consequence of an excellent wetting between melt and the graphite disc surface.
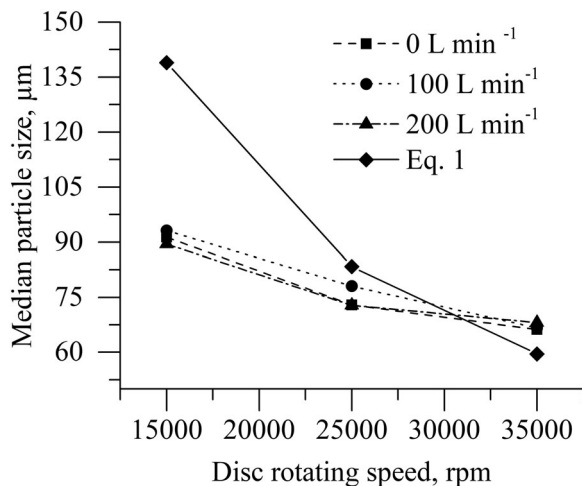

Figure 3. Effect of rotating disc speed on median particle at different hybrid gas flowrates.

Morphology of Cu powder

SEM micrographs in Figure 4 reveal the morphology of the Cu powder for conventional centrifugal atomisation and with the hybrid complementary system. As illustrated in the same figure, the morphology of these powders is spherical or nearly spherical. In addition, few satellites are found around main particles under both atomisation conditions and no hollow particles were detected.

Grain size as a function of gas flowrate

The microstructure of atomised particles for both conventional and hybrid atomisation was equiaxed and mainly affected by the particle size. The mean grain size area of the particles decreased with decreasing particles size. This was due to smaller surface area/volume ratios and a higher heat content of the large particles, which resulted in lower cooling rate and larger microstructure [12].

Micrographs from Figure 5 show that the particle grain size is highly variable, which indicates the complexity of the process even in the same range of particle size. If considering spherical grains that nucleate randomly in a given particle, as the grains grow, they will eventually impinge on one another determining the variability of the grain sizes, even within the same range of grain size. These effects are explained on the basis of competing nucleation and growth phenomena during solidification of the atomised particles [12]. Within this process is mandatory to add the complexity of the particle break up from the melt, particle trajectory and particle velocity. Nonetheless, according to the literature and as shown in this study, a higher cooling rate will result in a decrease in grain size [12].

According to Figure 6, when the gas flowrate increases from 0 to 200 L min^{-1}, the mean grain size of the particle decreases, having the same tendency for different speeds of atomisation. As can be seen from the figures, the effect of gas flowrate is stronger at lower disc rotational speeds. At 15,000 rpm the average grain size was reduced by half for 106 μm particles. This can be explained in terms of disc-particle dynamics. At lower speeds, the velocity of the droplet at the edge of the disc is lower, accounting for a higher contribution of the hybrid vertical component. However, the gas flowrate implemented in this study has no effect on the particle size distribution as discussed previously. These results confirm that the grain size has a stronger dependence on the cooling rate relative to that of particle size [13].

A finer microstructure is a consequence of higher cooling rates. Thus, from the results the cooling rate is expected to increase with increasing hybridisation gas flowrate at a constant disc speed and with increasing disc speed at a constant gas flowrate. However,
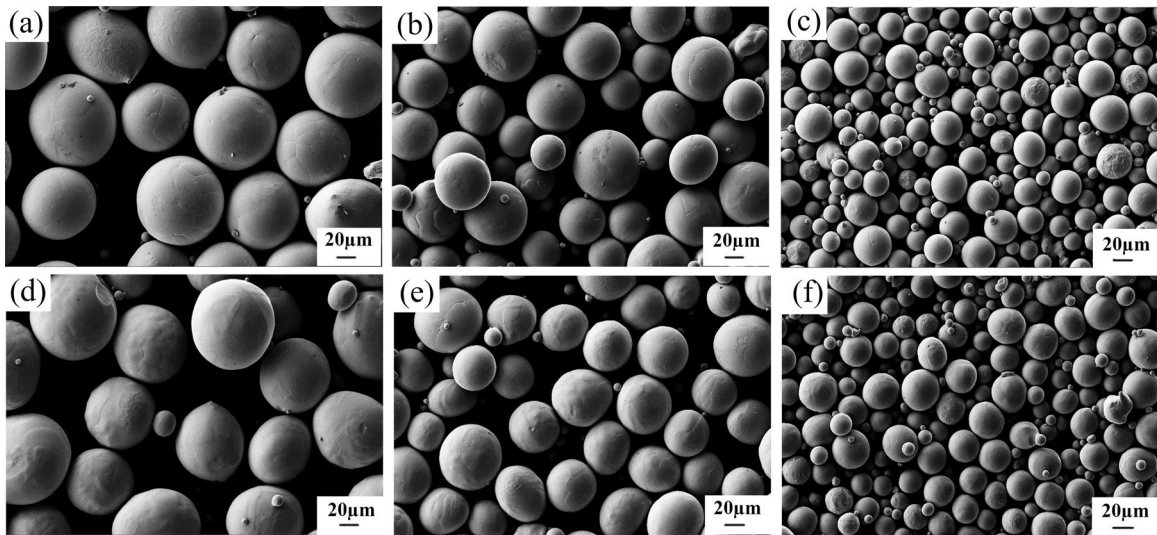
Figure 4. SEM images of Cu powders by hybrid atomisation at 200 L min^{-1} (a–c) and centrifugal atomisation (d–f) at 35,000 rpm for different particle size: (a,d) 106–75 µm, (b,e) 75–45 µm, (c,f) 45–20 µm.

experimentally the effect of disc speed on grain size was not evident.

Cooling rate analysis

The cooling rate process of the atomised particles was theoretically calculated assuming the concept of a

Figure 5. MO images of Cu powders by hybrid atomization: (a, b) 106–75 µm.

single particle which is projected into a gas flow in the same direction as the velocity of the particle. The complexities of the system require additional assumptions [4] reported below.

For conventional centrifugal atomisation, the initial droplet velocity is assumed to be the peripheral tangential velocity of the disc. When using the hybrid complementary system, the vertical component velocity is also taken into account. Therefore, the total droplet velocity increases and the convection heat transfer coefficient is higher.

According to Yule and Dunkley [4], after the droplet is completely solidified, it furthers cools down in the solid state. This process can be evaluated from the sum of heat convection (Q_c) and heat radiation (Q_r) using the following equation:

$$Q_{ave} = A_s h(T_d - T_A) + A_s \varepsilon S_T(T_d^4 - T_A^4) \qquad (2)$$

where h is the convection heat transfer coefficient (W.m^{-2}.K^{-1}), A_s is the total surface area of sphere particle (m^2), ε is the emissivity (0.52, according to [4]), S_T is the Stefan–Boltzmann constant (5.67 × 10^{-8} W.m^{-2}.K^{-4}), T_d is the temperature of the droplet (K) and T_A is the ambient temperature of the atomisation chamber.

Fuqian et al. [14] evaluate the convection heat transfer coefficient in terms of the relationship between Reynolds Number (Re), the Nusselt number (Nu) and Prandtl number (Pr):

$$h = \frac{K_g}{d}\left[2 + 0,6\left(\frac{V_d \rho_g d}{\eta_g}\right)^{1/2}\left(\frac{C_g \eta_g}{K_g}\right)^{1/3}\right] \qquad (3)$$

where K_g is the thermal conductivity of gas (W m^{-1} K^{-1}), d the diameter of a droplet (m), V_d the relative velocity of the droplet (m s^{-1}), ρ_g the density of the
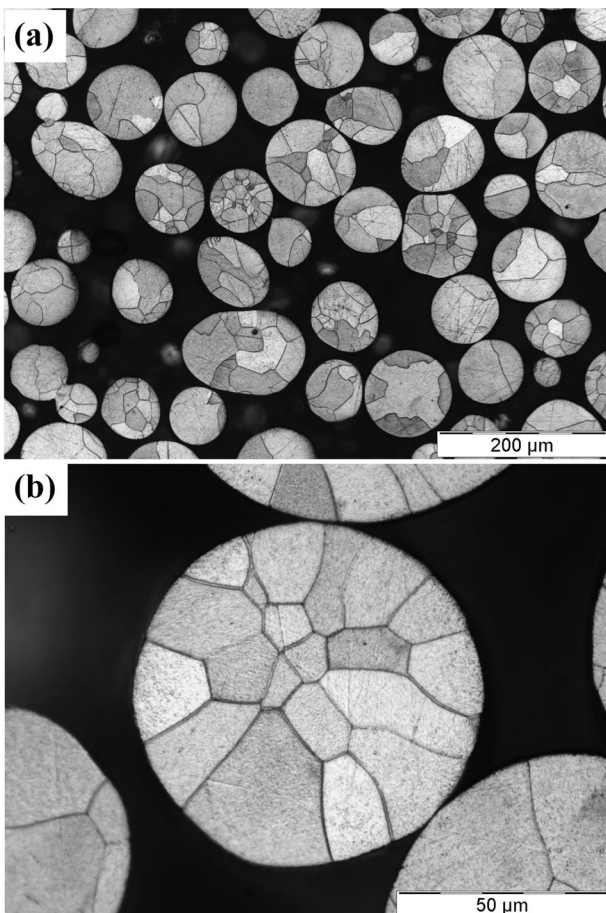
■ 45-20 μm ——— fit (45-20μm)
● 75-45 μm - - - - fit (75-45μm)
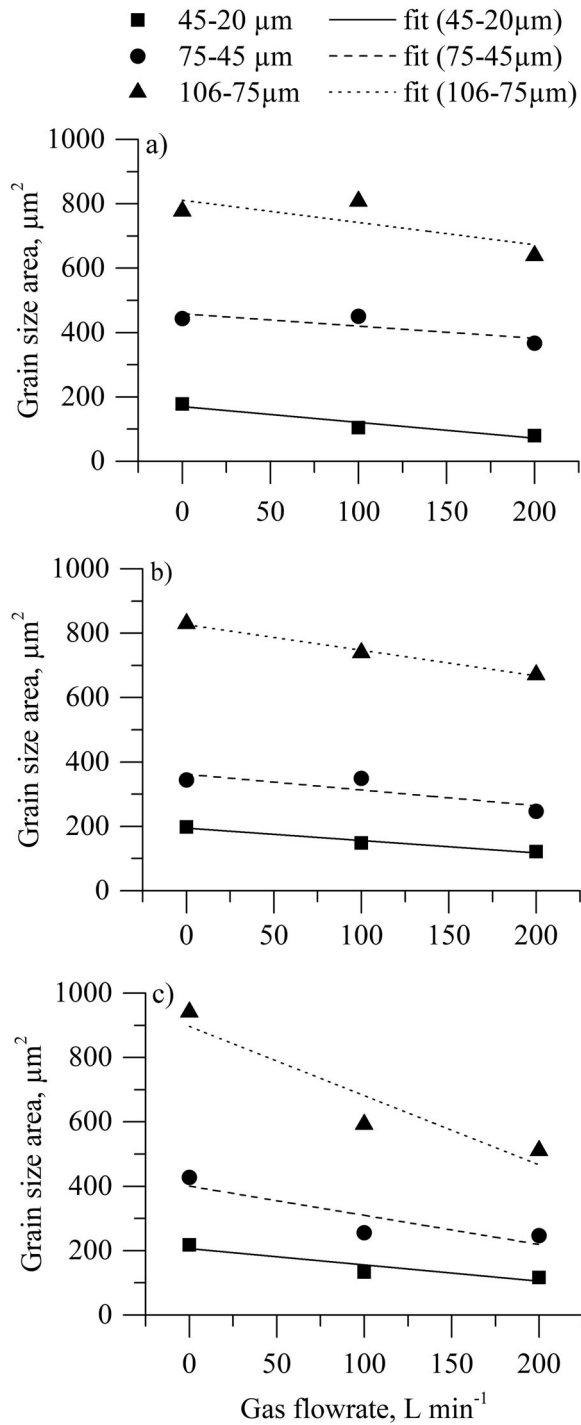▲ 106-75μm ········· fit (106-75μm)

Figure 6. Grain size area as a function of gas flowrate at different speeds of atomization: (a) 35,000 rpm, (b) 25,000 rpm and (c) 15,000 rpm.

gas (kg m^{-3}), C_g the specific heat of the gas (J Kg^{-1} K^{-1}) and η_g is the dynamic viscosity of the gas (P$_a$.s).

The energy conservation equation in a droplet is described by Fuqian et al. [14] as follows:

$$-A_s h(T_d - T_A) - A_s \varepsilon S_T(T_d^4 - T_A^4)$$
$$= V_d \rho_d C_{pd} \frac{\mathrm{d}T}{\mathrm{d}t} \tag{4}$$

where V_d (m s^{-1}) is the relative velocity of the droplet, ρ_d (kg m^{-3}) is the droplet density and C_{pd} (J kg^{-1} K^{-1}) is the droplet specific heat.

For centrifugal atomisation, Q_c dominates, so that Q_r is ignored in the subsequent analysis. Then, Zheng et al. estimate the cooling rate from the previous equation as follows [15]:

$$\frac{\mathrm{d}T}{\mathrm{d}t} = \frac{6h(T_d - T_A)}{C_{pd}\rho_d d}. \tag{5}$$

Therefore, substituting typical conditions into Equation (4), and assuming a maximum gas flowrate of 200 L min^{-1}, theoretically the cooling rate is estimated about 10^4–10^5 K s^{-1} for the equipment described in this work. Applying the same conditions to calculate the cooling rate for the conventional centrifugal atomisation process, the difference for both methods is in the order of 10^3 K s^{-1}.

Interrelationship between the atomisation parameters, such as disc velocity melt superheat, disc diameter, gas flowrate and their influence on the solidification process, are complex interactions which are common in centrifugal atomisation process and make it difficult to accurately predict the cooling behaviour of particles. As a result, the numerical analysis described in this article tends to overestimate the magnitude of the cooling rate. First of all, to simplify the analysis, heat radiation is ignored. Second, various empirical equations are incorporated into the analysis. Third, the values of the physical parameters of the melt, gas and others are not accurately known. Therefore, although an experimental validation of the cooling rate would be necessary, the numerical analysis helps to provide information to a reasonable degree.

Effects of processing parameters on cooling rate

Figure 7 shows the influence of rotational speed on cooling rate with a constant gas flowrate of 200 L min^{-1}, for rotational speeds ranging from 15,000 rpm to
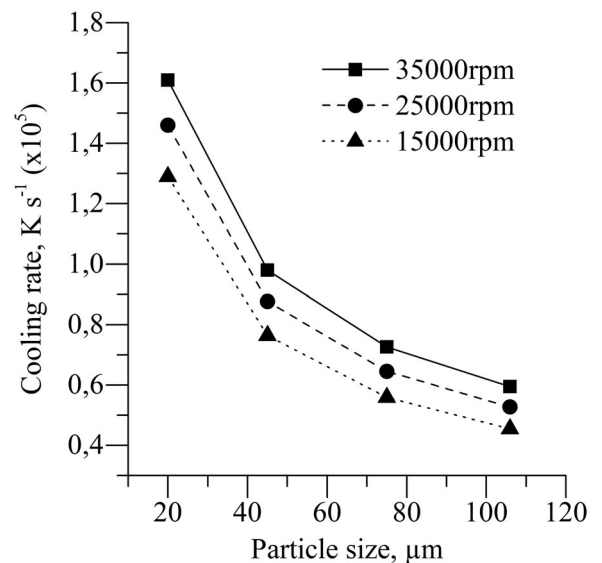

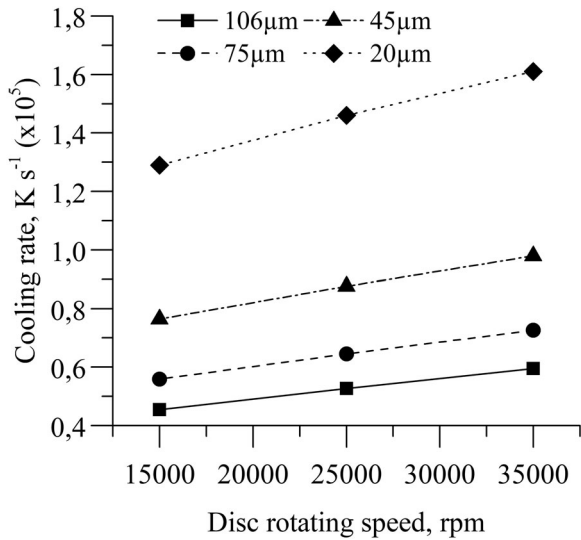Figure 7. Influence of disc speed on cooling rate with a constant gas flowrate of 200 L min^{-1}.

Figure 8. Influence of disc speed on cooling rate with a constant gas flowrate of 200 L min⁻¹ for different particle sizes.

Figure 10. Influence of gas flowrate on cooling rate with a disc speed of 35,000 rpm: (a) for different gas flowrates, (b) for different particle sizes.

35,000 rpm. It was found that the cooling rate is affected by the rotational speed. A higher disc speed applies more centrifugal force on the melt and the initial velocity of the particle is higher, this resulting in higher values of cooling rate. This finding is consistent with those previously reported by other researches [16].

Figure 8 shows that although the cooling rate increases with increasing disc speed, it mainly affected by the mean particle size. The cooling rate increases one order of magnitude for particle sizes <20 μm. This can be explained in terms of energy content; as smaller particles have smaller values of convective heat transfer coefficient.

On the contrary, Figure 9 shows that at a constant disc speed of 35,000 rpm, hybrid gas flowrates from 0 to 200 L min⁻¹ have little effect on the cooling rates. When gas flowrates increase, the change in cooling rate is not evident for specific particle size, but, as

shown previously, it is enough to change the microstructure, which suggests that the effect of hybrid gas on cooling rate is not simple. It is also noted from Figure 10 that for the same particle size the curve is flat, which illustrates the weak dependence of cooling rate on gas flowrate, but it confirms its strong function of particle size.

With these experiments, it was found that even a small change in cooling rate can affect the final microstructure of the final powder. Thus, theoretically speaking, the powder microstructure can be controlled by the cooling rate which enhances unique microstructures in attempts to produce powder of new alloys which hitherto have not been possible.

Conclusion

A new complementary hybrid system was constructed and applied to produce Cu powder. The effects of gas flowrate and rotating disc speed on the particle size distribution, microstructure and cooling rate were studied. The following conclusions could be drawn from the theoretical calculation and experimental results:

(1) Particle size distribution does not change with the hybrid complementary system but it has a strong relationship with the disc rotational speed. The particle size became finer with increasing disc speed.
(2) The particle grain size tends to decrease with the addition of the hybrid complementary system and with increasing the gas flowrates. At lower speeds of atomisation, the effect of the hybrid gas flowrate is stronger due to the extra velocity component.
(3) The cooling rate of the atomised particles increased with decreasing particle size, and it can reach more than 10⁵ K s⁻¹ for <20 μm powders.

Figure 9. Influence of gas flowrate on cooling rate with a disc speed of 35,000 rpm.

Based on the results and analysis, the cooling rate is strongly dependant on particle size and rotational speed, and it has a weak dependence on gas flowrate used in this study.

Disclosure statement

Funding

Notes on contributors

Sasha Alejandra Cegarra Salges is a Geophysical Engineer, currently a Ph.D. student at the Materials and Engineering Science Department of the Technical University of Catalonia. Her area of interest is metallic materials science and she is currently dedicated to the study of metallic powder materials produced by atomization processes at the Technological Centre EURECAT.

Jordi Pijuan is an Industrial Engineer from the Technical University of Catalonia (ETSEIAT-UPC). From 2010–2015 he has been an active researcher in Mechanical Engineering and holds a Ph.D. from Lleida Univesity (UdL). His area of interest is mechanical design and he is currently dedicated to the development of atomisation processes equipment's at the Technological Centre EURECAT.

Ricardo Hernández is an Industrial Engineer, specializing in Mechanics and holds a master's degree in Business Management. He is currently a Ph.D. candidate at the Materials and Engineering Science Department of the Technical University of Catalonia. He is an expert in metallic materials forming process design. He is also responsible of different research projects at the Technical Centre EURECAT.

María Dolores Riera is a Professor from the Material Science and Metallurgical Engineering department at the Technical University of Catalonia. She specializes in plastic deformation process design and materials mechanical modelling and numerical simulation.

ORCID

Sasha Alejandra Cegarra Salges http://orcid.org/0000-0002-4675-9931
Jordi Pijuan http://orcid.org/0000-0002-9498-0673
Maria Dolores Riera http://orcid.org/0000-0001-9733-416X

References

[1] Singer ARE, Kisakurek SE. Centrifugal spray deposition aluminium strip. Met Technol. 1976;3:565–570.

[2] Frost AR. Rotary atomization in the ligament formation mode. J Agric Eng Res. 1981;26:63–78.

[3] Klaphaak DJ, Barnes LG. inventor; Atomization System Inc., assignee. Method of centrifugal atomization. United States Patent. 3,720,737. 1973 March 13.

[4] Yule AJ, Dunkley JJ. Atomization of melts. Oxford: Clarendon Press; 1994.

[5] Lavernia J, Srivatsan TS. The rapid solidification processing of materials: science principles, technology advances and applications. J Mater Sci. 2010;45:287–325.

[6] Yung-Zhong L, Minagawa K, Kakisawa H, et al. Melt film formation and disintegration during novel atomization process. Trans Nonferrous Met Soc China. 2007;17:1276–1281.

[7] Plookphol T, Wisutmethangoon S, Gonsrang S. Influence of process parameters on SAC305 lead-free solder powder produced by centrifugal atomization. Powder Technol. 2011;214:506–512.

[8] Malvern Panalytical Limited. Optimizing metal powders for additive manufacturing. Worcestershire: Technical documentation; 2018.

[9] Minagawa K, Kasisawa H, Osawa Y, et al. Production of fine spherical lead-free solder powders by hybrid atomisation. Sci Technol Adv Mater. 2005;6:325–329.

[10] Sungkhaphaitoon P, Wisutmethangoon S, Plookphol T. Influence of process parameters on zinc powder produced by centrifugal atomisation. Mater Res. 2017;20 (3):718–724.

[11] Xie JW, Zhao YY, Dunkley JJ. Effects of processing conditions on powder particle size and morphology in centrifugal atomization of tin. Powder Metall. 2004;47(2):168–172.

[12] Dantzig JA, Rappaz M. Solidification. Switzerland: EPFL Press; 2009.

[13] Zheng B, Yaojun L, Yizhang Z, et al. Gas atomization of amorphous aluminium powder: part II. experimental investigation. Metalld Mater Trans B. 2009;40:995–1004.

[14] Fuqian Z, Ming X, Jianliang L, et al. Study of rapidly solidified atomization technique and production of metal alloy powders. Mater Sci Eng: A. 2001;304-306:579–582.

[15] Zheng B, Yaojun L, Yizhang Z, et al. Gas atomization of amorphous aluminium powder: Part I. thermal behaviour calculations. Metall Mater Trans B. 2009;40:768–778.

[16] Östürk S, Arslan F, Östürk B. Effect of production parameters on cooling rates of AA2014 alloy powders produced by water cooled, rotating disc atomisation. Powder Metall. 2003;46(4):342–348.

PAPER II

Cooling Rate Modeling and Evaluation During Centrifugal Atomization Process

Article

Cooling Rate Modeling and Evaluation during Centrifugal Atomization Process

Sasha A. Cegarra [1,*] , Jordi Pijuan [1] and María D. Riera [2]

1 Eurecat, Centre Tecnològic de Catalunya, Unit of Metallic and Ceramic Materials, Plaça de la Ciència 2, 08243 Manresa, Spain; jordi.pijuan@eurecat.org
2 Department of Mining, Industrial and ICT Engineering, Universitat Politècnica de Catalunya, Av. de les Bases de Manresa, 61-73, 08242 Manresa, Spain; md.riera@upc.edu
* Correspondence: sasha.cegarra@eurecat.org; Tel.: +34-938777373

Abstract: Centrifugal atomization is a rapid solidification technique involving fast cooling rates to produce high-quality powders. The final microstructure of the atomized particles is closely linked with the thermal history and cooling rates experienced during the atomization process. However, there is insufficient research on the temperature evolution of metal particles produced by this technique, and most works evaluate the thermal history of the droplet through semi-empirical correlations that lie outside the conditions where they were derived. In this work, the cooling rate of centrifugally atomized Al-4%Cu was studied via mathematical modelling and experimental validation. A heat transfer model was implemented, and the value of the convective heat transfer coefficient was obtained from the Whitaker semi-empirical correlation considering three cases of study for the thermophysical properties of the gas. The validity of the Whitaker correlation was experimentally evaluated by means of cooling rates based on the Secondary Dendrite Arm Spacing (SDAS) technique. The Whitaker correlation with the Reynolds and Prandtl numbers evaluated at the ambient temperature and the gas conductivity evaluated at the film temperature gave the best agreement with the experimental results, with cooling rates in the order of 10^5 Ks^{-1} for <32.5 μm powders atomized in He atmosphere.

Keywords: centrifugal atomization; cooling rate; secondary dendrite arm spacing

1. Introduction

Centrifugal atomization is a rapid solidification technique that has been widely used for the production of metal powder for decades [1–3]. During this process, a molten metal stream falls onto a rotating disk, forming a liquid film on its surface. At the edge of the spinning disk, the centrifugal force exceeds the surface tension of the liquid, causing the melt to break up into droplets that solidify in flight in the form of powder. This technique finds wide application in metal powder production for several industrial processes, such as additive manufacturing [4,5], sintering processing [6–8], and thermal spray processes [9,10].

The centrifugal atomization technique offers many advantages, compared to more conventional gas and water atomization technologies, in terms of spherical shape, narrow particle size distribution, low satellite content, and high energy efficiency [11]. Although these characteristics are of greatest interest in many of the classic applications of metal powder, the need for new materials with a unique combination of properties is increasingly emerging to satisfy the powder metallurgy industry needs, which makes way to amplify the research spectrum in the use of this technology.

Some of these materials are rapidly solidified alloys, such as amorphous materials, which require strict control of the microstructure of the powder [12]. In the case of centrifugal atomization, the final microstructure of a powder is highly dependent on the thermal transport between a droplet in flight and a surrounding cooling gas once the droplet is ejected from the disk. During metal atomization, temperature differences of 1000 K or more

can be found between the molten droplet and the ambient gas. Therefore, the thermophysical properties of the gas vary considerably, and depending on the reference temperature, uneven results could be obtained. To address this limitation, several approaches have been used to account for the variation of gas properties that occur across the boundary layers in different processes, such as impulse atomization and gas atomization [13,14].

Most of the published works on the centrifugal atomization technique have been principally concerned with the design of a centrifugal atomizer, modes of liquid disintegration from a rotating disk, and the effect of process conditions on the particle size of the atomized powders [15–19], with the aim of contributing to the design and optimization of centrifugal atomizers in order to improve the stability of the process. However, although the thermal transport between a droplet and a surrounding gas has been extensively studied for processes such as gas atomization [20–24], plasma spray [25] and impulse atomization [13,26], very little information could be found in the literature for the centrifugal atomization process [27,28].

In the present work, a mathematical model has been carried out to describe the thermal behavior of Al-4%Cu centrifugally atomized particles that allows a better understanding of the heat transfer phenomena for this process. These calculations are based on the semi-empirical transfer laws [13,29], accounting for the temperature-dependent thermophysical properties of the gas evaluated at different conditions. The aim is to investigate the validity range of this semi-empirical correlation which predicts the cooling rate in molten metal centrifugal atomization. The results are compared with experimental cooling rate results obtained from Secondary Dendrite Arm Spacing (SDAS).

2. Mathematical Model

The heat transfer between a particle and the surrounding medium can be represented by Newton's cooling law, expressed by the following equation:

$$Q_c = A_s h_g (T_d - T_A) \tag{1}$$

where Q_c is the heat flow, A_s is the total surface area of a sphere particle, T_d is the temperature of the droplet, T_A is the ambient gas temperature inside the atomizer, and h_g is the total transfer coefficient. The application of this expression to a particular fluid–particle system has the obvious difficulty of knowing the value of h_g, a coefficient that incorporates the effect of convection, conduction, and radiation heat transfer mechanisms.

The high cooling rates experienced by a particle during the centrifugal atomization process [30], together with the high thermal conductivity of the metallic material, favors the homogeneous temperature distribution inside the droplet so that conduction is usually assumed negligible. This requires that the Biot number (Bi) be less than 0.1, where $Bi = hd/k_p$, h is the heat transfer coefficient to the gas, d is the diameter of the particle, and k_p is the thermal conductivity of the particle [31,32].

On the other hand, it has been shown that in low melting temperature metallic materials, the radiation heat transfer mechanism is negligible [33]. However, in this work, to account for precise results, the radiation contribution was taken into account. In this sense, the transfer of heat by radiation Q_r is expressed as follows:

$$Q_r = A_s S_t \varepsilon \left(T_d^4 - T_w^4 \right) \tag{2}$$

where S_t is the Stefan–Boltzmann constant, ε is the emissivity, and T_w is the wall temperature. A maximum value of emissivity ($\varepsilon = 1$) was considered for this work.

The variable hg from Equation (1) is a convective coefficient that can be quantified through the Nusselt number, Nu, which thermally characterizes the boundary layer between a particle of diameter d_p and a cooling gas by the following general semi-empirical equation [34]:

$$Nu = h_c \frac{d_p}{k_g} = a + cRe^m Pr^n \tag{3}$$

where h_c is the convective component of the heat transfer coefficient, and k_g is the thermal conductivity of the gas. The coefficients a and c, as well as the exponents m and n, are inherent to each system and must be determined experimentally.

The Reynolds numbers of the particle, Re, and Prandtl number of the gas, Pr, are given by the following equations:

$$Re = \frac{\rho_g(V_g - V_p)d_p}{\mu_g} \tag{4}$$

$$Pr = \frac{\mu_g C_{pg}}{k_g} \tag{5}$$

where ρ_g is the density of the cooling gas, V_p and V_g are the particle and gas velocity, respectively, μ_g is the dynamic viscosity, k_g is the thermal conductivity, and C_{pg} is the specific heat capacity of the gas.

Several approximations of the Nusselt number have been published [25,29,35–37], although the most frequently used in the field of metal atomization are the Ranz and Marshall [25] and the Whitaker [29] correlations, both defined for systems with a stationary particle interaction and a moving fluid.

The convective component of heat transfer coefficient h_c, described by the Ranz and Marshall correlation, is represented in the following equation:

$$Nu = h_c \frac{d_p}{k_g} = 2.0 + 0.6Re^{1/2}Pr^{1/3} \tag{6}$$

Ranz and Marshall proposed the following values, $a = 2$, $c = 0.6$, $m = 0.5$, and $n = 0.33$, and they are valid for Reynolds between 0 and 200 and for Prandtl numbers between 0.68 and 0.72, with the gas properties evaluated at the average ambient temperature.

The convective component of heat transfer coefficient h_c, described by the Whitaker correlation, is represented in the following equation:

$$Nu = h_c \frac{d_p}{k_g} = 2.0 + \left(0.4Re^{1/2} + 0.06Re^{2/3}\right)Pr^{0.4}\left(\frac{\mu_A}{\mu_s}\right)^{1/4} \tag{7}$$

where μ_A/μ_s is the relationship between the viscosity at the ambient temperature μ_A and at the surface of the droplet μ_s. This approximation is valid for Nusselt number values between 3.5×10^4 and 7.6×10^4, Reynolds number between 0.71 and 380, and Prandtl numbers between 1 and 3.2 [13].

Both approximations, Ranz and Marshall and Whitaker, share the same equation structure. The fundamental difference between both approaches is the inclusion of the viscosity ratio in Whitaker's correlation. In their test conditions, where a stationary copper sphere was exposed to a stream of water, they found that water exhibited a significant change in viscosity with temperature. In addition, Whitaker's correlation separates the term relative to the Reynolds number into two contributions corresponding to the two types of regimes that are established in the laminar and wake regions found in the particle and fluid interaction.

A limitation of the former correlations, highlighted by numerous published works [14,21,31,38], is the validity of their extrapolation to systems that incorporate high temperatures, such as metal atomization techniques. In this sense, the work of Wiskel et al. [13] deserves to be highlighted. They proposed a modification of Whitaker's correlation applicable to the impulse atomization conditions for the production of Al-4.5%Cu powder, considering the temperature variation of the thermophysical properties of the gas through the boundary layer in high-temperature systems, expressed by the following relationship:

$$Nu = \frac{2B}{K_s(m+1)} \frac{T_s^{m+1} - T_A^{m+1}}{T_s - T_A} + \left(0.4T_s^{\frac{1}{2}} + 0.06Re_s^{\frac{2}{3}}\right)Pr_s\left(\frac{\mu_A}{\mu_s}\right)^{\frac{1}{4}} \tag{8}$$

where B is the pre-power coefficient from the variation of gas conductivity with temperature and is equal to 3.44×10^{-4}.

Overall, the evaluation of the thermophysical properties of the gas varies from author to author and must be addressed for each specific system through adjustments with experimental results. During centrifugal atomization, the initial droplet speed when the particles are ejected from the disk, and their trajectory during flight are the key parameters in the heat transfer mechanism. Zhao et al. studied the flow development and the velocity of the droplet depending on the melt flow rate in different conditions of atomization, in the case of a full spreading melt and the case of discontinuous melt flow rate on the atomization disc [39,40].

Zhao et al. [39] showed that for rotating disk velocities between 3000 to 60,000 rpm, specifically from the centrifugal atomization process studied in this work, the tangential component velocity of the atomizing disk is far superior to the radial component. Therefore, the tangential velocity of the atomizing disk can be used as an accurate estimate of the initial metal droplet velocity, to be 94.2 ms^{-1} at a rotating speed of 40,000 rpm.

After leaving the disk, the trajectory of the particles depends on the forces acting during their flight in the atomization chamber: buoyancy, gravity, and drag forces. Under the conditions of centrifugal atomization, the buoyancy effect is negligible, and it is not considered in this study [32].

After the particle is released from the disc, its movement is described into a plane tangent to the disc. In the vertical direction, gravity force is present, while the components of drag force appear in the horizontal and vertical directions. The drag coefficient is computed according to Yule et al. which considers a drag coefficient for particles in the micron range.

$$C_d = 18.5/Re^{0.6} \tag{9}$$

The acceleration components of the droplet are expressed as:

$$d^2x/dt^2 = -\rho_g(dx/dt)^2 A_s C_d/2m_d \tag{10}$$

$$d^2y/dt^2 = g - \rho_g(dy/dt)^2 A_s C_d/2m_d \tag{11}$$

where A_s and m_d is the area of the mass of the droplet, respectively.

The density and viscosity of the gas in which the particle moves and cools, as well as its size and speed with respect to that of the gas, determine the drag force to which it is subjected and the type of fluid dynamic regime that develops. In addition, in its flight inside the atomizer chamber, the particle, initially driven by the centrifugal force imposed by the rotating disk, loses speed until it collides with the wall of the chamber or drops to its bottom. The progressive change in temperature and, therefore, in the thermal gradient between the particle and the gas, as well as the decrease in the speed, continuously modify the heat transfer conditions. Hence, it is important to address the dependent thermophysical properties of the gas to accurately calculate the heat transfer and cooling rate in the process of droplet solidification during centrifugal atomization.

In this work, the Whitaker correlation [29] and the Whitaker modified correlation [13], which considers the effect of gas viscosity, were used to determine the Nu number. The thermal gas conductivity k_g in Equations (6) and (7) was evaluated at three different temperatures: Case 1, at gas ambient temperature T_A; Case 2, at film temperature T_f, which is the median temperature between the droplet and ambient gas temperatures, $T_f = (T_d + T_A)/2$; and Case 3, at droplet surface temperature T_d.

2.1. Cooling Rate Calculation

The size of the solidification microstructure is related to the solidification cooling over the entire local solidification process [11]. Therefore, the cooling rate is computed as the

difference between liquidus and solidus temperature with respect to the local solidification time:

$$CR = (T_l - T_s)/t_{ls} \qquad (12)$$

where T_l and T_s are the liquidus and solidus temperature, and t_{ls} is the time required for each full solidification state.

During the solidification period, an equivalent heat capacity coefficient is computed to consider solidification enthalpy [41].

$$C_{p,app} = \Delta H_m/(T_l - T_s) + C_{p,s} + C_{p,l}/2 \qquad (13)$$

where ΔH_m is the latent heat of fusion, $C_{p,l}$ is the specific heat capacity of the material in a liquid state, while $C_{p,s}$ is the specific heat capacity of the material in a solid state, and T_l and T_s are the liquidus and solidus temperatures.

2.2. Properties of Atomization Gas and Alloys

Trajectories and thermal history of particles of different sizes (32.5, 60, 90.5, 115.5, 137.5 and 165 µm) were computed to correspond with the median particle size on each particle size range analyzed in this work. Two gas atmospheres (He and Ar at 25 °C and 1 atm) and two initial melt superheat temperatures (250 K and 400 K) were considered. The initial velocity of droplets was computed according to the tangential velocity in an atomization disc of 45 mm diameter spinning at 40,000 rpm. Values of thermophysical properties of Al-4%Cu alloy are shown in Table 1 [42].

Table 1. Physical and thermal properties of alloy Al-4%Cu.

Parameter	Symbol (Unit)	Value
Liquidus Temperature	T_l (K)	921
Solidus Temperature	T_s (K)	845
Density of the droplet	ρ_d (kg m^{-3})	2540
Specific Heat of Liquid Alloy	$C_{p,l}$ (J kg^{-1} K^{-1})	910
Specific Heat of Solid Alloy	$C_{p,s}$ (J kg^{-1} K^{-1})	1178
Latent Heat of Fusion	ΔH_f (J kg^{-1})	381,774

An exponential equation is used to define He and Ar thermal conductivity, dynamic viscosity, and density depending on temperature [21]. Gas-specific heat capacity is assumed to be constant. The thermophysical properties of gases are shown in Table 2 [21].

Table 2. Thermophysical properties of He and Ar.

Parameter	Ar	He
Density ρ_g (kg/m^3)	$486.61/T$	$48.774/T$
Dynamic Viscosity μ_g (Pa·s)	$3.7763 \cdot 10^{-7} \cdot T^{0.71832}$	$4.3679 \cdot 10^{-7} \cdot T^{0.67016}$
Thermal Conductivity k_g (W m^{-1}K^{-1})	$2.5943 \cdot 10^{-4} \cdot T^{0.74021}$	$2.1588 \cdot 10^{-3} \cdot T^{0.74210}$
Specific Heat Capacity C_{pg} (J kg^{-1} K^{-1})	520.8	5197

3. Materials and Methods

3.1. Materials

Commercial aluminum alloy Al 1050 and electrolytic copper with a purity of 99.9% were induction melted in a mass composition of Al-4%Cu prior to atomization. This alloy was used since many studies on the correlation between Secondary Dendrite Arm Spacing of Al-4%Cu alloys and cooling rate are found in the literature [43–46].

3.2. Atomization

A schematic diagram of the centrifugal atomizer pilot plant is shown in Figure 1. The stainless steel atomization chamber measures 2.5 m in diameter and 4 m in height. The

melting system consists of a crucible, an alumina stopper rod, and a thermocouple as a temperature controller. The crucible with a 3.5 mm hole was made of alumina, and the metal was heated via induction. A stopper rod was fitted to the hole to control the molten metal exit. A 45 mm H13 steel spinning disk with a ZrO_2 coating was used for atomizing the molten metal. A water-cooling system for the disk was used to guarantee the integrity of the disk due to the high temperatures of atomization. The atmosphere controlling unit consists of a vacuum pump with levels down to 1 Pa and an inert gas supply.
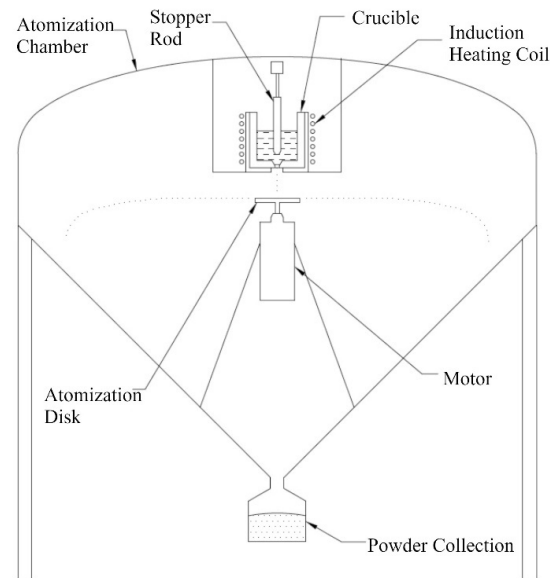
Figure 1. Schematic diagram of the centrifugal atomization pilot plant.

Prior to melting and atomization, the vacuum pump was run to ensure low oxygen content, being backfilled with up to 1 atm of He or Ar according to the atomization. The raw materials were induction melted to temperatures of 850 K and 1050 K, which corresponds to a superheating temperature of 250 K and 400 K, respectively. To ensure maximum homogenization of all elements, the molten metal atomization temperature was kept constant for 10 min. Molten metal was poured gravity onto the atomization disc rotating at 40,000 rpm. Figure 2 shows observations on the melt performance on the rotating disk during atomization made with a Vision Research Phantom v311 Monochrome high-speed camera.
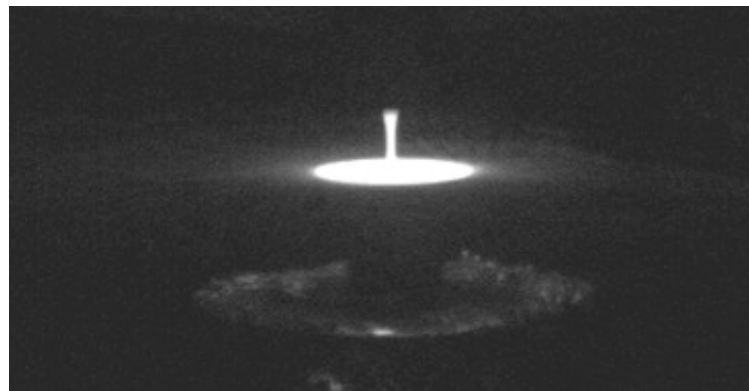
Figure 2. Centrifugal atomization process in operation.

A series of atomization runs were carried out with the variation of the inert gas atmosphere and the alloy melt superheat temperature as the main parameters of the atomization process. The experimental process parameters of atomization are shown in

Table 3. A total of 350 g of materials were melted and atomized for each experiment, where only one parameter was changed, leaving the others fixed. The mass median particle size and the log-normal standard deviation (σ) were calculated.

Table 3. Experimental processing parameters of atomization.

Run #	Gas Type	Superheat Melt Temperature	D_{50} (µm)	σ
1	100% Ar	400	113	1.82
2	100% He	400	119	1.63
3	100% Ar	250	107	1.64
4	100% He	250	104	1.69

3.3. Powder Characterization

Following atomization, each of the as-produced powders was collected and sieved according to ASTM-B214-07 for 15 min with a Filtra FTL-0150 electromagnetic digital sieving machine into six fractions: 25–45 µm, 75–45 µm, 106–75 µm, 125–106 µm, 150–125 µm, and 180–150 µm. Samples of each size fraction from each experiment were subsequently metallographically prepared. A total of 25 samples were cold mounted using epoxy resin, mixing the metal powder with a small amount of epoxy resin and pouring it into the bottom of the specimen cup. Samples were ground using wet grit SiC paper of 600-800-1200-2400-4000, respectively, for one minute at a force of 20 N. The specimens were polished with diamond suspension solution of 6 µm, 3 µm, and 1 µm for 10 min in each step, applying a force of 20 N, and finally finishing with colloidal dispersions of silica (SiO_2) for 10 min. The procedures were applied according to ASTM-B215, using standard metallographic methods for uncompacted metal powders [47]. The shape, microstructure and SDAS of the powders were investigated by using an Ultra Plus Field Emission Scanning Electron Microscope (SEM).

3.4. Secondary Dendrite Arm Spacing Measuring Method

SEM images were used to measure SDAS with the image analysis software Olympus Stream Version 2.4.4, with enabled direct length readings. A minimum of 10 particles were analyzed for each size range, and at least 10 dendrites were measured in each particle. The secondary dendrites were evaluated according to the following equation:

$$SDAS = 2/N_{arms} - 1 \tag{14}$$

where *N* represents the number of secondary arms counted along one side of the primary arm, and *L* is measured as the length parallel to the primary arm between the first and the last secondary dendrite arm, as shown in Figure 3.
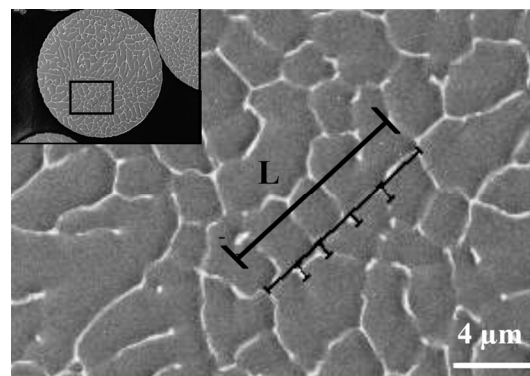

Figure 3. Schematic representation of SDAS measurement.

4. Results and Discussion

4.1. Metallographic Analysis

SEM micrographs from Figure 4 show the solidification structure for Al-4%Cu droplets in the 75–45 μm size range observed in each experiment. The microstructure of the atomized Al-4%Cu powders consisted of a fine equiaxed dendrite structure which is typical for all-size droplets atomized in this study. From these micrographs, no visible changes are shown in the effect of melting superheat temperature on the resulting microstructure. However, the gas composition does have a significant effect on the microstructure, resulting in fine-scale microstructure for powders atomized in He, as opposed to those atomized in Ar.
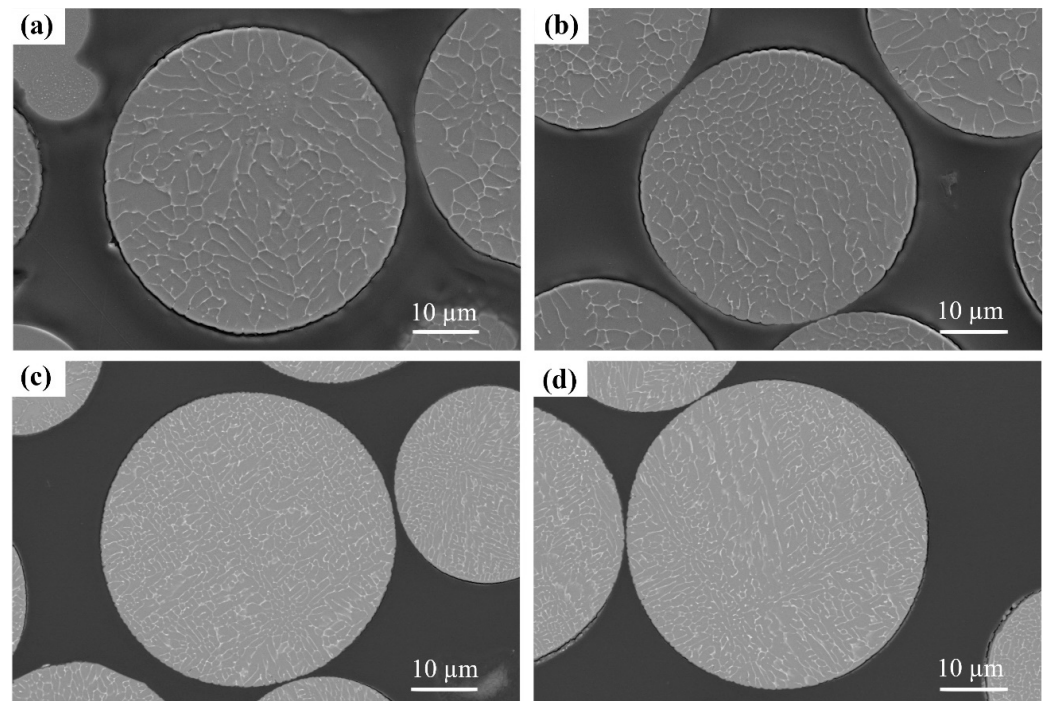
Figure 4. Micrographs of Al-4%Cu centrifugal atomized particles (size fraction from 45 to 75 μm) at different gas compositions and melt superheat temperatures: (**a**) Ar-400 K; (**b**) Ar-250 K; (**c**) He-400 K; and (**d**) He-250 K.

4.2. Secondary Dendrite Arm Spacing—Cooling Rate Correlation

The relationship between secondary arm spacing λ and cooling rate R is obtained by means of a correlation analysis leading to the following empirical logarithmic equation [48,49]:

$$\lambda = \lambda_0 R^{-n} \tag{15}$$

where R is the cooling rate and n and λ_0 are constants derived empirically where the SDAS is compared to the cooling rate. In this work, Mullis' correlation [45], based on several published experiments for Al-Cu alloy, was used to convert the SDAS results to cooling rate as a function of the mean particle size.

$$\lambda = 58.7 R^{-0.355} \tag{16}$$

The relationship between SDAS with respect to the corresponding fraction size for each atomization run is plotted in Figure 5a, whilst a direct comparison of the SDAS to cooling rate as a function of the mean particle size is shown in Figure 5b [46].
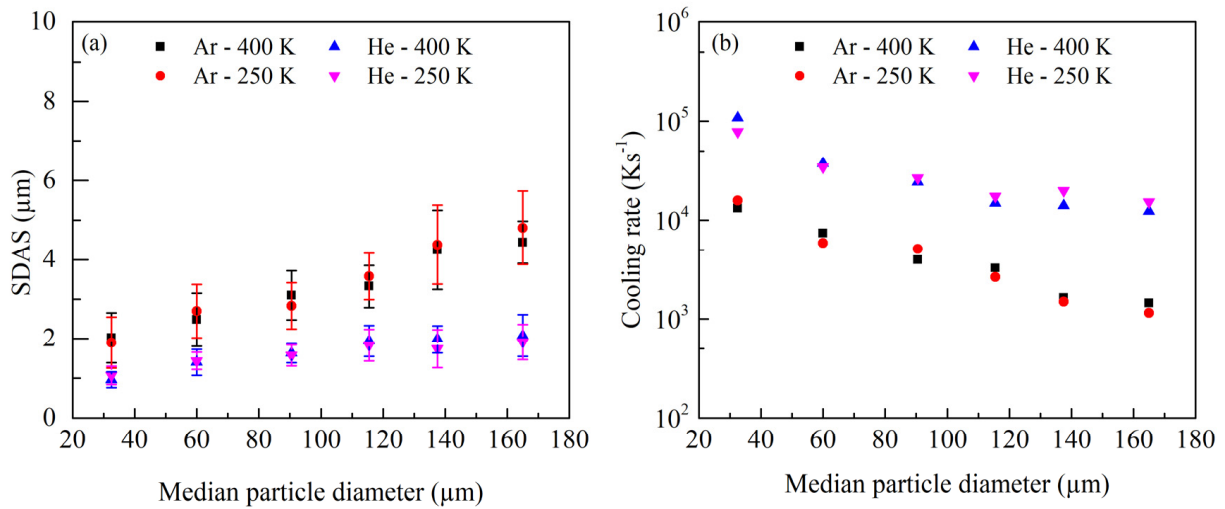
Figure 5. (**a**) Experimental results of the SDAS as a function of the mean particle size for a corresponding size range; (**b**) calculated cooling rate as a function of the mean particle size for a corresponding size range.

Error bars in Figure 5a represent the standard deviation calculated from the data of corresponding fraction size. This standard variation is caused by the cumulative effect of measurement errors inherent to the SDAS measurement method, the thermal history of each particle resulting in different microstructures, and the range of particle sizes experiencing different cooling rates.

The results capture a refinement in dendritic structure with decreasing particle size. The length of SDAS ranges from 2 to 5 μm for particles atomized in the Ar atmosphere. However, for particles atomized in the He atmosphere, the length of SDAS ranges from 1 to 2 μm. As expected, SDAS, for a given particle size, is finer for atomization in He relative to Ar due to the high thermal conductivity of He, whereas the melt superheat temperature does not seem to affect the microstructure. Based on these values, cooling rates range from 10^3 to 10^4 Ks^{-1} for particles atomized in the Ar atmosphere to 10^4 to 10^5 Ks^{-1} for particles atomized in the He atmosphere. These values are in agreement with those previously reported by Östürk [27], although the processing parameters in their study differ from this work.

4.3. Theoretical Cooling Rate

Figure 6 shows the theoretically cooling rate as a function of mean particle diameter for the three cases of study considered in this work for the evaluation of the Nusselt number Nu:

- Case 1: Whitaker correlation with k_g, Re and Pr evaluated at the ambient temperature T_A;
- Case 2: Whitaker correlation with k_g evaluated at the film temperature $T_f = (T_d + T_A)/2$ and Re and Pr evaluated at the ambient temperature T_A;
- Case 3, Wiskel modified correlation with k_g evaluated at the droplet surface temperature T_d and Re and Pr evaluated at the ambient temperature T_A.

The cooling rate notably changes with the different conditions studied in this work. Both the thermophysical properties of the He and the Ar atmosphere vary considerably from the droplet surface temperature T_d to the ambient temperature T_A, confirming that these differences can have a significant impact on the centrifugal atomization heat transfer evaluation.
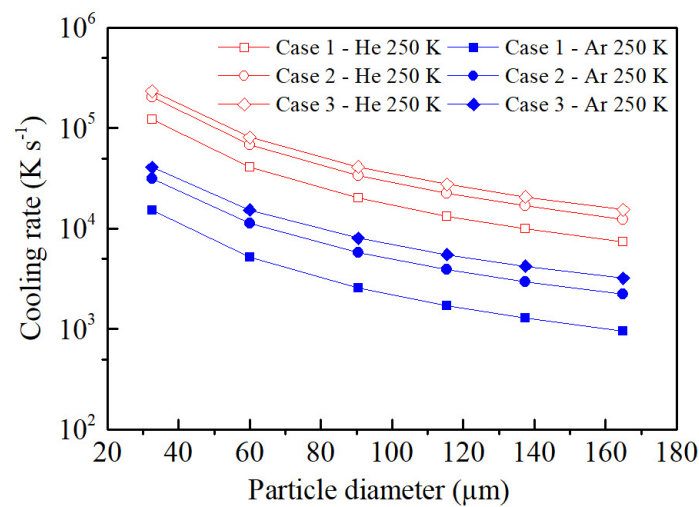
Figure 6. Theoretically calculated cooling rate as a function of the mean particle diameter for particles atomized in Ar and He atmospheres at 250 K superheat temperature. Gas properties were evaluated at three different temperatures: case 1, at gas ambient temperature T_A; case 2, at film temperature T_f; case 3, at droplet surface temperature T_d.

The curves for Case 1 have the lowest values of cooling rate, between 2.7×10^3 Ks^{-1} and 3×10^4 Ks^{-1} for particles atomized in the Ar atmosphere and between 1.7×10^4 Ks^{-1} and 2×10^5 Ks^{-1} for particles atomized in the He atmosphere. The thermal conductivity k_g evaluated at the ambient temperature T_A corresponds to systems where the temperature differences between the particle and the fluid are small. Therefore, the thermophysical properties of the gas in the boundary layer do not vary significantly. Despite this and the great temperatures differences found in metallurgical processes such as centrifugal atomization, the evaluation of these properties continues to be evaluated at the ambient temperature for a large number of processes [20,50,51], which may introduce errors in the final cooling rate results.

Regarding Case 2, although it has been suggested to use the Whitaker correlation with the evaluation of k_g at the ambient temperature [24], using these values at the film temperature T_f is, a priori, a reasonable approximation for systems where the temperature differences in the boundary layer may become larger than in Case 1. Figure 4 shows an increase in the cooling rate values in Case 2 compared to Case 1.

Finally, Case 3 corresponds to the case where the thermal conductivity k_g is measured at the droplet surface temperature T_d, that is, when the relative velocity between the atomized particle and the gas approaches zero. In this approach, the Wiskel correlation [13] was used to account for the temperature dependency of k_g in the boundary layer for systems where the temperature differences between the particle and the fluid are big (approx. 1000 K). Case 3 gives the highest values of cooling rate from the three cases of study.

As expected, as the temperature where the thermal conductivity k_g is measured increases, the cooling rate values also increase. It is evident that the cooling rate notably changes with the different conditions, following the same pattern either for particles atomized in Ar or He gas, stating the importance of determining at which temperature (ambient, film of surface temperature) to calculate the thermophysical properties of the gas.

4.4. Experimental Validation of the Model

Figure 7 shows the cooling rate calculated theoretically for the three cases of study, as well as the cooling rate calculated experimentally and through Mullis' empirical correlation for Al-4%Cu [45].
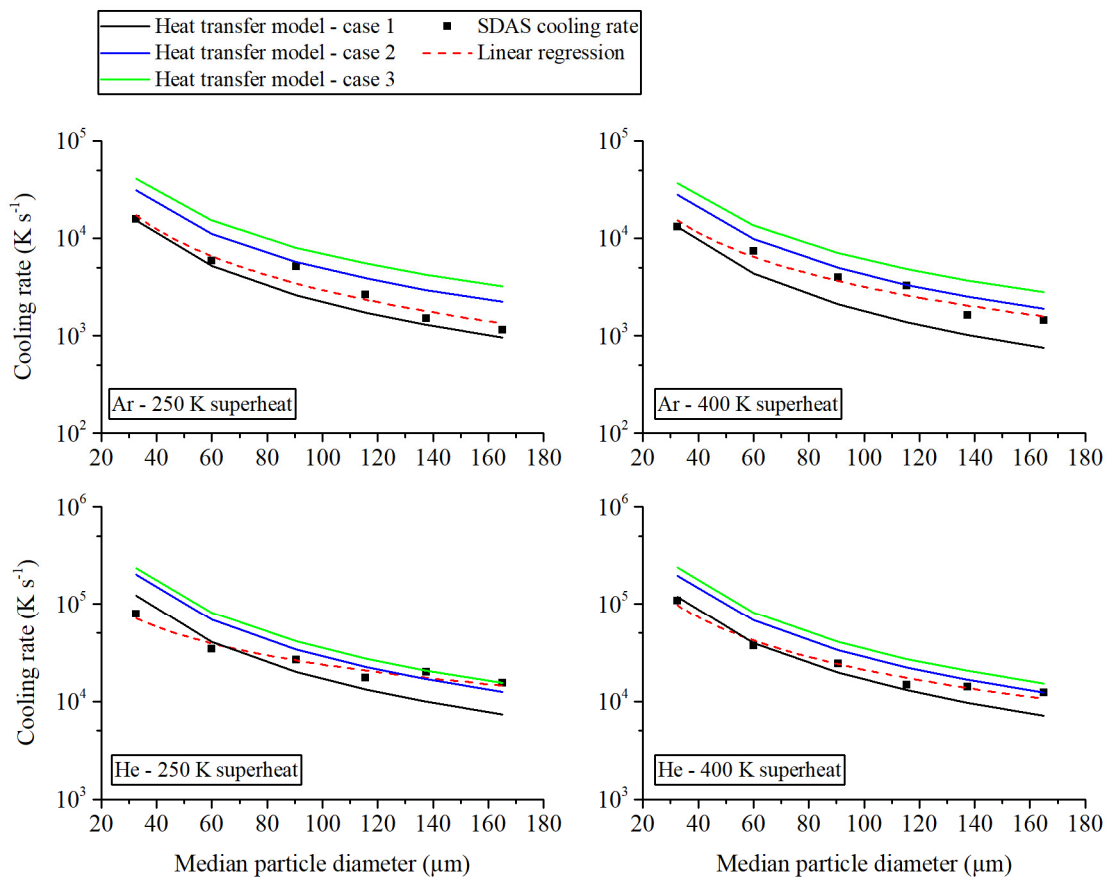
Figure 7. Comparison between the theoretically calculated cooling rate for the three cases of study and the calculated cooling rates based on SDAS measurements.

It becomes evident that in Case 3, where k_g is evaluated at the surface temperature of the droplet T_d, the model yields overestimated cooling rate values. It is worth mentioning that Wiskel reported that the gas properties evaluated at T_d fit better for the impulse atomization process [7]. This may be due to the low particle velocity achieved during impulse atomization. When the relative velocity between the gas and the particle approaches zero, it seems of a good agreement to evaluate the gas properties at the droplet surface temperature T_d. However, during the centrifugal atomization process, particles experience a high velocity provided by the disk speed. Thus, the surrounding gas renovation around the particle is faster than during impulse atomization; therefore, evaluating k_g at the surface temperature of the droplet does not correlate with the experimental results.

From the comparison between the theoretical cooling rate and the experimental cooling rate calculation, it is not clear whether the evaluation of k_g using the Whitaker correlation at the film temperature T_f gives better results than evaluating k_g at the ambient temperature T_A. For small particle sizes, evaluating the properties of the gas at the ambient temperature correlates better by comparing both results, theoretical and experimental approaches, while as the particle size increases, Case 2 gives better results. However, it is known that to calculate the convective heat transfer coefficient h_c, the use of k_g at ambient temperatures may introduce errors for higher temperatures systems. In this sense, the evaluation of the thermophysical properties of the gas for the centrifugal atomization process is recommended to be addressed using Whitaker's correlation, which considers the temperature differences through the ratio of the dynamic viscosities at the droplet surface temperature T_d and the ambient temperature T_A, with the evaluation of the thermal conductivity of the gas k_g from the Nusselt number at the film temperature T_f.

From the heat transfer model, it is evident that the cooling rate of particles depends largely on the alloy in terms of density, specific heat, and melting temperature. In addition,

in the case of the centrifugal atomization process, in particular, the cooling rate also depends on the size of the particle in trajectory, the initial velocity of the particle, and the properties of the gas. In this sense, by varying the properties of the gas for a specific alloy, and for a known initial velocity provided by the disk speed, the heat transfer process gives different results for the cooling rate of the particles.

The proposed approach does not consider the effect of radiation, which in cases of high melt temperature alloys, its contribution is significant. Additionally, for simplicity, the model considers just one particle solidifying at a time with no interaction with each other, which otherwise would contribute to a local temperature increase resulting in a lower cooling rate. Finally, the use of a Mullis semi-empirical relationship is applicable to Al-4%Cu alloys. Although these limitations arise, this work suggests further advances in terms of modelling the solidification process in the centrifugal atomization process.

4.5. Thermal Evolution of the Atomized Particles

Figure 8 shows the temperature profile for a 60 μm and 137 μm droplet atomized in the Ar and He atmosphere, with a melt superheat temperature of 250 K computed using Case 2 in the mathematical model. It can be seen that the temperature decreases rapidly with changing the gas composition from Ar to He. For a 60 μm particle atomized in an Ar atmosphere, it takes 8.7×10^{-3} s to completely solidify, whereas, for the same particle size atomized in a He atmosphere, it takes 1.6×10^{-3} s to solidify. Therefore, for the same particle size, solidification occurs earlier in a He atmosphere, meaning that the solidification of droplets occurs in a nearer position of the atomization disc than in an Ar atmosphere.
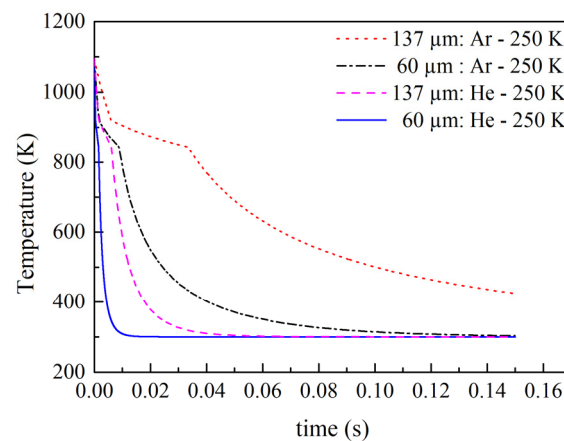
Figure 8. The temperature profile of centrifugally atomized particles for Case 2 of this study, for particles atomized in Ar and He atmospheres at 250 K superheat temperature.

Moreover, Figure 8 shows that droplet temperature decreases faster with decreasing powder size from 137 to 60 μm within the same gas composition. For example, particles of 60 μm atomized in He atmosphere take 3.7×10^{-4} s, while particles of 137 μm atomized in the same atmosphere take 6.07×10^{-3} s to completely solidify, increasing one order of magnitude. These results confirm that while the gas composition is effective in influencing the cooling rate of the atomized particles, the cooling rate has a strong dependence on droplet size.

5. Conclusions

A mathematical model was employed to describe the thermal behavior of Al-4%Cu centrifugally atomized particles coupled with the characterization of the powder by the Secondary Dendrite Arm Spacing method. This contribution discusses the effect of the temperature-dependent thermophysical properties of the gas evaluated at different conditions.

To calculate cooling rates to be consistent with those determined experimentally by the semi-empirical model proposed by Mullis correlation, the gas thermal conductivity k_g requires the evaluation of the thermal conductivity of the gas at the film temperature T_f, which accounts for the fast-surrounding gas renovation when the particle is expelled from the disk.

From the SDAS measurements, the cooling rate was calculated to be from 10^4 to 10^5 Ks^{-1} for particles atomized in a He atmosphere and from 10^3 to 10^4 Ks^{-1} for particles atomized in an Ar atmosphere, where He provides the highest rates of heat transfer compared to Ar due to its higher thermal conductivity.

The realization of the full potential of centrifugal atomization is limited by the lack of in-depth scientific understanding of the process. Therefore, and since the process of droplet solidification during flight is not available experimentally, this study offers new insights into the scientific knowledge in this field in order to improve the process in terms of the predictability of the resulting powder atomized by the centrifugal atomization process.

References

1. Frost, A. Rotary Atomization in the Ligament Formation Mode. *J. Agric. Eng. Res.* **1981**, *26*, 63–78. [CrossRef]
2. Klaphaak, D. Method of Centrifugal Atomization. U.S. Patent 3,720,737, 13 March 1973.
3. Mandal, S.; Sadeghianjahromi, A.; Wang, C.C. Experimental and Numerical Investigations on Molten Metal Atomization Techniques—A Critical Review. *Adv. Powder Technol.* **2022**, *33*, 103809. [CrossRef]
4. Popov, V.V.; Grilli, M.L.; Koptyug, A.; Jaworska, L.; Katz-demyanetz, A.; Klobčar, D.; Balos, S.; Postolnyi, B.O.; Goel, S. Powder Bed Fusion Additive Manufacturing Using Critical Raw Materials: A Review. *Materials* **2021**, *14*, 909. [CrossRef]
5. Sames, W.J.; List, F.A.; Pannala, S.; Dehoff, R.R.; Babu, S.S. The Metallurgy and Processing Science of Metal. *Int. Mater. Rev.* **2016**, *61*, 315–360. [CrossRef]
6. Narasimhan, K.S.; Semel, F.J. Sintering of Powder Mixtures and the Growth of Ferrous Powder Metallurgy. *Mater. Chem. Phys.* **2001**, *67*, 56–65. [CrossRef]
7. Deirmina, F.; Pellizzari, M.; Federici, M. Production of a Powder Metallurgical Hot Work Tool Steel with Harmonic Structure by Mechanical Milling and Spark Plasma Sintering. *Metall. Mater. Trans. A* **2017**, *48*, 1910–1920. [CrossRef]
8. Kim, J.H.; Lee, J.W.; Kim, K.H.; Lee, C.B. Preliminary Study on the Fabrication of Particulate Fuel through Pressureless Sintering Process. *Sci. Technol. Nucl. Install.* **2016**, *2016*, 3717361. [CrossRef]
9. Henao, J.; Concustell, A.; Cano, I.G.; Dosta, S.; Cinca, N.; Guilemany, J.M.; Suhonen, T. Novel Al-Based Metallic Glass Coatings by Cold Gas Spray. *Mater. Des.* **2016**, *94*, 253–261. [CrossRef]
10. Bauckhage, K. Fundamentals of Melt Atomization, Spray Forming and Deposition. In Proceedings of the International Conference on Liquid Atomization and Spray Systems ICLASS, Sorrento, Italy, 13–17 July 2003.
11. Bogno, A.-A.; Henein, H.; Uhlenwinkel, V.; Gärtner, E. Single Fluid Atomization Fundamentals. In *Metal Sprays and Spray Deposition*; Henein, H., Uhlenwinkel, V., Fritsching, U., Eds.; Springer: Cham, Switzerland, 2017; pp. 9–46, ISBN 978-3-319-52687-4.
12. Pijuan, J.; Cegarra, S.A.; Dosta, S.; Albaladejo-Fuentes, V.; Riera, M.D. Centrifugal Atomization of Glass-Forming Alloy Al$_{86}$Ni$_8$Y$_{4.5}$La$_{1.5}$. *Materials* **2022**, *15*, 8159. [CrossRef]
13. Wiskel, J.B.; Henein, H.; Maire, E. Solidification Study of Aluminum Alloys Using Impulse Atomization: Part I: Heat Transfer Analysis of an Atomized Droplet. *Can. Metall. Q.* **2002**, *41*, 97–110. [CrossRef]
14. Poulikakos, D.; Waldvogel, J.M. Heat Transfer and Fluid Dynamics in the Process of Spray Deposition. *Adv. Heat Transf.* **1996**, *28*, 1–74. [CrossRef]
15. Zhang, L.P.; Zhao, Y.Y. Particle Size Distribution of Tin Powder Produced by Centrifugal Atomisation Using Rotating Cups. *Powder Technol.* **2017**, *318*, 62–67. [CrossRef]

16. Sungkhaphaitoon, P.; Plookphol, T.; Wisutmethangoon, S. Design and Development of a Centrifugal Atomizer for Producing Zinc Metal Powder. *Int. J. Appl. Phys. Math.* **2012**, *2*, 77–82. [CrossRef]

17. Sungkhaphaitoon, P.; Wisutmethangoon, S.; Plookphol, T. Influence of Process Parameters on Zinc Powder Produced by Centrifugal Atomisation. *Mater. Res.* **2017**, *20*, 718–724. [CrossRef]

18. Zhao, Y.Y.; Jacobs, M.H.; Dowson, A.L. Liquid Flow on a Rotating Disk Prior to Centrifugal Atomization and Spray Deposition. *Metall. Mater. Trans. B* **1998**, *29*, 1357–1369. [CrossRef]

19. Kumar, P.; Sarkar, S. Experimental Investigation of Liquid Disintegration on Slotted Disc in Centrifugal Atomization Process. *Chem. Eng. Res. Des.* **2019**, *145*, 76–84. [CrossRef]

20. Freyberg, A.V.; Henein, H.; Uhlenwinkel, V.; Buchholz, M. Droplet Solidification and Gas-Droplet Thermal Coupling in the Atomization of a Cu-6Sn Alloy. *Metall. Mater. Trans. B* **2003**, *34*, 243–253. [CrossRef]

21. Ciftci, N.; Ellendt, N.; Coulthard, G.; Soares Barreto, E.; Mädler, L.; Uhlenwinkel, V. Novel Cooling Rate Correlations in Molten Metal Gas Atomization. *Metall. Mater. Trans. B* **2019**, *50*, 666–677. [CrossRef]

22. Zheng, B.; Lin, Y.; Zhou, Y.; Lavernia, E.J. Gas Atomization of Amorphous Aluminum: Part I. Thermal Behavior Calculations. *Metall. Mater. Trans. B* **2009**, *40*, 768–778. [CrossRef]

23. He, S.; Liu, Y.; Guo, S. Cooling Rate Calculation of Non-Equilibrium Aluminum Alloy Powders Prepared by Gas Atomization. *Rare Met. Mater. Eng.* **2009**, *38*, 353–356.

24. Ellendt, N.; Lumanglas, A.M.; Moqadam, S.I.; Mädler, L. A Model for the Drag and Heat Transfer of Spheres in the Laminar Regime at High Temperature Differences. *Int. J. Therm. Sci.* **2018**, *133*, 98–105. [CrossRef]

25. Abderrahmane, A.; Mohamed, A.; Abdelkader, N.; El Ganaoui, M.; Pateyron, B. Ranz and Marshall Correlations Limits on Heat Flow Between a Sphere and Its Surrounding Gas at High Temperature. *Therm. Sci.* **2015**, *19*, 1521–1528. [CrossRef]

26. Ellendt, N.; Schmidt, R.; Knabe, J.; Henein, H.; Uhlenwinkel, V. Spray Deposition Using Impulse Atomization Technique. *Mater. Sci. Eng. A* **2004**, *383*, 107–113. [CrossRef]

27. Öztürk, S.; Arslan, F.; Öztürk, B. Effect of Production Parameters on Cooling Rates of AA2014 Alloy Powders Produced by Water Jet Cooled, Rotating Disc Atomisation. *Powder Metall.* **2003**, *46*, 342–348. [CrossRef]

28. Zhu, X.; Ding, B.; Wang, H.; He, X.Y.; Tan, Y.; Liao, Q. Numerical Study on Solidification Behaviors of a Molten Slag Droplet in the Centrifugal Granulation and Heat Recovery System. *Appl. Therm. Eng.* **2018**, *130*, 1033–1043. [CrossRef]

29. Whitaker, S. Forced Convection Heat Transfer Correlations for Flow in Pipes, Past Flat Plates, Single Cylinders, Single Spheres, and for Flow in Packed Beds and Tube Bundles. *AIChE J.* **1972**, *18*, 361–371. [CrossRef]

30. Cegarra Salges, S.A.; Pijuan, J.; Hernández, R.; Riera, M.D. Effect of Processing Parameters on Copper Powder Produced by Novel Hybrid Atomisation Technique. *Powder Metall.* **2020**, *63*, 142–148. [CrossRef]

31. Meharabian, R.; Hsu, S.C.; Levi, C.G.; Kou, S. Heat Flow Limitations in Rapid Solidification Processing. In *Advances in Metal Processing*; Burke, J.J., Meharabian, R., Weiss, V., Eds.; Plenum Press: New York, NY, USA, 1981; pp. 13–44, ISBN 9781461583028.

32. Yule, A.J.; Dunkley, J.J. *Atomization of Melts*, 1st ed.; Oxford University Press: Oxford, UK, 1994; ISBN 0198562586.

33. Gianoglio, D.; Ciftci, N.; Armstrong, S.; Uhlenwinkel, V.; Battezzati, L. On the Cooling Rate-Microstructure Relationship in Molten Metal Gas Atomization. *Metall. Mater. Trans. A* **2021**, *52*, 3750–3758. [CrossRef]

34. Ranz, W.E.; Marshal, W.R. Evaporation from drops. *Chem. Eng. Prog.* **1952**, *48*, 141–146.

35. Lewis, J.A.; Gauvin, W.H. Motion of Particles Entrained in a Plasma Jet. *AIChE J.* **1973**, *19*, 982–990. [CrossRef]

36. Young, R.M.; Pfender, E. Nusselt Number Correlations for Heat Transfer to Small Spheres in Thermal Plasma Flows. *Plasma Chem. Plasma Process.* **1987**, *7*, 211–229. [CrossRef]

37. Haghighatjoo, M. A Numerical Investigation of Free-Fall Swirling Gas Atomization Process. Masters's Thesis, Concordia University, Montreal, QC, Canada, November 2020.

38. Lee, E.S.; Ahn, S. Solidification Progress and Heat Transfer Analysis of Gas-Atomized Alloy Droplets during Spray Forming. *Acta Metall. Mater.* **1994**, *42*, 3231–3243. [CrossRef]

39. Zhao, Y.Y. Analysis of Flow Development in Centrifugal Atomization: Part I. Film Thickness of a Fully Spreading Melt. *Model. Simul. Mater. Sci. Eng.* **2004**, *12*, 959–971. [CrossRef]

40. Zhao, Y.Y. Analysis of Flow Development in Centrifugal Atomization: Part II. Disintegration of a Non-Fully Spreading Melt. *Model. Simul. Mater. Sci. Eng.* **2004**, *12*, 973–983. [CrossRef]

41. Produktionstechnik, D.F.; Ciftci, N. Cooling Strategies for the Atomization of Glass-Forming Alloys. Ph.D. Thesis, University of Bremen, Bremen, Germany, 2020.

42. Çengel, Y.A. *Heat Transfer: A Practical Approach*, 1st ed.; McGraw-Hill: New York, NY, USA, 1998.

43. Anyalebechi, P.N. Effects of Alloying Elements and Solidification Conditions on Secondary Dendrite Arm Spacing in Aluminum Alloys. In Proceedings of the TMS Annual Meeting, Charlotte, NC, USA, 14–18 March 2004; Volume 2004, pp. 217–233.

44. Wiskel, J.B.; Navel, K.; Henein, H.; Maire, E. Solidification Study of Aluminum Alloys Using Impulse Atomization: Part II. Effect of Cooling Rate on Microstructure. *Can. Metall. Q.* **2002**, *41*, 193–204. [CrossRef]

45. Mullis, A.M.; Farrell, L.; Cochrane, R.F.; Adkins, N.J. Estimation of Cooling Rates during Close-Coupled Gas Atomization Using Secondary Dendrite Arm Spacing Measurement. *Metall. Mater. Trans. B* **2013**, *44*, 992–999. [CrossRef]

46. He, C.; Yu, W.; Li, Y.; Wang, Z.; Wu, D.; Xu, G. Relationship between Cooling Rate, Microstructure Evolution, and Performance Improvement of an Al-Cu Alloy Prepared Using Different Methods. *Mater. Res. Express* **2020**, *7*, 116501. [CrossRef]

47. Leander, F.; Pease, D.L. Metallography and Microstructures of Powder Metallurgy Alloys. In *Metallography and Microstructures Handbook*; Voort, V., Baldwin, W., Eds.; ASM International: Almere, The Netherlands, 2004; Volume 9, pp. 994–1020, ISBN 0871707063.

48. Stefanescu, D.M.; Ruxanda, R. Fundamentals of Solidification. In *Metallography and Microstructures Vol 9—ASM Handbook*; Vander Voort, G.F., Ed.; ASM International: Almere, The Netherlands, 2004; pp. 71–92.

49. Ferreira, A.F.; De Castro, J.A.; De Olivé Ferreira, L. Predicting Secondary-Dendrite Arm Spacing of the Al-4.5wt%Cu Alloy during Unidirectional Solidification. *Mater. Res.* **2017**, *20*, 68–75. [CrossRef]

50. Sharma, P. Analysis Anddesign of Cooling Chamber for Gas Atomization Plant. *Int. J. Curr. Res.* **2017**, *9*, 46614–46625.

51. Tourret, D.; Reinhart, G.; Gandin, C.A.; Iles, G.N.; Dahlborg, U.; Calvo-Dahlborg, M.; Bao, C.M. Gas Atomization of Al-Ni Powders: Solidification Modeling and Neutron Diffraction Analysis. *Acta Mater.* **2011**, *59*, 6658–6669. [CrossRef]

PAPER III

Centrifugal Atomization of Glass-Forming Alloy $Al_{86}Ni_8Y_{4.5}La_{1.5}$

Centrifugal Atomization of Glass-Forming Alloy Al$_{86}$Ni$_8$Y$_{4.5}$La$_{1.5}$

Jordi Pijuan [1],*, Sasha Alejandra Cegarra [1], Sergi Dosta [2], Vicente Albaladejo-Fuentes [3] and María Dolores Riera [4]

1   Eurecat, Centre Tecnològic de Catalunya, Unit of Metallic and Ceramic Materials, Plaça de la Ciència 2, 08243 Manresa, Spain

2   Departament de Ciència dels Materials i Química Física, Universitat de Barcelona, Martí i Franqués 1, 08028 Barcelona, Spain

3   Thermal Spray Centre (CPT), Departament de Ciència dels Materials i Química Física, Universitat de Barcelona, Martí i Franqués 1, 08028 Barcelona, Spain

4   Department of Mining, Industrial and ICT Engineering, Universitat Politècnica de Catalunya, Av. De les Bases de Manresa, 61-73, 08242 Manresa, Spain

*   Correspondence: jordi.pijuan@eurecat.org; Tel.: +34-938-777-373

Abstract: Centrifugal atomization is a rapid solidification technique for producing metal powders. However, its wide application has been limited to the production of common metal powders and their corresponding alloys. Therefore, there is a lack of research on the production of novel materials such as metallic glasses using this technology. In this paper, aluminum-based glassy powders (Al$_{86}$Ni$_8$Y$_{4.5}$La$_{1.5}$) were produced by centrifugal atomization. The effects of disk speed, atomization gas, and particle size on the cooling rate and the final microstructure of the resulting powder were investigated. The powders were characterized using SEM and XRD, and the amorphous fractions of the atomized powder samples were quantified through DSC analysis. A theoretical model was developed to evaluate the thermal evolution of the atomized droplets and to calculate their cooling rate. The average cooling rate experienced by the centrifugally atomized powder was calculated to be approximately 7×10^5 Ks^{-1} for particle sizes of 32.5 µm atomized at 40,000 rpm in a helium atmosphere. Amorphous fractions from 60% to 70% were obtained in particles with sizes of up to 125 µm in the most favorable atomization conditions.

Keywords: metallic glasses; centrifugal atomization; amorphous fraction; cooling rate

1. Introduction

Metallic glasses have attracted the interest of the scientific community for their possible applications due to their unique properties over their crystalline counterparts. Within amorphous metal alloys, Al-based metallic glasses have gained attention since their discovery in 1988 [1,2] because of their high specific strength [3,4] and high resistance to corrosion [5] compared to general-use aluminum alloys, which makes these materials an important target for their potential development in engineering applications.

Al-based metallic glasses have been proven to be very difficult to obtain due to their low glass-forming ability (GFA) compared to other metallic glasses [6,7]. The vast majority of the studied alloys are within the AL-RE-TM (aluminum, rare earths, and transition metals) system because they exhibit a higher GFA [8]. Yang et al. [4] produced glassy rods of 1 mm in diameter using copper mold casting, which is the largest product reported for Al-based metallic glasses with a composition of Al$_{86}$Ni$_6$Y$_{4.5}$Co$_2$La$_{1.5}$.

Low GFA suggests a higher critical cooling rate, therefore limiting the sample size that can be achieved in a fully amorphous structure. The cooling rate necessary to obtain amorphous Al-based alloys is in the order of 10^3–10^6 K s^{-1} [9]. Thus, the most viable way to manufacture these metallic glasses are through rapid cooling processes, with the most common including melt spinning [10] and gas atomization [11–13]. Although melt spinning is popular for scientific research, the maximum achievable size for specimens is

restricted [14]. On the other hand, for gas atomization, it has been found that the largest completely amorphous particle size obtained for these alloys are powders of less than 25 µm [15,16].

Although the resulting product of atomization methods is a powder, these techniques have maintained scientific interest due to the possibility of producing amorphous or partially amorphous powder that can be further processed using various technologies. Al-based metallic glass powders have been successfully deposited by cold gas spraying, demonstrating that is possible to maintain amorphous structure and to create functional coatings with high hardness and corrosion resistance [5,17,18]. Additionally, selective laser melting [19,20] and spark plasma sintering [21] had been demonstrated to be good techniques to maintain a partially amorphous structure of consolidated bulk specimens, but studies on Al-based amorphous alloys in these fields are still incipient.

Today, the production of Al-based metallic glasses is still challenging. An alternative technique to gas atomization for generating these materials is centrifugal atomization. During this process, molten metal is dropped onto a high-speed rotating disk. The liquid spreads out onto the disk by the centrifugal force and finally breaks into small droplets that solidify during their flight in the presence of an inert gas atmosphere. Cooling rates between 10^3 and 10^5 K s^{-1} can be reached using this method [22], thus providing an appropriate range of cooling rates for the generation of Al-based metallic glasses. However, a review of the literature reveals that although there are several works on the centrifugal atomization process [23–25], studies on the production of metallic glasses using this technique are not found in the literature.

In addition, centrifugal atomization has significant advantages compared to traditional gas atomization technology. The particle size distribution of the batch produced is narrower, resulting in a higher yield process. The powder that is produced has a highly spherical form, with better roundness and a smooth surface. Unlike gas atomization, satellites, which are adhesions of small particles on larger ones, are minimized. All of these powder characteristics significantly improve powder flowability, a key factor in additive manufacturing or thermal spraying technologies. Additionally, inert gas consumption and the energy consumption associated with it is significantly reduced, making centrifugal atomization highly beneficial in terms of sustainability and cost reduction.

In the present work, an $Al_{86}Ni_8Y_{4.5}La_{1.5}$ alloy was centrifugally atomized, and its microstructure and the amorphous fraction that were obtained were investigated as a function of gas composition and rotational disk speed. $Al_{86}Ni_8Y_{4.5}La_{1.5}$ was chosen because it showed a strong capacity in the formation of metallic glasses, as derived from an extensive study of aluminum-based bulk metallic glasses [26]. However, the centrifugal atomization of the powder resulting from this composition has never been reported on before. This research is aimed at characterizing the glass formation ability of the atomized $Al_{86}Ni_8Y_{4.5}La_{1.5}$ and at expanding our understanding of metallic glass preparation via the centrifugal atomization technique.

2. Materials and Methods

2.1. Powder Synthesis

A schematic diagram of the centrifugal atomization unit is shown in Figure 1. This equipment consists of three main parts: an atomization chamber to provide a controlled atmosphere; an induction melting system with a crucible that allows the metal to be melted in an inert gas atmosphere; and a spinning disk, which disintegrates the melt into fine particles.
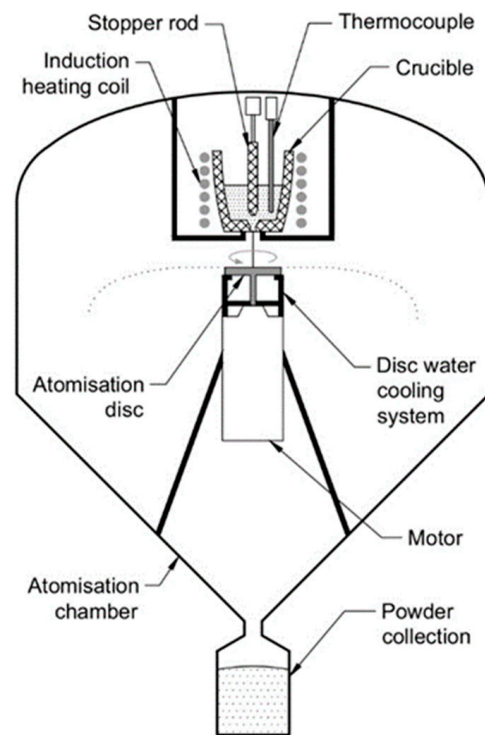
Figure 1. Schematic diagram of the centrifugal atomization equipment.

The raw materials used for alloy formation were commercial-purity Al-Y master alloy (90%Al-10%Y mass%), Y-La lump (12%Al-88%Y mass%), La-Ni eutectic pieces (12%Ni-88%La mass %), and commercially pure nickel 201 alloy (>99 Ni mass%). They were mixed in a molar composition of $Al_{86}Ni_8Y_{4.5}La_{1.5}$ and then induction-melted at 1605 K in an alumina crucible equipped with a stopper rod that allowed the melt to flow through the crucible orifice. The temperature was measured by means of a thermocouple located inside the crucible and was kept constant for 15 min to ensure homogenization and proper dissolution of all of the raw materials. Prior to melting and atomization, a vacuum pump was run to depressurize the chamber to 10^{-3} Pa and was subsequently backfilled with inert gas. During the atomization process, the stopper rod was pulled up, and the melt was gravity poured through the 3 mm orifice onto a flat 40 mm diameter 316 L stainless steel disk rotating at a high speed. This disk had a 150 μm ZrO_2 coating on the upper surface in contact with the melt. A water-cooling system was used to guarantee the integrity of the disk due to the high temperatures of atomization.

The main processing parameters for this study were the disk speed and the inert gas atmosphere. A set of test runs were carried out, melting a total of 350 g of the starting materials for each experiment. Process conditions consisted of analyzing two different disk speeds: 30,000 rpm and 40,000 rpm; and three combinations of different gas compositions (in volume %): 100% Ar (Ar), 50%He-50%Ar (He-Ar), and 100% He (He).

2.2. Powder Characterization

The powder obtained from each atomization run was collected and sieved according to ASTM-B215 for 15 min with a Filtra FTL-0150 electromagnetic digital sieving machine with 20, 45, 75, 106, 125, 150, and 180 μm sieves according to the corresponding particle fraction sizes.

The particles were then embedded in cold-mounting resin, ground, and polished with diamond suspension solution and finished with a colloidal dispersion of silica (SiO_2) using standard metallographic methods for uncompacted metal powders [27]. The surface morphology and microstructure of the powders were investigated using an Ultra Plus field-emission scanning electron microscope (SEM). The chemical compositions of the atomized

powders were checked by inductively coupled plasma optical emission spectroscopy (ICP-OES) using Thermo Scientific iCAP PRO. X-ray diffraction analysis of the sieved Al alloy powder was performed in order to verify the production of amorphous material, even for high-size powder fractions. XRD patterns were recorded using PANalytical X'Pert PRO MPD equipment with Cu Kα radiation (λ = 1.5418 Å) from 5 to 100° 2θ with a 0.017° step, measuring 100 s per step. The differential scanning calorimetry (DSC) technique was selected to determine the volume fraction of the amorphous (V_f) phase present in the different powder fractions produced by centrifugal atomization. For this analysis, a DSC1 Mettler Toledo was used, and the measurements were conducted under a nitrogen atmosphere using aluminum crucibles. For the test, 20 mg of each powder was heated from 300 K to 800 K at 10 K/min rate.

3. Results

A summary of the test runs performed, their atomizing conditions, and the particle size distribution of the obtained powders is presented in Table 1. The particle size distributions of the atomized powders at 40,000 rpm are finer than those atomized at 30,000 rpm. This result is coherent with the known state-of-the-art of centrifugal atomization [28], as the higher the disk velocity, the lower the particle size that can be achieved. Regarding the gas atmosphere used in atomization, no clear tendency was found in the particle size distribution results, allowing us to conclude that the nature of the gas does not affect the particle size distribution.

Table 1. Description of atomization runs and particle size distribution obtained.

Run #	Disc Velocity (rpm)	Gas Composition	D_{10} (µm)	D_{50} (µm)	D_{90} (µm)
1	30,000	He	63	111	165
2	30,000	He-Ar	77	136	231
3	30,000	Ar	78	127	193
4	40,000	He	55	96	156
5	40,000	He-Ar	59	102	155
6	40,000	Ar	51	90	150

Chemical analysis by inductively coupled plasma (ICP) of the final powder indicates that the alloy composition is close to the desired nominal composition. The final composition of the powder was Ni:8.1, Y: 4.6, La: 1.6, Al: bal. (in atomic %).

3.1. SEM Analysis

SEM images of the powders in the particle size range of 75–45 µm atomized under different conditions are shown in Figure 2. Most of the powder particles were spherical in shape. The surfaces of particles atomized in a He atmosphere were very smooth, and direct observations did not show a crystalline structure, whereas particles atomized in He-Ar—and to a larger extent, in Ar atmospheres—presented rough surfaces that are related to the formation of crystalline phases.

Micrographs of centrifugally atomized particle sizes synthesized in a He atmosphere are shown in Figure 3. Figure 3a shows the cross-section micrograph of the 45–20 µm particle size range, where the majority of the particles have a featureless structure. In some particles, small Al_2Y crystals (less than 10 µm in length) surrounded by the featureless structure appear [15]. It is important to notice that for the smaller particle sizes, it cannot be determined if the particles are completely featureless. SEM observations only show the cross section of the particles, meaning that they may have a certain degree of crystallization that remains unknown.
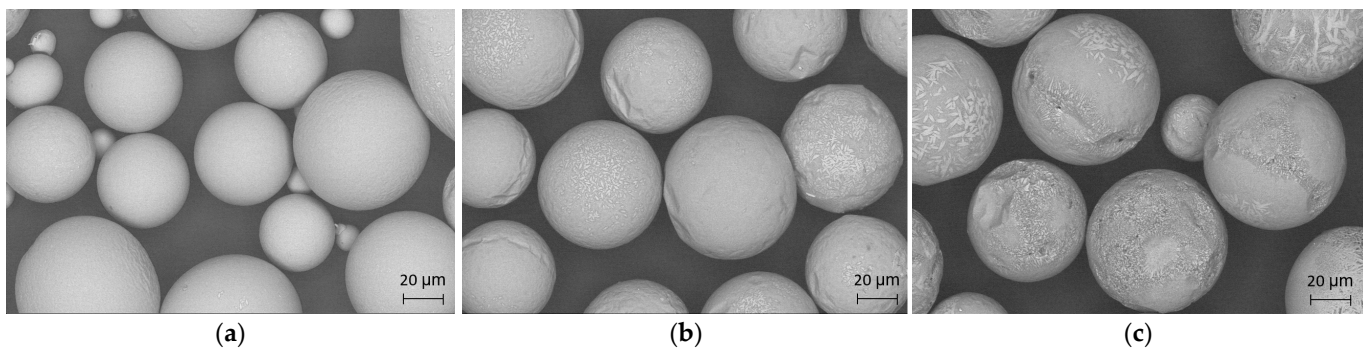
Figure 2. Surface morphology of the resulting powder in the size range of 75–45 μm atomized at the same speed of 40,000 rpm using different gas compositions: (**a**) He; (**b**) He-Ar; (**c**) Ar.
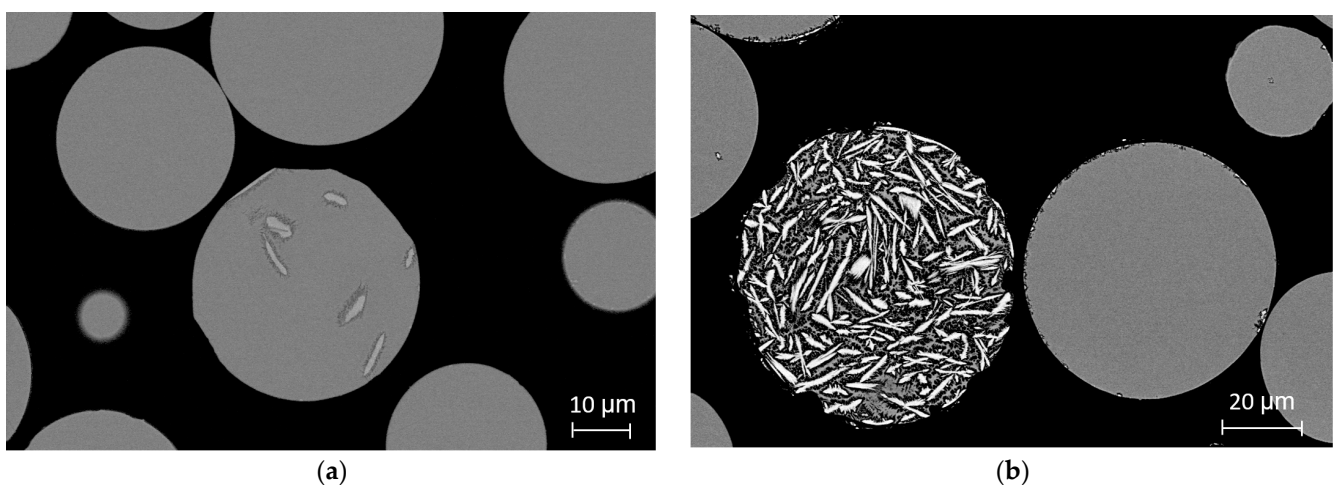
Figure 3. Cross-section SEM micrographs of particles centrifugally atomized in a He atmosphere at 40,000 rpm: (**a**) 45–20 μm; (**b**) 45–75 μm.

A similar pattern is detected in the micrographs of the 75–45 μm particle range. In Figure 3b, most of the particles also appear to be featureless, but some of them are clearly crystallized, with high-length crystals and a heterogeneous crystallographic structure that is typical of the crystallization of Al-Ni-Y alloys [12,16]. High randomness is noticed in the microstructure between particles for the same particle size range and atomization conditions, in which some seem totally amorphous, and others are almost totally crystalline. Despite this disparity, a clear pattern appears in the proportion of featureless and crystallized particles depending on particle size and atomization gas. In small particle size ranges and in particles atomized in He, the majority of the particles present a featureless structure, while in large particle size ranges atomized in He-Ar and Ar, almost the totality of the particles are fully crystallized.

3.2. XRD Analysis

XRD patterns of centrifugally atomized powder samples at different gas compositions and disk speeds are shown in Figure 4. Phase identification in Figure 4 is based on results from [12]. From these diffraction patterns, it can be verified that the crystalline fraction increases with the particle size, even for different gas compositions, as previously observed in the micrographs.
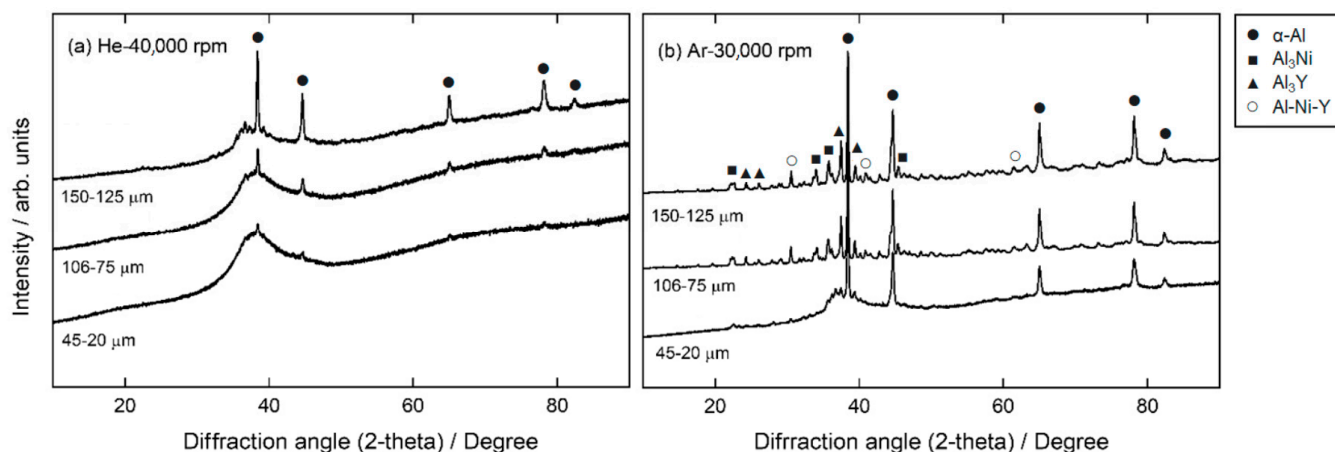
Figure 4. XRD pattern for centrifugally atomized particles: (**a**) particles atomized in a He atmosphere at 40,000 rpm, and (**b**) particles atomized in an Ar atmosphere at 30,000 rpm. The intensity of the crystalline peak increases with increasing particle sizes, indicating a higher crystalline fraction.

When comparing the diffraction patterns of particles atomized in He and Ar, it is clear that particles atomized in an Ar atmosphere have more crystallinity than particles atomized in a He atmosphere. A broad amorphous halo was observed in the particles atomized in a He atmosphere at a disk speed of 40,000 rpm, indicating the formation of an amorphous structure up to a particle class size of 125–106 μm. However, even for small particle sizes (45–20 μm), small diffraction peaks close to the background signal indicate that these particles are not fully amorphous. Peaks appear more clearly as the particle size increases, indicating an increase in the crystalline fraction in larger particles. These peaks correspond to the α-Al phase [29]. In comparison, the XRD patterns of particles atomized in an Ar atmosphere at a disk speed of 30,000 rpm show clear diffraction peaks, even in particle sizes of 45–20 μm. For particles > 75 μm atomized in an Ar atmosphere, the DRX results correspond to an almost entirely crystalline pattern, as no halo is identified in these cases.

3.3. DSC Analysis

Figure 5 shows a DSC measurement from room temperature to 800 K (10 K min^{-1}) for a 45–75 μm particle size range sample atomized in a He atmosphere at a disk speed of 40,000 rpm. DSC curves for the different gas compositions and the same particle range are shown in the inset in Figure 5. The DSC curve of the ribbon sample is adapted from [26]. For all of the atomization conditions, the DSC curves exhibited a three-stage crystallization process characterized by three peak crystallization temperatures, as expected for this alloy. No detailed analysis of the crystallization of the $Al_{86}Ni_8Y_{4.5}La_{1.5}$ glass-forming alloy is found in the literature. However, other similar compositions are studied in detail. The first peak corresponds to nano-Al precipitation, the second peak corresponds to the growth of alpha-phase nanocrystals and the formation of Al_3Ni and Al-Ni-Y phases, and the third peak corresponds to the growth of existing crystals and to the formation of Al-La phases [4,30]. No sign of glass transition temperature (T_g) was detected from the DSC curve. For most of the Al-based metallic glasses, the supercooled liquid region is small; therefore, the glass transition signal and the onset of the crystallization signal tend to overlap [5,31].
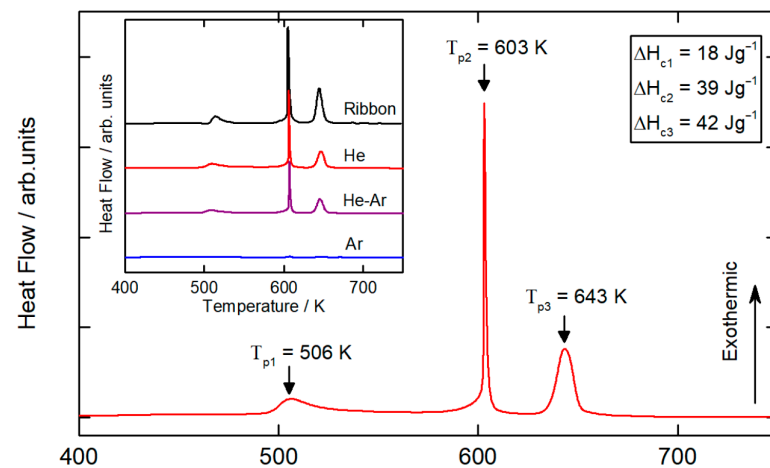
Figure 5. DSC measurements for 75–45 μm particles atomized in a He atmosphere at 40,000 rpm. ΔH_{c1}, ΔH_{c2}, and ΔH_{c3} are the integrated enthalpies of crystallization for the first, second, and third peaks, respectively. Inset in the figure shows the DSC curves of the respective samples atomized in different gas compositions, and DSC curve of ribbon sample is adapted from [26].

3.4. Determination of Amorphous Fraction

The volume fraction of the amorphous phase (V_f) in each atomized particle size range was evaluated by normalizing the enthalpy released during the crystallization of the powder with the enthalpy of crystallization of a fully amorphous melt-spun ribbon sample using the following equation:

$$V_f = (\Delta H_{T,Am} - \Delta H_{T,\,PAm})/\Delta H_{T,\,Am} \tag{1}$$

where $\Delta H_{T,Am}$ is the total enthalpy released upon the crystallization of a fully amorphous sample, and $\Delta H_{T,PAm}$ is the total enthalpy released upon the crystallization of a partially amorphous sample. For this work, the enthalpy of the crystallization of the fully amorphous melt-spun ribbon sample was taken from Yang et al. and used as a reference [26].

The heat released during the three exothermic reactions was compared with the heat released from the three exothermic reactions of the fully amorphous $Al_{86}Ni_8Y_{4.5}La_{1.5}$ melt-spun ribbon of the identical crystallization sequence. Figure 6 gathers the total amorphous volume fraction present in the atomized particles as a function of the corresponding size range for the different conditions of atomization.
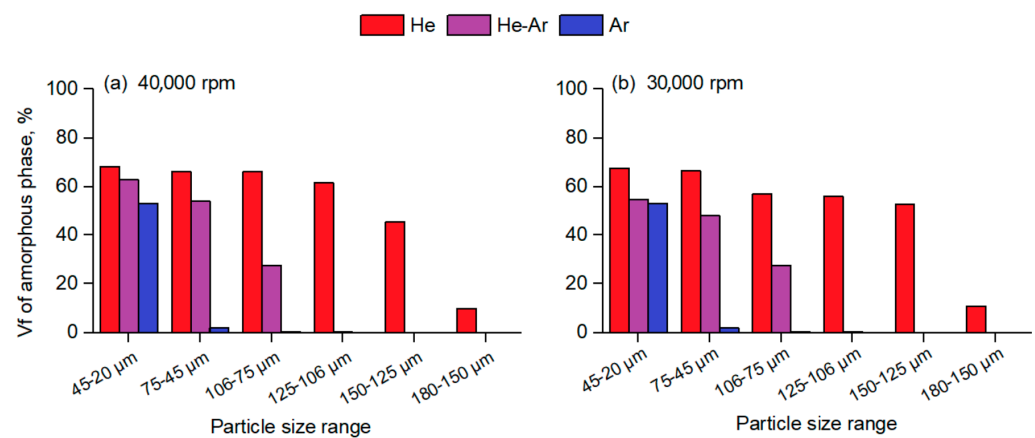
Figure 6. Amorphous volume fraction of the centrifugally atomized $Al_{86}Ni_8Y_{4.5}La_{1.5}$ powder as a function of the corresponding particle size range using different gas compositions: (**a**) particles atomized at a disk speed of 40,000 rpm; (**b**) particles atomized at a disk speed of 30,000 rpm.

Figure 6a shows that for a given particle size range, centrifugally atomized powders prepared in a He atmosphere have a much higher amorphous fraction than powders atomized in an Ar and He-Ar atmosphere, whereas Figure 6b shows that changes in the disk speed do not seem to have a significant effect on the achieved amorphous fraction compared to the gas composition. From Figure 6, it can be seen that centrifugally atomized powders prepared in a He atmosphere, either at 30,000 rpm or 40,000 rpm, have a high amorphous fraction of 60% to 70% in particle size ranges of up to 125–106 μm. To the authors' knowledge, there are few data on amorphous volume fractions in atomized alloys in the existing literature related to the Al-TM-RE system [5,12,13]. The literature suggests that a high percentage of amorphous fractions have only been found for particle sizes <40 μm for particles atomized via gas atomization, even for those atomized in a He atmosphere.

3.5. Thermal Evolution of Atomized Droplets

A mathematical heat transfer analysis was used to quantify the heat transport between the surrounding gas and the centrifugally atomized droplets. Particle trajectories along the atomization chamber were computed according to Yule [32] by considering drag force and gravity force and by assuming an initial velocity equal to the tangential velocity of the disk [33]. A homogeneous temperature distribution inside the droplet is assumed to be due to rapid heat conduction within the particle compared with convection heat transfer from the surface of the droplet and the surrounding gas [34]. Radiation is considered to be negligible due to the low contribution on the cooling rate compared to convection, which is around an order of magnitude lower [11,32]. To calculate the effective heat transfer coefficient h, the Nusselt number Nu from the semi-empirical equation based on the Whitaker correlation [34] was used [34], which considers the temperature-dependent thermophysical properties of the gas in an environment with a high temperature gradient [35]:

$$Nu = h\,d/k_g = 2 + \left(0.4Re^{1/2} + 0.06Re^{2/3}\right)Pr^{1/4}\left(\mu_g/\mu_s\right)^{1/4} \tag{2}$$

where d is the droplet diameter, k_g and μ_g are the thermal conductivity and the viscosity of the gas evaluated at ambient temperature, respectively, and μ_s is the gas viscosity evaluated at the temperature of the surface of the droplet. Nu includes the Reynolds number Re and the Prandtl number Pr, which are defined as:

$$R_e = \rho_g\,v\,d/\mu_g \tag{3}$$

and

$$P_r = C_{pg}\,\mu_g/k_g \tag{4}$$

where C_{pg} and ρ_g are the specific heat capacity and density of the gas evaluated at the ambient temperature inside the atomizer, respectively, and v is the droplet velocity.

For simplicity, the thermophysical properties for pure Al liquid were used for the $Al_{86}Ni_8Y_{4.5}La_{1.5}$ alloy. The glass transition temperature T_g of the $Al_{86}Ni_8Y_{4.5}La_{1.5}$ alloy was taken as 507 K [26]. Since the experiment involved metallic glass powder, this calculation was performed by assuming that no phase change takes place during the cooling of the molten metal from the atomization temperature to the glass transition temperature T_g [11,36]. Thus, for the cooling rate calculation, it was assumed that undercooling takes place below the glass transition temperature.

Figure 7 shows the cooling evolution of the atomized droplets from the atomization temperature to the glass transition temperature in the different study cases. Droplets from the lower diameter are cooled more rapidly, and He provides the best cooling rate. Comparing the cases of equal atmosphere and different disk velocities, only a slight improvement in the cooling rate is observed at higher velocities. In the case of He atomization, all of the droplets reach the glass transition temperature in 20 ms, while in a He-Ar atmosphere, only particles of around 100 μm in size achieve this cooling time, and only finer particles below

50 μm reach this condition in an Ar atmosphere. The largest time interval is 150 ms for droplets of 165 μm in size atomized in Ar.
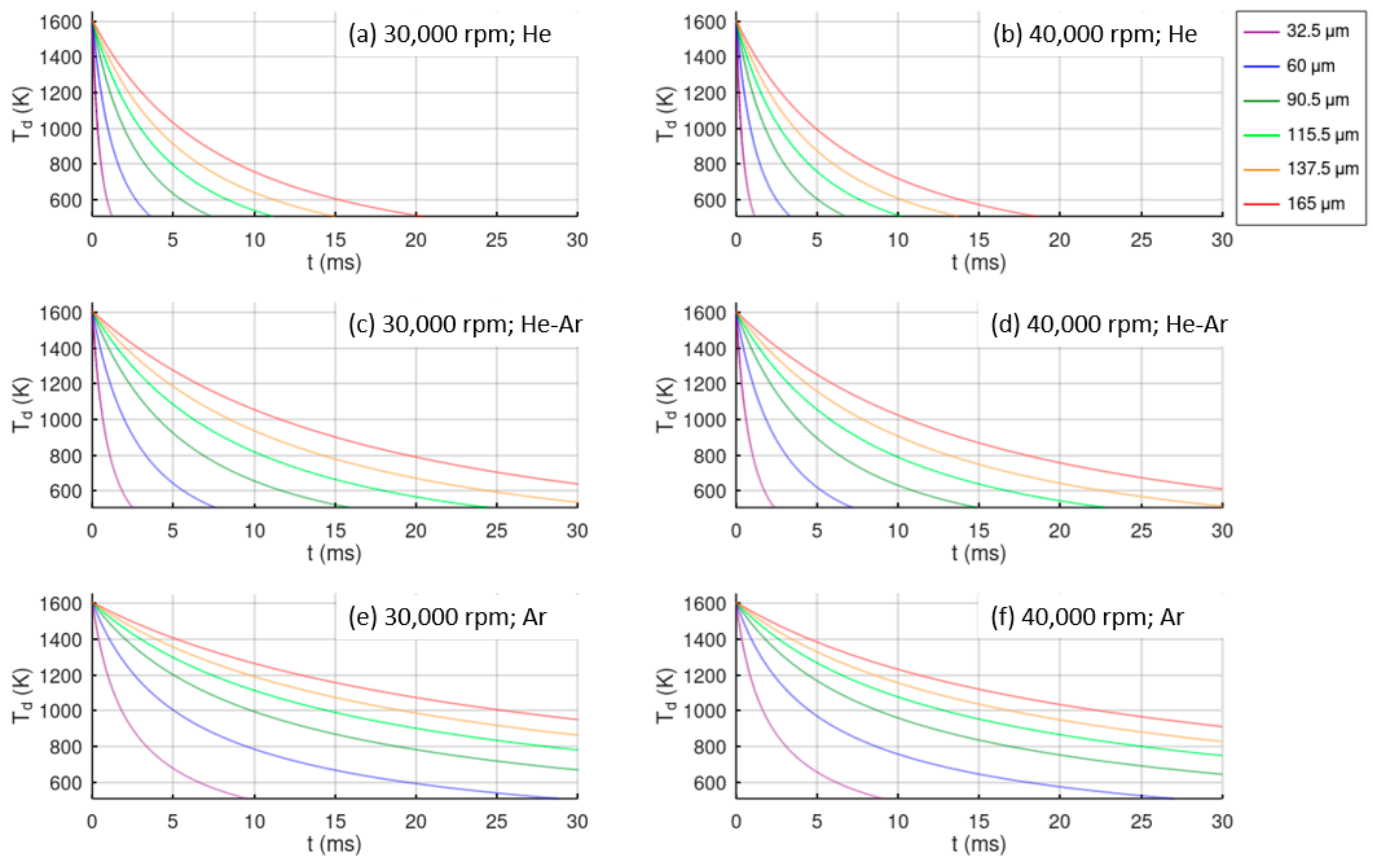
Figure 7. Temperature variation in centrifugally atomized droplets of different sizes in different atomization conditions of disk velocity and gas atmosphere.

4. Discussion

4.1. Cooling Rate Calculation

The cooling rate of the atomized droplets, assuming no phase change appears before reaching the glass transition temperature, can be evaluated as [32]:

$$\dot{T} = \frac{6h(T_d - T_\infty)}{C_{pl}d} \tag{5}$$

where T_d is the droplet temperature, T_∞ is the temperature of the gas atmosphere, and C_{pl} is the specific heat capacity of the droplet. In Figure 8, the values of the cooling rate over time for different particle sizes and atomization conditions are represented. These plots represent the cooling rate experienced by the particles from the initial melt temperature to the glass transition temperature T_g. The case studies for 30,000 rpm are not shown due to similarity with the 40,000 rpm cases. As mentioned before, He provides larger cooling rates, and Ar provides the lowest cooling rates, and finer droplets are also cooled more rapidly.

A droplet of 33 μm in a He atmosphere experiences a cooling rate between 2×10^6 Ks^{-1} and 1.5×10^5 Ks^{-1} from the melt temperature to the glass transition temperature. In the case of an Ar atmosphere, these values are reduced by approximately an order of magnitude. Comparing the different atmosphere gas cases, droplets of 137.5 μm have a cooling rate approximately an order for magnitude lower than 33 μm droplets. Even finer particles of 33 μm atomized in an Ar atmosphere have a higher cooling rate than large particles of 137.5 μm atomized in a He atmosphere do.
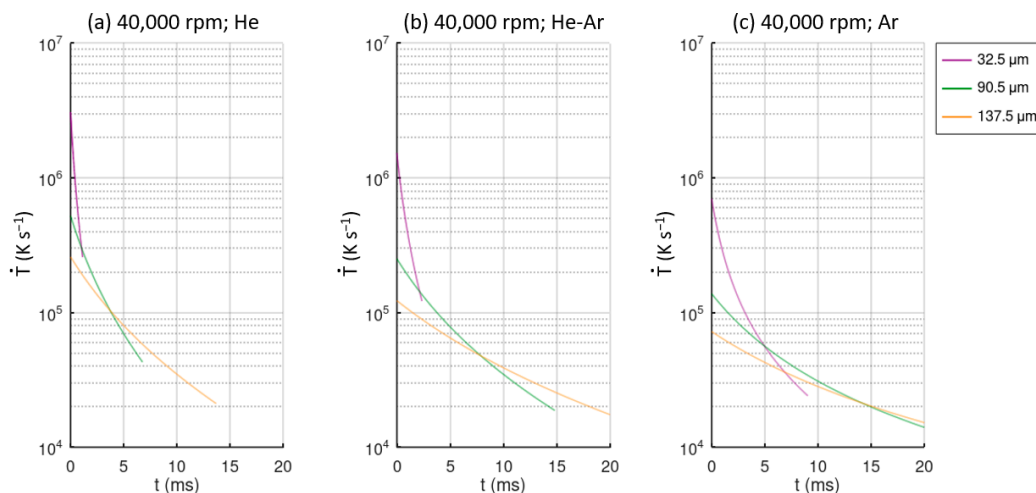
Figure 8. Cooling rate value over time for different particle sizes and different atomization conditions: (**a**) He atmosphere; (**b**) He-Ar atmosphere; (**c**) Ar atmosphere. All cases correspond to a disk velocity of 40,000 rpm.

4.2. Comparison between Cooling Rate and Amorphous Fraction

In order to obtain comparable and interpretable results between the cooling rate and the amorphous fraction, an average cooling rate is preferred for the entire cooling process CR instead of $\dot{T}$, and this is evaluated as [36]:

$$CR = \frac{T_L - T_g}{t_L - t_g} \tag{6}$$

where $t_L - t_g$ is the time between the liquidus temperature T_L and the glass transition temperature T_g.

Figure 9 illustrates the average cooling rate CR as a function of particle size with the corresponding amorphous fraction obtained from the DSC data for different gas compositions. The amorphous fraction decreases rapidly for cooling rates below 6×10^4 Ks^{-1} for all the atomization conditions.
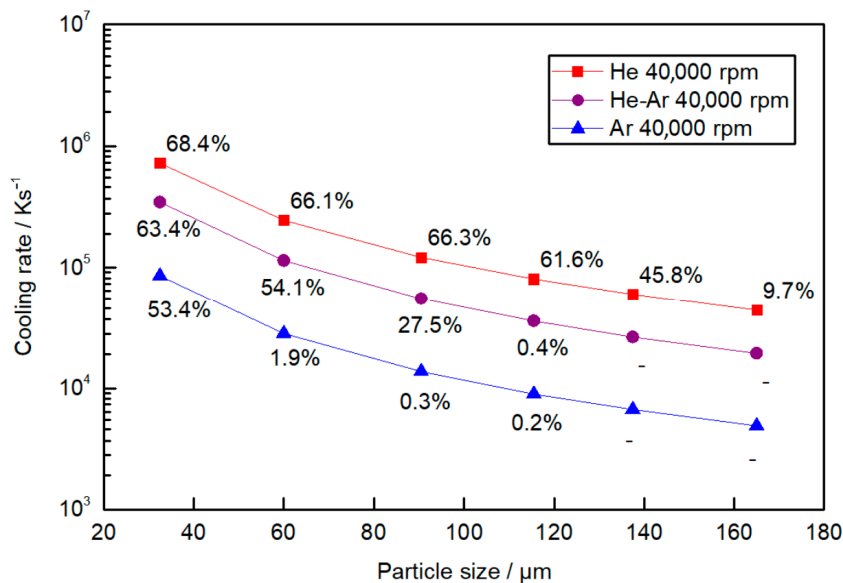
Figure 9. Cooling rate as a function of particle size atomized in a He, Ar, and He-Ar atmospheres at a disk speed of 40,000 rpm. The data points represent the amorphous fraction calculated from the DSC results for the corresponding mean particle size range.

The maximum cooling rate is achieved in a He atmosphere, where particles of 32.5 μm experience an average cooling rate of 7×10^5 K s^{-1}. In an Ar atmosphere, the cooling rate decreases an order of magnitude compared to the cooling rate achieved in a He atmosphere for the same particle sizes. Particles of 32.5 μm have an average cooling rate of an order magnitude higher than particles of 165 μm atomized in the same atmosphere. Hence, it is concluded that He has a stronger effect than Ar, resulting in a higher cooling rate, which is in good agreement with the literature [36,37]. This is mainly due to the thermal conductivity of He being greater than that of Ar (1.52×10^{-1} Wm^{-1} k^{-1} value for He and 1.77×10^{-2} Wm^{-1} k^{-1} for Ar, both at 300 K, which is the initial temperature of the gas in the atomization chamber). The particle diameter also has a strong influence on the cooling rate and is as important as the gas atmosphere.

In a case where the same cooling rate is taken for any of the atmospheres, a similar amorphous fraction is obtained independently of the particle size diameter. For example, a similar cooling rate and a similar amorphous fraction are obtained for 32.5 μm particles atomized in Ar and 120 μm particles atomized in He. The same pattern is found when comparing particles atomized in a He atmosphere that are 150 μm in size and particles atomized in Ar that are 60 μm in size, whereas in this case, both appear to be almost fully crystalline.

4.3. Effect of Gas Composition in Amorphous Fraction

The cooling rates necessary to achieve completely amorphous microstructures in Al-based metallic glasses have been calculated theoretically for different techniques such as gas atomization and melt spinning [11,38]. In both cases, the cooling rate was estimated to be 10^6 Ks^{-1}. Figure 9 shows that in a He atmosphere, although particle sizes of 45–20 μm achieved a cooling rate of near 10^6 Ks^{-1}, the amorphous fraction obtained in this work is below 70%. However, in a He atmosphere, the amorphous fraction value is kept relatively stable, with a slight decrease as the droplet diameter increases in particles of up to 125 μm in size, after which the amorphous fraction decreases rapidly. In a He-Ar atmosphere, this rapid decrease appears at particle sizes of 90 μm and at around 40 μm in an Ar atmosphere. Comparing these results with time intervals in Figure 7, a significant amorphous fraction is obtained in all cases if the particles are cooled in at least 15 ms, which represents an average cooling rate of 7.3×10^4 Ks^{-1}. This cooling rate value is larger than those experimentally determined in a laboratory with melt spinning, which are between 3×10^3 and 10^4 Ks^{-1} [9].

The obtention of particles that are not fully amorphous but that achieve the required cooling rates may be due to impurities or oxide particles from the raw material that act as nucleation sites that favor the crystallization of the final powder [39]. Consequently, it is difficult to obtain fully amorphous powders since these impurities may cause crystalline phases. Commercial starting materials and commercial alumina crucibles were used in atomization experiments, and these may be the result of a higher presence of impurities in the atomized melt. The presence of impurities could also justify the wide variability in the particle microstructure shown in Figure 3b depending on whether the presence of an impurity acts as nucleation point in the atomized droplet.

Although a fully amorphous fraction has not been achieved in any particle size range, a significant amorphous fraction is obtained in particle sizes of up to 125 μm atomized in a He atmosphere. This demonstrates that centrifugal atomization is able to achieve high cooling rates, even in large particles.

Another aspect that can contribute to crystallization is melt superheat. Some investigations have concluded that a lower melt superheat temperature contributes to the cooling path not reaching the crystallization zone in the time–temperature–transformation diagram [40]. A high melt superheat of 1605 K was used in the atomization runs (400 K above liquidus temperature) to guarantee the complete melting of the starting materials and to avoid possible melt solidification in the atomization disk. In this study, the cooling effect of the atomization disk in the melt is an aspect that has been assumed to have no significant

influence, but detailed analysis should be required to estimate the initial temperature of the droplet when it is expelled from the atomization disk.

4.4. Effect of Disk Speed in Amorphous Fraction

Particles atomized at different disk speeds do not show a significant change in the microstructure. Theoretical results show a minor decrease in the cooling rate at lower disk speed, and there is also a slight reduction in the amorphous fraction for particles atomized at 30,000 rpm compared to particles atomized at 40,000 rpm. The experimental and theoretical results show that disk velocity does not contribute to an increase in the cooling rate of the particles. An increase of 33% in the disk velocity, and therefore in the droplet initial velocity, while contributing to the increase in the heat transfer coefficient between the droplet and the surrounding gas, has no significant effect on the cooling rate compared to other variables such as droplet diameter and the gas atmosphere. Nevertheless, disk velocity will have a strong influence on obtaining finer droplets and will contribute to the overall yield to obtain powders with a higher amorphous fraction.

5. Conclusions

Powder samples of $Al_{86}Ni_8Y_{4.5}La_{1.5}$ glass-forming alloy were atomized by centrifugal atomization technology. The influence of processing parameters such as disk speed and gas composition was studied. Most of the powders were spherical in shape, while the surface morphology was different for the finer and the coarser powders. Powders of particle sizes below 45 μm mainly had a smooth morphology where no optically detectable microstructure was identified. However, as the particle size increased, partially crystalline and fully crystalline microstructures were observed.

The volume fraction of the amorphous phase for various particle size ranges were determined from DSC analysis. Centrifugally atomized particles synthesized in a He atmosphere resulted in an amorphous fraction of around 70% for particle sizes <45 μm and between 50% and 65% for particle sizes <125 μm. However, particles atomized in an Ar atmosphere resulted in an amorphous fraction of 55% for particle sizes <45 μm, and this value decreased sharply as the particle size increased. Limitations in achieving a fully amorphous fraction might be due to the presence of nucleants in the melt during the atomization process.

The cooling rate experienced by centrifugally atomized powders was determined theoretically. As expected, the cooling rate increases as the particle size decreases. A cooling rate of 7×10^5 Ks^{-1} for particles of 32.5 μm atomized in a He atmosphere was obtained, and this value was reduced by one order of magnitude for particles atomized in an Ar atmosphere. As for the disk speed, no significant increase in the amorphous fraction was observed as the disk speed increased from 30,000 rpm to 40,000 rpm.

The results show that the centrifugal atomization technique is able to achieve cooling rates that are high enough to obtain an amorphous fraction above 50% in particle sizes of up to 125 μm using a He atmosphere. Although more research is necessary to achieve a higher amorphous fraction, it is demonstrated that centrifugal atomization is a viable technique for obtaining amorphous powders of larger particle sizes in alloys with a low glass-forming ability, such as Al-based metallic glasses.

Institutional Review Board Statement: Not applicable.

Informed Consent Statement: Not applicable.

Data Availability Statement: Data are contained within the article.

Conflicts of Interest: The authors declare no conflict of interest.

References

1. Inoue, A.; Ohtera, K.; Masumoto, T. New Amorphous Al-Y, Al-La and Al-Ce Alloys Prepared by Melt Spinning. *Jpn. J. Appl. Phys.* **1988**, *27*, L736–L739. [CrossRef]
2. He, Y.; Poon, S.J.; Shiflet, G.J. Synthesis and Properties of Metallic Glasses That Contain Aluminum. *Science* **1988**, *241*, 1640–1642. [CrossRef] [PubMed]
3. Inoue, A.; Kimura, H. High-Strength Aluminum Alloys Containing Nanoquasicrystalline Particles. *Mater. Sci. Eng. A* **2000**, *286*, 1–10. [CrossRef]
4. Yang, B.J.; Yao, J.H.; Zhang, J.; Yang, H.W.; Wang, J.Q.; Ma, E. Al-Rich Bulk Metallic Glasses with Plasticity and Ultrahigh Specific Strength. *Scr. Mater.* **2009**, *61*, 423–426. [CrossRef]
5. Henao, J.; Concustell, A.; Cano, I.; Dosta, S.; Cinca, N.; Guilemany, J.M.; Suhonen, T. Novel Al-Based Metallic Glass Coatings by Cold Gas Spray. *Mater. Des.* **2016**, *94*, 253–261. [CrossRef]
6. Yang, B.J.; Lu, W.Y.; Zhang, J.L.; Wang, J.Q.; Ma, E. Melt Fluxing to Elevate the Forming Ability of Al-Based Bulk Metallic Glasses. *Sci. Rep.* **2017**, *7*, 11053. [CrossRef]
7. Liang, X.; Fan, C.; Fu, J.; Liu, Z.; Zhang, Z.; Ren, S.; Ruan, W.; Shi, H. Improve the Forming Ability of Al-Based Metallic Glass Under Ultrasonic Vibration at Room Temperature. *Front. Mater.* **2021**, *8*, 361. [CrossRef]
8. Fan, C.; Yue, X.; Inoue, A.; Liu, C.T.; Shen, X.; Liaw, P.K. Recent Topics on the Structure and Crystallization of Al-Based Glassy Alloys. *Mater. Res.* **2019**, *22*. [CrossRef]
9. Liao, J.P.; Yang, B.J.; Zhang, Y.; Lu, W.Y.; Gu, X.J.; Wang, J.Q. Evaluation of Glass Formation and Critical Casting Diameter in Al-Based Metallic Glasses. *Mater. Des.* **2015**, *88*, 222–226. [CrossRef]
10. Yang, H.W.; Wang, R.C.; Yuan, X.G.; Li, R.D.; Wang, J.Q.; Tan, M.J. Importance of Chamber Gas Pressure on Processing of Al-Based Metallic Glasses during Melt Spinning. *Philos. Mag. Lett.* **2011**, *91*, 656–663. [CrossRef]
11. Zheng, B.; Lin, Y.; Zhou, Y.; Lavernia, E.J. Gas Atomization of Amorphous Aluminum: Part I. Thermal Behavior Calculations. *Metall. Mater. Trans. B* **2009**, *40*, 768–778. [CrossRef]
12. Dong, P.; Hou, W.L.; Chang, X.C.; Quan, M.X.; Wang, J.Q. Amorphous and Nanostructured $Al_{85}Ni_5Y_6Co_2Fe_2$ Powder Prepared by Nitrogen Gas-Atomization. *J. Alloys Compd.* **2007**, *436*, 118–123. [CrossRef]
13. Cardoso, K.R.; Escorial, A.G.; Lieblich, M.; Botta F, W.J. Amorphous and Nanostructured Al-Fe-Nd Powders Obtained by Gas Atomization. *Mater. Sci. Eng. A* **2001**, *315*, 89–97. [CrossRef]
14. Jassim, A.K.; Hammood, A.S. Sustainable Manufacturing Process for Bulk Metallic Glasses Production Using Rapid Solidification with Melt Spinning Technique. In Proceedings of the International Conference on Material Science and Material Engineering (MSME 2014), Chicago, IL, USA, 14–16 March 2014. [CrossRef]
15. Yan, M.; Wang, J.Q.; Schaffer, G.B.; Qian, M. Solidification of Nitrogen-Atomized Al86Ni6Y 4.5Co2La1.5 Metallic Glass. *J. Mater. Res.* **2011**, *26*, 944–950. [CrossRef]
16. Liu, Y.; Liu, Z.; Guo, S.; Du, Y.; Huang, B.; Huang, J.; Chen, S.; Liu, F. Amorphous and Nanocrystalline $Al_{82}Ni_{10}Y_8$ Alloy Powder Prepared by Gas Atomization. *Intermetallics* **2005**, *13*, 393–398. [CrossRef]
17. Sun, C.; Zhou, X.; Xie, C. Effect of Processing Conditions on Al-Based Amorphous/Nanocrystalline Coating by Cold-Spraying. *Surf. Coat. Technol.* **2019**, *362*, 97–104. [CrossRef]
18. Sun, C.; Zhou, X.; Xie, C.; Xu, L.; Li, R.; Liu, B. Formation of Al-Based Amorphous/Nanocrystalline Coatings by Cold Spraying. *Surf. Coat. Technol.* **2020**, *389*, 125644. [CrossRef]
19. Li, X.P.; Kang, C.W.; Huang, H.; Zhang, L.C.; Sercombe, T.B. Selective Laser Melting of an $Al_{86}Ni_6Y_{4.5}Co_2La_{1.5}$ Metallic Glass: Processing, Microstructure Evolution and Mechanical Properties. *Mater. Sci. Eng. A* **2014**, *606*, 370–379. [CrossRef]
20. Prashanth, K.G.; Shakur Shahabi, H.; Attar, H.; Srivastava, V.C.; Ellendt, N.; Uhlenwinkel, V.; Eckert, J.; Scudino, S. Production of High Strength $Al_{85}Nd_8Ni_5Co_2$ Alloy by Selective Laser Melting. *Addit. Manuf.* **2015**, *6*, 1–5. [CrossRef]
21. Scudino, S.; Surreddi, K.B.; Nguyen, H.V.; Liu, G.; Gemming, T.; Sakaliyska, M.; Kim, J.S.; Vierke, J.; Wollgarten, M.; Eckert, J. High-Strength $Al_{87}Ni_8La_5$ Bulk Alloy Produced by Spark Plasma Sintering of Gas Atomized Powders. *J. Mater. Res.* **2009**, *24*, 2909–2916. [CrossRef]
22. Öztürk, S.; Arslan, F.; Öztürk, B. Effect of Production Parameters on Cooling Rates of AA2014 Alloy Powders Produced by Water Jet Cooled, Rotating Disc Atomisation. *Powder Metall.* **2003**, *46*, 342–348. [CrossRef]

23. Denmud, N.; Plookphol, T. Characteristics of SAC305 Lead-Free Powder Prepared by Centrifugal Atomization. *Key Eng. Mater.* **2018**, *777*, 322–326. [CrossRef]

24. Mantripragada, V.T.; Kumar, K.; Kumar, P.; Sarkar, S. Modeling of Powder Production During Centrifugal Atomization. *J. Sustain. Metall.* **2021**, *7*, 620–629. [CrossRef]

25. Wolf, S.; Riedemann, T.M.; Barclay, J.; Holladay, J.; Anderson, I.E.; Cui, J. Synthesis and Magnetic Performance of Gadolinium Powder Produced with Rotating Disk Atomization. *Powder Technol.* **2020**, *359*, 331–336. [CrossRef]

26. Yang, B.J.; Yao, J.H.; Chao, Y.S.; Wang, J.Q.; Ma, E. Developing Aluminum-Based Bulk Metallic Glasses. *Philos. Mag.* **2010**, *90*, 3215–3231. [CrossRef]

27. Leander, F.; Pease, D.L. Metallography and Microstructures of Powder Metallurgy Alloys. In *Metallography and Microstructures Handbook*; Voort, V., Baldwin, W., Eds.; ASM International: Novelty, OH, USA, 2004; Volume 9, pp. 994–1020.

28. Xie, J.W.; Zhao, Y.Y.; Dunkley, J.J. Effects of Processing Conditions on Powder Particle Size and Morphology in Centrifugal Atomisation of Tin. *Powder Metall.* **2004**, *47*, 168–172. [CrossRef]

29. Li, X.P.; Yan, M.; Wang, J.Q.; Huang, H.; Kong, C.; Schaffer, G.B.; Qian, M. Non-Isothermal Crystallization Kinetics and Mechanical Properties of Al 86Ni 6Y 4.5Co 2La 1.5 Metallic Glass Powder. *J. Alloys Compd.* **2012**, *530*, 127–131. [CrossRef]

30. Lay, M.D.H.; Hill, A.J.; Saksida, P.G.; Gibson, M.A.; Bastow, T.J. 27Al NMR Measurement of Fcc Al Configurations in As-Quenched Al85Ni11Y4 Metallic Glass and Crystallization Kinetics of Al Nanocrystals. *Acta Mater.* **2012**, *60*, 79–88. [CrossRef]

31. Sahoo, K.L.; Sahu, R. Glass Transition and Crystallization of Al-Ni-La Based Metallic Glasses Studied by Temperature Modulated DSC. *J. Non. Cryst. Solids* **2013**, *365*, 33–36. [CrossRef]

32. Yule, A.J.; Dunkley, J.J. *Atomization of Melts*, 1st ed.; Oxford University Press: Oxford, UK, 1994.

33. Zhao, Y.Y. Analysis of Flow Development in Centrifugal Atomization: Part I. Film Thickness of a Fully Spreading Melt. *Model. Simul. Mat. Sci. Eng.* **2004**, *12*, 959–971. [CrossRef]

34. Whitaker, S. Forced Convection Heat Transfer Correlations for Flow in Pipes, Past Flat Plates, Single Cylinders, Single Spheres, and for Flow in Packed Beds and Tube Bundles. *AIChE J.* **1972**, *18*, 361–371. [CrossRef]

35. Wiskel, J.B.; Henein, H.; Maire, E. Solidification Study of Aluminum Alloys Using Impulse Atomization: Part I: Heat Transfer Analysis of an Atomized Droplet. *Can. Metall. Q* **2002**, *41*, 97–110. [CrossRef]

36. Ciftci, N.; Ellendt, N.; von Bargen, R.; Henein, H.; Mädler, L.; Uhlenwinkel, V. Atomization and Characterization of a Glass Forming Alloy $\{(Fe_{0.6}Co_{0.4})_{0.75}B_{0.2}Si_{0.05}\}_{96}Nb_4$. *J. Non. Cryst. Solids* **2014**, *394–395*, 36–42. [CrossRef]

37. Shiwen, H.; Yong, L.; Sheng, G. Cooling Rate Calculation of Non-Equilibrium Aluminum Alloy Powders Prepared by Gas Atomization. *Rare Met. Mater. Eng.* **2009**, *38*, 353–356.

38. Guo, S.; Liu, Y. Estimation of Critical Cooling Rates for Formation of Amorphous Alloys from Critical Sizes. *J. Non. Cryst. Solids* **2012**, *358*, 2753–2758. [CrossRef]

39. Bolfarini, C.; Srivastava, V.C. Spray Forming of Novel Materials. In *Metal Sprays and Spray Deposition*, Henein, H., Uhlenwinkel, V., Fritsching, U., Eds.; Springer: Cham, Switzerland, 2017; pp. 521–533.

40. Zheng, B.; Lin, Y.; Zhou, Y.; Lavernia, E.J. Gas Atomization of Amorphous Aluminum Powder: Part II. Experimental Investigation. *Metall. Mater. Trans. B* **2009**, *40*, 995–1004. [CrossRef]

Discussion and conclusions

5.1 Combining the atomization conditions and methods: a comparison.

During the centrifugal atomization process, it became evident that the key parameters influencing the control of cooling rate values were the gas composition within the atomization chamber and the rotational speed of the disk. In contrast, the implementation of a complementary hybrid system did not yield significant differences in terms of altering particle size or cooling rate values.

These findings were supported by a mathematical model that accounted for the temperature differences between the gas and the droplet during the centrifugal atomization process. This model provided a theoretical framework to understand the thermal behavior of the system and helped elucidate the factors influencing cooling rates. By considering the temperature gradients between the gas environment and the atomized droplets, the model facilitated the identification of optimal conditions for achieving the highest cooling rates, and with the integration of experimental results, the complex dynamics involved in centrifugal atomization was tackled.

The resulting characteristics of the powder were found to be depended upon the process parameters and atomization strategy, which influenced the cooling conditions and, consequently, the cooling rates and amorphous fractions. To consolidate the main findings, a comprehensive table (**Table 3**) has been constructed to compare results across different atomization parameters. This diagram provides a visual representation of the effectiveness of each parameter in reducing particle size, refining microstructure, increasing cooling rates, and enhancing amorphous percentage during centrifugal atomization.

In the table, symbols were used to denote whether each parameter led to an increase (↑), decrease (↓), or neutral effect (N), with the number of arrows indicating the magnitude of the effect. Notably, it has been demonstrated once more that the primary parameter governing particle size distribution is the disk speed. This observation holds true for the materials atomized during this investigation. For instance, in copper powder, there was a notable change in the median particle size from 68.1 μm when atomized at 35,000 rpm to 88.3 microns when atomized at a lower disk speed of 15,000 rpm. Similarly, in the AlNiYLa obtained powder, the median particle size decreased from 136 μm for particles atomized at 30,000 rpm to 90 μm for particles atomized at 40,000 rpm. This finding is crucial to consider, especially when aiming to produce amorphous powder, as smaller particle sizes are associated with higher cooling rates.

The external stream of gas did not exhibit a significant effect on particle size, although it did influence the grain size of the Cu powder. Specifically, an increase in the flow rate of the gas stream resulted in a decrease in grain size, although to a minimal extent. However, a factor that did have a profound impact on the microstructure of the atomized powder was the gas composition within the atomization chamber.

Table 3. *Centrifugal atomization outcome variables/imput parameters studied. The arrows demonstrate increase (↑), decrease (↓), Neutral (N) and not studied (-).*

Outcome variables/ Imput Parameters	Increasing disk velocity	Gas composition			Increasing melt superheat (K)		Flowrate: external stream of gas (L/min)		
		100%He	100%Ar	50%-50% He-Ar	250	400	0	100	200
Particle size	↓↓	N	N	N	N	N	N	N	N
Grain size	N	-	-	-	-	-	N	↓	↓
SDAS	↓	↓↓↓	N	↓↓	N	N	-	-	-
Cooling rate	↓	↑↑↑	N	↑↑	N	N	N	N	N
Amorphous fraction	↑	↑↑↑	↑	↑↑	N	N	-	-	-

80

Notably, a combination of 50% He and 50% Ar, as well as 100% He, led to a decrease in secondary dendrite arm spacing (SDAS) measurements. For instance, for particles sizes of 32.5 µm, the SDAS decreased from 2 µm to 1 µm for those atomized in an Ar and He atmosphere, respectively. Furthermore, particles produced in a He atmosphere with a size larger than 180 µm showed no indication of an amorphous structure, whereas those produced in an Ar atmosphere exhibited this limit at 75 µm. These observations highlight that He has a stronger cooling effect compared to Ar.

From **Table 3** it becomes evident that not all parameters were capable of achieving the desired cooling rates, and consequently, the desired amorphous structure. This suggests that ongoing efforts should focus on enhancing the efficiency and effectiveness of the atomization system to achieve this desired outcome. In an ideal scenario, the centrifugal atomization process would yield a high yield of fine, amorphous, and spherical particles. This may involve the further refinement of the complementary hybrid atomization system with optimizing various parameters such as gas composition, disk speed, and other operational variables to ensure the production of powders with the desired properties characteristics.

5.2 Conclusions

Al-based glass-forming alloys offer significant advantages over conventional aluminum alloys, presenting a promising route for engineering applications. However, their low glass-forming ability (GFA) has posed challenges in production, restricting their use to techniques capable of providing rapid cooling rates. Atomization of these alloys is particularly challenging, as it may lead to crystallization due to limitations in cooling rates and GFA. While production of Al-based metallic glasses has been produced using other atomization processes such as gas and water atomization, centrifugal atomization presents several distinct advantages.

This PhD thesis has contributed novel process guidelines for the centrifugal atomization of Al-based glass-forming alloys. To address this, detailed studies were conducted on the centrifugal atomization process with the aim of proving and developing the production of Al-based glass-forming alloys, with the potential for extension to other alloys in the future. To achieve this goal, it was imperative to thoroughly characterize the centrifugal atomizer equipment used in this PhD thesis, particularly in terms of its capacity to achieve desired cooling rates. For this purpose, various parameters and strategies of atomization were investigated, including the development of a complementary hybrid system, increasing the melt superheat temperature, the variation of the gas composition, and increasing the disk speed of atomization.

Hybrid atomization process

In Paper I, the impact of an external stream of gas at the periphery of the disk on the production of Cu powder was thoroughly examined. The primary findings revealed that the particle grain size exhibited a tendency to decrease with the increase in the flowrates of the

external gas stream. Notably, this effect was more pronounced at lower speeds of atomization, attributable to the additional velocity component introduced by the gas stream.

However, despite the introduction of this complementary system, it was anticipated that a decrease in particle size distribution compared to the conventional centrifugal atomization method would be observed. The underlying hypothesis was that the gas stream would serve to further break the droplets immediately after their ejection from the disk. Yet, it was observed that a higher flowrate of gas was necessary for this effect to manifest. Flowrates ranging from 100 to 200 L/min proved to be only sufficient to reduce the grain size within the particle, rather than causing droplet fragmentation itself.

Consequently, the hybrid complementary system was excluded from subsequent atomization approaches aimed at enhancing the cooling rate of the atomized particles. Instead, the focus shifted towards characterizing the traditional centrifugal atomization process in terms of cooling rates, both theoretically and experimentally.

Increasing melt superheat

The impact of an increased melt superheat temperature on the characteristics of the resulting Al-Cu powder was investigated in Paper II. It is widely acknowledged that elevating the melt superheat temperature leads to an increased temperature gradient in the melt, which can deactivate impurities, dissolve intermetallic remnants, elevate the diffusion coefficient, and reduce undercooling [156]. However, varying the melt superheat temperature is a complex process, as elevated temperatures may induce chemical reactions with the crucible, potentially triggering crystallization.

In paper II, the results indicated that increasing the melt superheat temperature from 200 K to 450 K did not yield significant outcomes. Both particle size and particle size distribution remained unaffected by the melt superheat temperature, as well as no changes on the cooling rate values were found. Consequently, it can be said that the melt superheat does not influence the cooling history of the particles. However, it remains a crucial parameter to ensure proper melting of the starting materials and prevent potential melt solidification on the atomization disk.

Effect of the gas composition

In Papers II and III, both Al-Cu alloy and AlNiYLa alloy were subjected to atomization in both argon (Ar) and helium (He) atmospheres. Prior research on gas atomization has demonstrated that particles atomized in a helium atmosphere can be sufficiently cooled to achieve the same amorphous fraction as particles twice their size atomized in a nitrogen or argon atmosphere [20].

Paper III further elucidated this point by revealing in a He atmosphere, the amorphous fraction value remained relatively stable, exhibiting a slight decrease as the droplet diameter increased in particles up to 125 µm in size. However, beyond this threshold, the amorphous fraction decreased rapidly. Conversely, in a He-Ar atmosphere, this abrupt decrease occurred at

particle sizes around 90 μm, while in an Ar atmosphere, it was observed at approximately 40 μm. These findings underscore the superior cooling effect of helium compared to argon.

While helium is approximately ten times more expensive than argon from an economic standpoint, centrifugal atomization presents a distinct advantage in terms of gas consumption. This is due to the fact that helium is only used to fill the atomization chamber, while the atomization process itself is carried out by the atomization disk. Therefore, employing helium in the centrifugal atomization process for producing amorphous powder emerges as a promising approach from an economic perspective.

Effect of the disk speed

In both papers I and III, an exhaustive examination was conducted on the impact of disk speed, ranging from 15,000 rpm to 40,000 rpm. It is widely acknowledged within the realm of centrifugal atomization that disk speed stands as the primary determinant governing the particle size of the atomized droplets. However, while disk speed exerts a pronounced influence on particle size, its effect on microstructure appears comparatively subtle. This minor effect was exposed in paper III, where it was observed that variations in disk speed resulted in only marginal alterations in microstructural features for the same particle size. Specifically, a minor reduction in the amorphous fraction was seen among particles atomized at 30,000 rpm compared to those atomized at 40,000 rpm. It became evident that variables such as particle diameter and gas atmosphere exerted a more substantial impact on the cooling rate of the particles, thereby producing significant modifications in microstructural characteristics.

Theoretical heat transfer model

In Paper II, the significance of evaluating the thermal properties of the gas at specific temperatures became evident in the quest for achieving the most accurate cooling rate values possible. The crucial aspect lies in the understanding that even a difference of one order of magnitude in the cooling rate values can delineate the boundary between obtaining an amorphous or crystalline structure.

When comparing the theoretical and experimental calculations of cooling rates, the superiority of evaluating the thermal conductivity k_g using the Whitaker correlation at the film temperature T_f over evaluating it at the ambient temperature T_A remains uncertain. For smaller particle sizes, correlating the properties of the gas at ambient temperature seems to yield better results when comparing both theoretical and experimental approaches. However, as particle size increases, evaluating the thermal conductivity k_g at the film temperature T_f tends to offer more accurate outcomes. Nevertheless, it is acknowledged that utilizing k_g at ambient temperatures for calculating the convective heat transfer coefficient h_c may introduce errors in systems with higher temperatures.

In this regard, it is advisable to address the evaluation of thermophysical properties of the gas for the centrifugal atomization process using Whitaker's correlation. This approach accounts for temperature variations by considering the ratio of dynamic viscosities at the droplet surface

temperature T_d and the ambient temperature T_A, while also evaluating the thermal conductivity of the gas k_g from the Nusselt number at the film temperature T_f.

Overall, the process and cooling conditions of centrifugal atomization can be summarized as depicted in **Figure 18**. The atomization temperature is dependent upon factors such as the melt temperature, melt superheat temperature, and the heat loss from the melt stream passing through the nozzle of the crucible. Moreover, the thermal history of the droplets is intricately tied type of gas in the atomization chamber, to the distribution of the melt in the disk and the mode of droplet disintegration, which are governed by variables such as the disk material, disk geometry, and disk velocity. Ultimately, these factors collectively determine the characteristics of the obtained powder.

Melt feed
- Alloy selection (viscosity, Surface tension, density, etc.)
- Melt temperature and superheat temperature
- Nozzle diameter
- Melt flowrate

Atomization process
- Type of gas
- Nozzle diameter
- Disk material, disk geometry and disk velocity

Atomized particles
- Particle size, particle size distribution, shape, and surface roughness
- Particle porosity
- Impurities (oxygen, etc.)
- Microstructure: crystalline, partially-amorphous, and amorphous

Figure 18. Process conditions during molten metal centrifugal atomization.

The central research question aimed to ascertain whether the centrifugal atomization process could attain the necessary cooling rates for the production of metallic glasses powder. Through rigorous investigation, it was observed that achieving such rates is indeed feasible under specific conditions and atomization parameters. By optimizing these variables, it became evident that it is possible to significantly enhance cooling rates, consequently leading to a higher amorphous fraction in the synthesized powder. These findings underscore the potential of centrifugal atomization as a viable and efficient method for producing metallic glasses powders with desired amorphous characteristics, paving the way for advancements in materials science and engineering applications.

5.3 Outlook

High rotation speeds

Despite recognizing the significant role of the gas type in amorphous powder production, it has become evident that the resulting particle size is distinctly governed by the disk speed. With increasing disk speed, there is a corresponding decrease in particle size. As observed, smaller particle sizes lead to a higher fraction of amorphous powder, which is desirable for processes like additive manufacturing. Consequently, a crucial question arises: What is the maximum velocity that the centrifugal atomization disk can achieve to consistently produce smaller particle sizes? Theoretically, this velocity can be calculated as depicted in Figure 2.7, which illustrates that with increasing disk velocity, it becomes progressively more challenging to attain smaller particle sizes.

Moreover, achieving high rotation speeds in a centrifugal atomizer can often be challenging due to the scarcity of robust, vibration-free high-speed motors. In the USA, Europe, and Japan, numerous producers utilize spinning disk methods with speeds ranging from 30,000 to 60,000 rpm for low melting point metals [157]. Another centrifugal atomization design tailored for superalloy powder production has been developed to address challenges associated with handling high melting and aggressive alloys. This process, called Rapid Solidification Rate Process (RSR) involves a high-speed water-cooled rotating disk, reaching speeds of up to 50,000 rpm, enabling cooling rates of up to 10^5 K/s [158]. A curtain of helium jets is directed towards the atomized droplets. However, challenges persist, as there are reported issues with skull formation leading to out-of-balance forces in the disk.

As can be seen, increasing the speed of the disk in centrifugal atomization processes can lead to significant challenges, and up to date it has several limitations. On the one hand, as the rotational speed rises, the heightened force can lead to imbalances that can cause mechanical damage to the system itself, posing risks to its stability. Achieving a vibration free high-speed motor requires precise engineering and design considerations that are yet to be fully realized.

On the other hand, when atomizing high-melting-point metal alloys, the challenge of cooling the disk becomes apparent. The disk requires cooling to mitigate thermal shock that could disrupt its proper function. However, cooling the disk also increases the skull formation, which can disrupt the atomization process. Consequently, addressing these issues is not a straightforward task, and further technical development is still necessary.

Including fluxing agents

Some strategies to enhance the amorphous fraction obtained could involve the utilization of fluxing agents to improve the glass-forming ability of certain alloys. For instance, in the case of the glass-forming alloy $Fe_{40}Ni_{40}P_{14}B_6$, it was observed that the critical cooling rate decreased by three orders of magnitude when fluxed with B_2O_3 [159]. This reduction occurs because impurities can be sequestered in the fluxing agent if the major constituent elements in the melt exhibit a lower affinity to oxygen compared to boron.

Additionally, salts have emerged as another area of investigation [160]. Typically, salts increase the wettability of the melt, thereby enhancing the separation of oxide inclusions. For example, in Al-based glass-forming alloys, chloride fluxing agents have demonstrated the capability to float on the surface of the melt and subsequently absorb oxide impurities through agglomeration [161].

It is important to take into account that during the centrifugal atomization process employed in this PhD thesis, the elements and alloys required to prepare the material for atomization are melted in a crucible using induction melting at the same time as the atomization process is conducted. This means that the alloy is not pre-prepared and then remelted. Consequently, if a fluxing agent is to be used to separate oxide impurities from the melt, the alloy would need to be prepared beforehand which introduces an additional step to the current process implementation.

Further experiments extended to other materials

Despite the absence of a comprehensive and universally applicable criterion for selecting compositions with high forming ability, extensive knowledge exists regarding various compositions for producing metallic glasses [9]. However, it is noteworthy that atomization techniques have predominantly focused on applications currently in development, such as Al and Fe alloys. In the realm of Fe alloys, both water and gas atomization techniques have been extensively studied, yielding promising results [10,16,17,162].

Further exploration into the centrifugal atomization of Fe glass-forming alloys is highly recommended, given their expanding applications and potential benefits [163]. One of the primary challenges associated with centrifugal atomizing Fe alloys is addressing their high melting point when they come into contact with the atomization disk. This presents a risk of thermal shock to the disk, which could compromise its integrity. Therefore, the implementation of a refrigeration system on the disk is required to effectively manage the process and ensure successful atomization without causing damage to the entire disk-motor system. However, overcoming this issue and successfully producing Fe glass-forming alloys with the prominence they exhibit today would be highly beneficial for various industrial applications [164].

Bibliography

[1]   D.C. Hofmann, J.Y. Suh, A. Wiest, G. Duan, M.L. Lind, M.D. Demetriou, W.L. Johnson, Designing metallic glass matrix composites with high toughness and tensile ductility, Nature 451 (2008) 1085–1089. https://doi.org/10.1038/nature06598.

[2]   M.D. Demetriou, M.E. Launey, G. Garrett, J.P. Schramm, D.C. Hofmann, W.L. Johnson, R.O. Ritchie, A damage-tolerant glass, Nat Mater 10 (2011) 123–128. https://doi.org/10.1038/nmat2930.

[3]   M. Chen, A brief overview of bulk metallic glasses, NPG Asia Mater 3 (2011) 82–90. https://doi.org/10.1038/asiamat.2011.30.

[4]   W.L. Johnson, J. Plummer, Is metallic glass poised to come of age?, Nat Mater 14 (2015) 553–555. https://doi.org/10.1038/nmat4297.

[5]   Nature Materials Editorial, Crystallizing glassy issues, Nat Mater 14 (2015) 541. https://doi.org/10.1038/nmat4319.

[6]   D.B. Miracle, A physical model for metallic glass structures: An introduction and update, JOM 64 (2012) 846–855. https://doi.org/10.1007/s11837-012-0359-4.

[7]   D. M. Minić, M. M. Vasić, Introductory Chapter: Metallic Glasses, in: Metallic Glasses, IntechOpen, 2020. https://doi.org/10.5772/intechopen.88891.

[8]   C. Suryanarayana, A. Inoue, Metallic Glasses, Ullmann's Encyclopedia of Industrial Chemistry (2012). https://doi.org/10.1002/14356007.a16_335.pub2.

[9]   C. Bolfarini, V.C. Srivastava, Spray Forming of Novel Materials, in: H. Henein, V. Uhlenwinkel, U. Fritsching (Eds.), Metal Sprays and Spray Deposition, 1st ed., Springer, Gewerbestrasse, 2017: pp. 521–533.

[10]   C. Alvarez, Novel amorphous and nanocrystalline Fe-based soft magnetic powders produced by gas atomisation, Universidad de Navarra, 2020. https://dadun.unav.edu/handle/10171/59500 (accessed April 15, 2024).

[11]   Z. Baolong, Synthesis and behaviour of metallic glasses via gas atomization and laser deposition, University of California, Davis, 2006.

[12]   B. Zheng, Y. Lin, Y. Zhou, E.J. Lavernia, Gas atomization of amorphous aluminum: Part I. thermal behavior calculations, Metallurgical and Materials Transactions B: Process Metallurgy and Materials Processing Science 40 (2009) 768–778. https://doi.org/10.1007/s11663-009-9276-5.

[13]   B. Zheng, Y. Lin, Y. Zhou, E.J. Lavernia, Gas atomization of amorphous aluminum powder: Part II. experimental investigation, Metallurgical and Materials Transactions B: Process Metallurgy and Materials Processing Science 40 (2009) 995–1004. https://doi.org/10.1007/s11663-009-9277-4.

[14]   Y. Liu, Z. Liu, S. Guo, Y. Du, B. Huang, J. Huang, S. Chen, F. Liu, Amorphous and nanocrystalline Al82Ni10Y8 alloy powder prepared by gas atomization, in: Intermetallics (Barking), 2005: pp. 393–398. https://doi.org/10.1016/j.intermet.2004.07.026.

[15]   P. Dong, W.L. Hou, X.C. Chang, M.X. Quan, J.Q. Wang, Amorphous and nanostructured Al85Ni5Y6Co2Fe2 powder prepared by nitrogen gas-atomization, J Alloys Compd 436 (2007) 118–123. https://doi.org/10.1016/j.jallcom.2006.07.032.

[16]   Y. Liu, S. Niu, F. Li, Y. Zhu, Y. He, Preparation of amorphous Fe-based magnetic powder by water atomization, Powder Technol 213 (2011) 36–40. https://doi.org/10.1016/j.powtec.2011.06.026.

[17]   T. Zhao, C. Chen, X.J. Wu, C. Zhang, A.A. Volinsky, J. Hao, FeSiBCrC amorphous magnetic powder fabricated by gas-water combined atomization, J Alloys Compd 857 (2021) 157991. https://doi.org/10.1016/j.jallcom.2020.157991.

[18]   K.R. Cardoso, A. García Escorial, M. Lieblich, W.J. Botta, Amorphous and nanostructured Al-Fe-Nd powders obtained by gas atomization, (2001). https://doi.org/https://doi.org/10.1016/S0921-5093(01)01197-2.

[19]   D.F. Produktionstechnik, N. Ciftci, Cooling strategies for the atomization of glass-forming alloys, Universitat Bremen, 2020.

[20]   N. Ciftci, N. Ellendt, R. Von Bargen, H. Henein, L. Mädler, V. Uhlenwinkel, Atomization and characterization of a glass forming alloy {(Fe 0.6Co0.4)0.75B0.2Si 0.05}96Nb4, J Non Cryst Solids 394–395 (2014) 36–42. https://doi.org/10.1016/j.jnoncrysol.2014.03.023.

[21]   F. Chu, K. Zhang, H. Shen, M. Liu, W. Huang, X. Zhang, E. Liang, Z. Zhou, L. Lei, J. Hou, A. Huang, Influence of satellite and agglomeration of powder on the processability of AlSi10Mg powder in Laser Powder Bed Fusion, Journal of Materials Research and Technology 11 (2021) 2059–2073. https://doi.org/10.1016/j.jmrt.2021.02.015.

[22]   A.-A. Bogno, H. Henein, V. Uhlenwinkel, E. Gärtner, Single Fluid Atomization Fundamentals, in: H. Henein, V. Uhlenwinkel, U. Fritsching (Eds.), Metal Sprays and Spray Deposition, 1st ed., Springer, 2017: pp. 9–46.

[23]   J.J. Dunkley, D. Aderhold, Centrifugal atomization of metal powders, Sheffield, 2007.

[24]   S. Öztürk, F. Arslan, B. Öztürk, Effect of production parameters on cooling rates of AA2014 alloy powders produced by water jet cooled, rotating disc atomisation, Powder Metallurgy 46 (2003) 342–348. https://doi.org/10.1179/003258903225008599.

[25]   C. Suryanarayana, A. Inoue, Bulk Metallic Glasses, 1st ed., 2010.

[26]   H.S. Chen, J.T. Krause, E. Coleman, Elastic constants, harness and their implications to flow properties of metallic glasses, J Non Cryst Solids 18 (1975) 157–171. https://doi.org/https://doi.org/10.1016/0022-3093(75)90018-6.

[27]   H.S. Chent, Thermodynamic considerations on the formation and stability of metallic glasses, Acta Metallurgica 2 (1974) 1505–1511. https://doi.org/https://doi.org/10.1016/0001-6160(74)90112-6.

[28]   W. klement, R. Willens, P. Duwez, Non-crystalline structure in solidified gold-silicon alloys, Nature (1960) 869–870. https://doi.org/https://doi.org/10.1038/187869b0.

[29]   X.H. Lin, W.L. Johnson, Formation of Ti-Zr-Cu-Ni bulk metallic glasses, J Appl Phys 78 (1995) 6514–6519. https://doi.org/10.1063/1.360537.

[30] A. Inoue, N. Matsumoto, T. Masumoto, Al-Ni-Y-Co Amorphous alloys with high mechanical strength wide supercooled, Mater Trans 31 (1990) 493–500. https://doi.org/https://doi.org/10.2320/matertrans1989.31.493.

[31] A. Inoue, High strength bulk amorphous alloys with low critical cooling rates (overview), Mater Trans 36 (1995) 866–875. https://doi.org/https://doi.org/10.2320/matertrans1989.36.866.

[32] A. Inoue, Stabilization of metallic supercooled liquid and bulk amorphous alloys, Acta Mater 48 (2000) 279–306. https://doi.org/https://doi.org/10.1016/S1359-6454(99)00300-6.

[33] A. Peker, W.L. Johnson, A highly processable metallic glass: Zr41.2Ti 13.8Cu12.5Ni10.0Be22.5, Appl Phys Lett 63 (1993) 2342–2344. https://doi.org/10.1063/1.110520.

[34] H.X. Li, Z.C. Lu, S.L. Wang, Y. Wu, Z.P. Lu, Fe-based bulk metallic glasses: Glass formation, fabrication, properties and applications, Prog Mater Sci 103 (2019) 235–318. https://doi.org/10.1016/j.pmatsci.2019.01.003.

[35] S. Korkmaz, A. Kariper, Glass formation, production and superior properties of Zr-based thin film metallic glasses (TFMGs): A status review, J Non Cryst Solids 527 (2020). https://doi.org/10.1016/j.jnoncrysol.2019.119753.

[36] C. Fan, X. Yue, A. Inoue, C.-T. Liu, X. Shen, P.K. Liaw, Recent Topics on the Structure and Crystallization of Al-based Glassy Alloys, Materials Research 22 (2019) 1–15. https://doi.org/10.1590/1980-5373-mr-2018-0619.

[37] T.W. Wilson, Processing , Structure , and Properties of Amorphous Aluminum Alloys, University of Tennessee - Knoxville, 2008.

[38] R. Angers, R. Tremblay, L. Desrosiers, D. Dubé, Rotating disk coatings for centrifugal atomization of aluminium and magnesium alloys, Canadian Metallurgical Quarterly 35 (1996) 291–297. https://doi.org/10.1179/cmq.1996.35.3.291.

[39] S. Öztürk, F. Arslan, B. Öztürk, Effect of process parameters on production of metal powders by water jet cooled rotating disc atomisation, Powder Metallurgy 48 (2005) 163–170. https://doi.org/10.1179/003258905X37738.

[40] J. Dantzig, M. Rappaz, Solidification, 1st ed., Switzerland, 2009.

[41] M.D. Ediger, S.R. Nagel, Supercooled liquids and glasses, (1996) 13200–13212. https://doi.org/https://doi.org/10.1021/jp953538d.

[42] Calorimetría Diferencial de Barrido, (n.d.). https://www.pslc.ws/spanish/dsc.htm (accessed October 24, 2023).

[43] J.W.P. Schmelzer, T. V. Tropin, Glass transition, crystallization of glass-forming melts, and entropy, Entropy 20 (2018). https://doi.org/10.3390/e20020103.

[44] Q. Chen, J. Shen, D. Zhang, H. Fan, J. Sun, D.G. McCartney, A new criterion for evaluating the glass-forming ability of bulk metallic glasses, Materials Science and Engineering: A 433 (2006) 155–160. https://doi.org/10.1016/j.msea.2006.06.053.

[45]   J. Henao, A. Concustell, I. G.Cano, S. Dosta, N. Cinca, J.M. Guilemany, T. Suhonen, Novel Al-based metallic glass coatings by Cold Gas Spray, Mater Des 94 (2016) 253–261. https://doi.org/10.1016/j.matdes.2016.01.040.

[46]   M.E. Blodgett, T. Egami, Z. Nussinov, K.F. Kelton, Proposal for universality in the viscosity of metallic liquids, Sci Rep 5 (2015). https://doi.org/10.1038/srep13837.

[47]   L. Cormier, Nucleation in Glasses – New Experimental Findings and Recent Theories, Procedia Materials Science 7 (2014) 60–71. https://doi.org/10.1016/j.mspro.2014.10.009.

[48]   N. Van Steenberge, Study of structural changes in Zr-based bulk metallic glasses upon annealing and deformation treatments, Universitat Autònoma de Barcelona, 2008.

[49]   M.C. Weinberg, B.J. Zelinski, D.R. Uhlmann, E.D. Zanotto, Critical cooling calculations for glass formation, J Non Cryst Solids 123 (1990) 90–96. https://doi.org/https://doi.org/10.1016/0022-3093(90)90776-I.

[50]   D.R. Uglmann, P.I.K. Onorato, A simplified model for glass formation, in: G.W. Scherer (Ed.), Proceedings of Lunar and Planetary Science , New York, 1979: pp. 375–381.

[51]   D.R. Uhlmann, A kinetic treatment of glass formation, J Non Cryst Solids 7 (1972) 337–348. https://doi.org/https://doi.org/10.1016/0022-3093(72)90269-4.

[52]   P.I.K. Onorato, D.R. Uhlmann, Nucleating heterogeneities and glass formation, J Non Cryst Solids 22 (1976) 367–378. https://doi.org/https://doi.org/10.1016/0022-3093(76)90066-1.

[53]   M.C. Weinberg, D.R. Uhlmann, E.D. Zanotto, "Nose Method" of Calculating Critical Cooling Rates for Glass Formation, J. Am. Ceram. Soc 72 (1989) 2054–58. https://doi.org/https://doi.org/10.1111/j.1151-2916.1989.tb06030.x.

[54]   Z. Long, G. Xie, H. Wei, X. Su, J. Peng, P. Zhang, A. Inoue, On the new criterion to assess the glass-forming ability of metallic alloys, Materials Science and Engineering: A 509 (2009) 23–30. https://doi.org/10.1016/j.msea.2009.01.063.

[55]   C. Zhang, D. Ouyang, S. Pauly, L. Liu, 3D printing of bulk metallic glasses, Materials Science and Engineering R: Reports 145 (2021). https://doi.org/10.1016/j.mser.2021.100625.

[56]   A. Inoue, High strenght bulk amorphous alloys with low critical cooling rates (overview), Mater Trans 36 (1995) 866–875. https://doi.org/https://doi.org/10.2320/matertrans1989.36.866.

[57]   Y. Yokoyama, E. Mund, A. Inoue, L. Schultz, Production of Zr55Cu30Ni5Al10 glassy alloy rod of 30 mm in diameter by a cap-cast technique, in: Mater Trans, 2007: pp. 3190–3192. https://doi.org/10.2320/matertrans.MRP2007164.

[58]   P. Duwez, Metallic Glasses-Historical Background, in: Glassy Metals I. Topics in Applied Physics, 1981. https://doi.org/https://doi.org/10.1007/3540104402_2.

[59]   D. Turnbull, Under What Conditions Can A Glass Be Formed?, Contemp Phys 10 (1969) 473–488. https://doi.org/10.1080/00107516908204405.

[60]   J.H. Na, M.D. Demetriou, M. Floyd, A. Hoff, G.R. Garrett, W.L. Johnson, Compositional landscape for glass formation in metal alloys, Proc Natl Acad Sci U S A 111 (2014) 9031–9036. https://doi.org/10.1073/pnas.1407780111.

[61]   P. Sungkhaphaitoon, S. Wisutmethangoon, T. Plookphol, Influence of Process Parameters on Zinc Powder Produced by Centrifugal Atomisation, 20 (2017) 718–724. https://doi.org/https://doi.org/10.1590/1980-5373-MR-2015-0674.

[62]   A.J. Yule, J.J. Dunkley, Atomization of melts, 1st ed., Oxford University Press, Oxford, 1994.

[63]   Y.Y. Zhao, Analysis of flow development in centrifugal atomization: Part II. Disintegration of a non-fully spreading melt, Model Simul Mat Sci Eng 12 (2004) 973–983. https://doi.org/10.1088/0965-0393/12/5/014.

[64]   Y.Y. Zhao, Analysis of flow development in centrifugal atomization: Part I. Film thickness of a fully spreading melt, Model Simul Mat Sci Eng 12 (2004) 959–971. https://doi.org/10.1088/0965-0393/12/5/013.

[65]   S.A. Cegarra Salges, J. Pijuan, R. Hernández, M.D. Riera, Effect of processing parameters on copper powder produced by novel hybrid atomisation technique, Powder Metallurgy 0 (2020) 1–7. https://doi.org/10.1080/00325899.2020.1724431.

[66]   V.T. Mantripragada, K. Kumar, P. Kumar, S. Sarkar, Modeling of Powder Production During Centrifugal Atomization, Journal of Sustainable Metallurgy 7 (2021) 620–629. https://doi.org/10.1007/s40831-021-00370-2.

[67]   J.O. Hinze, H. Milborn, Atomization of liquids by means of rotating cups, J Appl Mech 17 (1950) 145–153. https://doi.org/https://doi.org/10.1115/1.4010093.

[68]   L. Tian, I. Anderson, T. Riedemann, A. Russell, Production of fine calcium powders by centrifugal atomization with rotating quench bath, Powder Technol 308 (2017) 84–93. https://doi.org/10.1016/j.powtec.2016.12.011.

[69]   M. Ahmed, M.S. Youssef, Characteristics of mean droplet size produced by spinning disk atomizers, Journal of Fluids Engineering, Transactions of the ASME 134 (2012). https://doi.org/10.1115/1.4006819.

[70]   P. Kumar, S. Sarkar, Experimental investigation of liquid disintegration on slotted disc in centrifugal atomization process, Chemical Engineering Research and Design 145 (2019) 76–84. https://doi.org/10.1016/j.cherd.2019.02.039.

[71]   P. Eisenklam, On ligament formation from spinning discs and cups, Chem Eng Sci 19 (1964) 693–694. https://doi.org/10.1016/0009-2509(64)85056-9.

[72]   R.P. Fraser, N. Dombrowski, J.H. Routley, The filming of liquids by spinning cups, Chem Eng Sci 18 (1963) 323–337. https://doi.org/https://doi.org/10.1016/0009-2509(63)80026-3.

[73]   L.M. Boize, ; N Dombrowskit, The Atomization Characteristics of a Spinning Disc Ultra-low Volume Applicator, J. Ugric. Engng Res 21 (1976) 87–99. https://doi.org/https://doi.org/10.1016/0021-8634(76)90101-3.

[74] A. Frost, Rotary Atomization in the Ligament Formation Mode, Journal of Agricultural Engineering Research 26 (1981) 63–78. https://doi.org/10.1016/0021-8634(81)90127-X.

[75] Y. Kawase, A. De, Ligament type disintegration of non-newtonian fluid in spinning disk atomization, Journal of Non-Newtoniari Fluid Mechanics 10 (1982) 367–371. https://doi.org/https://doi.org/10.1016/0377-0257(82)80010-4.

[76] D. Wang, X. Ling, H. Peng, Z. Cui, X. Yang, Experimental Investigation of Ligament Formation Dynamics of Thin Viscous Liquid Film at Spinning Disk Edge, Ind Eng Chem Res 55 (2016) 9267–9275. https://doi.org/10.1021/acs.iecr.6b01428.

[77] N. Dombrowski, T.L. Lloyd, The spread of liquid on a rotating vane, Chem Eng Sci 27 (1972) 1003–1012. https://doi.org/https://doi.org/10.1016/0009-2509(72)80015-0.

[78] N. Dombrowski, W.R. Johns, The aerodynamic instability and disintegration of viscous liquid sheets, Chem Eng Sci 18 (1963) 203–214. https://doi.org/https://doi.org/10.1016/0009-2509(63)85005-8.

[79] T. Kamiya, A. Kayano, Film-type disintegration by rotating disk, Journal of Chemical Engineering of Japan 5 (1972) 76–83. https://doi.org/10.1016/j.ces.2014.04.043.

[80] J. Liu, Q. Yu, Q. Guo, Experimental investigation of liquid disintegration by rotary cups, Chem Eng Sci 73 (2012) 44–50. https://doi.org/10.1016/j.ces.2012.01.010.

[81] J.W. Xie, Y.Y. Zhao, J.J. Dunkley, Effects of processing conditions on powder particle size and morphology in centrifugal atomisation of tin, Powder Metallurgy 47 (2004) 168–172. https://doi.org/10.1179/003258904225015482.

[82] R. Dhirhi, K. Prasad, A.K. Shukla, S. Sarkar, T. Renganathan, S. Pushpavanam, M. Kaza, Experimental study of rotating dry slag granulation unit: Operating regimes, particle size analysis and scale up, Appl Therm Eng 107 (2016) 898–906. https://doi.org/10.1016/j.applthermaleng.2016.07.049.

[83] F. Arslan, Production of rapidly solidified metal powders by water cooled rotating disc atomisation, 2001. https://doi.org/https://doi.org/10.1179/003258901666220.

[84] H. Li, X. Deng, Prediction of powder particle size during centrifugal atomisation using a rotating disk, Sci Technol Adv Mater 8 (2007) 264–270. https://doi.org/10.1016/j.stam.2007.03.001.

[85] L.P. Zhang, Y.Y. Zhao, Particle size distribution of tin powder produced by centrifugal atomisation using rotating cups, Powder Technol 318 (2017) 62–67. https://doi.org/10.1016/j.powtec.2017.05.038.

[86] T. Plookphol, S. Wisutmethangoon, S. Gonsrang, Influence of process parameters on SAC305 lead-free solder powder produced by centrifugal atomization, Powder Technol 214 (2011) 506–512. https://doi.org/10.1016/j.powtec.2011.09.015.

[87] S. Gonsrang, P. Thawathai, S. Wisutmethangoon, Design and development of centrifugal atomizer, in: 4th International Conference on Engineering Technologies - ICET 2009, 2009: pp. 611–617.

[88] A.J. Hewitt, Droplet size spectra produced by air-assited atomizers, J. Aerosol Sci 24 (1993) 155–162. https://doi.org/https://doi.org/10.1016/0021-8502(93)90055-E.

[89] A.D. Hewitt, Droplet size spectra produced by the X15 stacked spinning-disc atomizer of the Ulvamast Mark II sprayer, Crop Protection 11 (1992) 221–224. https://doi.org/https://doi.org/10.1016/0261-2194(92)90040-C.

[90] H. Peng, X. Shan, X. Ling, D. Wang, J. Li, Ligament-type granulation of molten slag in different rotary disk configurations, Appl Therm Eng 128 (2018) 1565–1578. https://doi.org/10.1016/j.applthermaleng.2017.09.132.

[91] P. Sungkhaphaitoon, W. Likhidkan, S. Kitjaidiaw, S. Wisutmethangoon, T. Plookphol, Effect of atomizer disc geometry on zinc metal powder production by centrifugal atomization, in: Applied Mechanics and Materials, 2013: pp. 232–236. https://doi.org/10.4028/www.scientific.net/AMM.271-272.232.

[92] M. Ahmed, M.S. Youssef, Influence of spinning cup and disk atomizer configurations on droplet size and velocity characteristics, Chem Eng Sci 107 (2014) 149–157. https://doi.org/10.1016/j.ces.2013.12.004.

[93] J.J. Wu, H. Wang, X. Zhu, Q. Liao, K. Li, Cold experiment of slag centrifugal granulation by rotary atomizer: Effect of atomizer configuration, Appl Therm Eng 111 (2017) 1557–1564. https://doi.org/10.1016/j.applthermaleng.2016.08.039.

[94] T. Misuochi, T. Akiyama, Cold Experiments of Rotary Vaned-disks and Wheels for Slag Atomization, Iron and Steel Institute of Japan International 43 (2003) 1469–1471. https://doi.org/https://doi.org/10.2355/isijinternational.43.1469.

[95] H. Peng, X. Shan, X. Ling, D. Wang, J. Li, Analogue experimental investigation on ligament granulation of molten slag in various rotary disk configurations for waste energy recovery, Results Phys 11 (2018) 385–393. https://doi.org/10.1016/j.rinp.2018.09.037.

[96] D. Wang, X. Ling, H. Peng, Z. Cui, X. Yang, High-temperature analogy experimental investigation on dry granulating characteristic of rotating disk for waste heat utilization of molten slag, Appl Therm Eng 125 (2017) 846–855. https://doi.org/10.1016/j.applthermaleng.2017.07.075.

[97] Y.Y. Zhao, M.H. Jacobs, A.L. Dowson, Liquid Flow on a Rotating Disk Prior to Centrifugal Atomization and Spray Deposition, Metallurgical and Materials Transactions B 29 (1998) 1357–1369. https://doi.org/https://doi.org/10.1007/s11663-998-0059-1.

[98] K.H. Ho, Y.Y. Zhao, Modelling thermal development of liquid metal flow on rotating disc in centrifugal atomisation, Materials Science and Engineering: A 365 (2004) 336–340. https://doi.org/10.1016/j.msea.2003.09.044.

[99] M.G. Osborne, Centrifugal Atomization of Lanthanide Materials for Cryogenic Coolers, Ames Labooratory, n.d.

[100] P. Sungkhaphaitoon, T. Plookphol, S. Wisutmethangoon, Design and Development of a Centrifugal Atomizer for Producing Zinc Metal Powder, International Journal of Applied Physics and Mathematics 2 (2012) 77–82. https://doi.org/10.7763/ijapm.2012.v2.58.

[101] S.A. Cegarra, J. Pijuan, M.D. Riera, Cooling Rate Modeling and Evaluation during Centrifugal Atomization Process, Journal of Manufacturing and Materials Processing 7 (2023) 112. https://doi.org/10.3390/jmmp7030112.

[102] J. Pijuan, S.A. Cegarra, S. Dosta, V. Albaladejo-Fuentes, M.D. Riera, Centrifugal Atomization of Glass-Forming Alloy Al86Ni8Y4.5La1.5, Materials 15 (2022). https://doi.org/10.3390/ma15228159.

[103] Y.Y. Zhao, A.L. Dowson, M.H. Jacobs, Modelling of liquid flow after a hydraulic jump on a rotating disk prior to centrifugal atomization *, 2000. http://iopscience.iop.org/0965-0393/8/1/305.

[104] R. Mehrabian, ed., Rapid solidification processing, in: Rapid Solidification Processing, Maryland, 1982.

[105] E.J. Lavernia, T. Srivatsan, The rapid solidification processing of materials : science, principles, technology, advances and applications, Journal of Material Science (2010) 287–325. https://doi.org/10.1007/s10853-009-3995-5.

[106] D.A. Porter, K.E. Easterling, M.Y. Sherif, Phase Transformations in Metals and Alloys, Third edition, CRC Press Taylor & Fransis Group, Boca Ratón, 2009.

[107] P. Delshad Khatibi, H. Henein, U. Fritsching, In-Situ, Real Time Diagnostics in the Spray Forming Process, in: H. Henein, U. Fritsching, V. Uhlenwinkel (Eds.), Metal Sprays and Spray Deposition, Springer, 2017: pp. 1–407. https://doi.org/10.1007/978-3-319-52689-8_6.

[108] P.D. Khatibi, A. Ilbagi, D. Beinker, H. Henein, In-situ characterization of droplets during free fall in the drop tube-impulse system, in: J Phys Conf Ser, Institute of Physics Publishing, 2011. https://doi.org/10.1088/1742-6596/327/1/012014.

[109] M. Krauss, D. Bergmann, U. Fritsching, K. Bauckhage, In-situ particle temperature, velocity and size measurements in the spray forming process, Materials Science and Engineering 326 (2002) 154–164. https://doi.org/10.1016/S0921-5093(01)01420-4 Authors:

[110] R.M. Srivastava, J. Eckert, W. Löser, B.K. Dhindaw, L. Schultz, Cooling rate evaluation for bulk amorphous alloys from eutectic microstructures in casting processes, Mater Trans 43 (2002) 1670–1675. https://doi.org/10.2320/matertrans.43.1670.

[111] A.M. Mullis, L. Farrell, R.F. Cochrane, N.J. Adkins, Estimation of cooling rates during close-coupled gas atomization using secondary dendrite arm spacing measurement, Metallurgical and Materials Transactions B: Process Metallurgy and Materials Processing Science 44 (2013) 992–999. https://doi.org/10.1007/s11663-013-9856-2.

[112] X. Liang, E.J. Lavernia, Solidification and microstructure evolution during spray atomization and deposition of Ni3Al, Materials Science and Engineering A 161 (1993) 221–235. https://doi.org/10.1016/0921-5093(93)90517-I.

[113] M.C. Flemings, Solidification processing, Metallurgical Transactions 5 (1974) 2121–2134. https://doi.org/10.1007/BF02643923.

[114] N. Ciftci, N. Ellendt, G. Coulthard, E. Soares Barreto, L. Mädler, V. Uhlenwinkel, Novel Cooling Rate Correlations in Molten Metal Gas Atomization, Metallurgical and Materials Transactions B: Process Metallurgy and Materials Processing Science 50 (2019) 666–677. https://doi.org/10.1007/s11663-019-01508-0.

[115] D. Eskin, Q. Du, D. Ruvalcaba, L. Katgerman, Experimental study of structure formation in binary Al-Cu alloys at different cooling rates, Materials Science and Engineering: A 405 (2005) 1–10. https://doi.org/10.1016/j.msea.2005.05.105.

[116] G.K. Sigworth, Fundamentals of solidification in aluminum castings, International Journal of Metalcasting 8 (2014) 7–20. https://doi.org/10.1007/BF03355567.

[117] Q.G. Wang, Microstructural effects on the tensile and fracture behavior of aluminum casting alloys A356/357, Metall Mater Trans A Phys Metall Mater Sci 34 (2003) 2887–2899. https://doi.org/10.1007/s11661-003-0189-7.

[118] S. Boontein, N. Srisukhumbovornchai, J. Kajornchaiyakul, C. Limmaneevichitr, Reduction in secondary dendrite arm spacing in cast aluminium alloy A356 by Sb addition, International Journal of Cast Metals Research 24 (2011) 108–112. https://doi.org/10.1179/1743133610Y.0000000007.

[119] E. Vandersluis, C. Ravindran, Comparison of Measurement Methods for Secondary Dendrite Arm Spacing, Metallography, Microstructure, and Analysis 6 (2017) 89–94. https://doi.org/10.1007/s13632-016-0331-8.

[120] S. Cegarra, J. Pijuan, M.D. Riera, Cooling Rate Evaluation of Al-4%Cu Alloy Powders During Centrifugal Atomization, in: Euro PM2023 Congress Proceedings, 2023.

[121] P.N. Anyalebechi, Effects of alloying elements and solidification conditions on secondary dendrite arm spacing in aluminum alloys, in: Proceedings of the TMS Fall Extraction and Processing Conference, 2004: pp. 217–233.

[122] ASTM, Standard Test Methods for Determining Average Grain Size 1, n.d. www.astm.org (accessed April 15, 2024).

[123] C.G. Levi, R. Mehrabian, Heat Flow during Rapid Solidification of Undercooled Metal Droplets, Metallurgical and Materials Transactions A 13 (1982) 221–234. https://doi.org/https://doi.org/10.1007/BF02643312.

[124] P.S. Grant, B. Cantor, L. Katgerman, Modelling of droplet dynamic and thermal histories during spray forming-II. Effect of process parameters, Acta Metallurgica Et Materialia 41 (1993) 3109–3118. https://doi.org/10.1016/0956-7151(93)90040-Y.

[125] D. Tourret, G. Reinhart, C.A. Gandin, G.N. Iles, U. Dahlborg, M. Calvo-Dahlborg, C.M. Bao, Gas atomization of Al-Ni powders: Solidification modeling and neutron diffraction analysis, Acta Mater 59 (2011) 6658–6669. https://doi.org/10.1016/j.actamat.2011.07.023.

[126] E.S. Lee, S. Ahn, Solidification progress and heat transfer analysis of gas-atomized alloy droplets during spray forming, Acta Metallurgica Et Materialia 42 (1994) 3231–3243. https://doi.org/10.1016/0956-7151(94)90421-9.

[127] D. Bergmann, U. Fritsching, K. Bauckhage, A mathematical model for cooling and rapid solidification of molten metal droplets, International Jounal of Thermal Sciences 39 (2000) 53–62. https://doi.org/https://doi.org/10.1016/S1290-0729(00)00195-1.

[128] S.K. Pillai, T. Ando, Modeling of the in-flight solidification of droplets produced by the uniform-droplet spray process, International Journal of Thermal Sciences 48 (2009) 1494–1500. https://doi.org/10.1016/j.ijthermalsci.2008.12.011.

[129] D. Liu, J. Zhao, H. Ye, Modeling of the solidification of gas-atomized alloy droplets during spray forming, Materials Science and Engineering: A 372 (2004) 229–234. https://doi.org/10.1016/j.msea.2003.12.041.

[130] A. V. Freyberg, H. Henein, V. Uhlenwinkel, M. Buchholz, Droplet solidification and gas-droplet thermal coupling in the atomization of a Cu-6Sn alloy, Metallurgical and Materials Transactions B: Process Metallurgy and Materials Processing Science 34 (2003) 243–253. https://doi.org/10.1007/s11663-003-0011-3.

[131] A. Prasad, H. Henein, Droplet cooling in atomization sprays, J Mater Sci 43 (2008) 5930–5941. https://doi.org/10.1007/s10853-008-2860-2.

[132] J. Valloton, S. Gawor, H. Henein, Modelling of nucleation in Impulse atomized undercooled droplets, Comput Mater Sci 144 (2018) 176–180. https://doi.org/10.1016/j.commatsci.2017.12.004.

[133] Y. Hu, X. lin Zhou, L. hui Xu, J. hao Li, H. Qi, K. ping Du, Y. Ma, Y. guang Yu, Motion and Solidification Behavior Analysis of Fe-Based Alloy Droplets During Gas Atomization, Metallurgical and Materials Transactions B: Process Metallurgy and Materials Processing Science 51 (2020) 2935–2945. https://doi.org/10.1007/s11663-020-01951-4.

[134] J.B. Wiskel, H. Henein, E. Maire, Solidification Study of Aluminum Alloys using Impulse Atomization: Part I: Heat Transfer Analysis of an Atomized Droplet, Canadian Metallurgical Quarterly 41 (2002) 97–110. https://doi.org/10.1179/cmq.2002.41.1.97.

[135] He Shiwen, Liu Yong, Guo Sheng, Cooling rate calculation of non-equilibrium aluminum alloy powders prepared by gas atomization, Rare Metal Materials and Engineering 38 (2009) 353–356. https://doi.org/10.1605/01.301-0006502464.2009.

[136] R. Mehrabian, S.C. Hsu, C.G. Levi, S. Kou, Rapid Solidification Processing, in: J.J. Burke, R. Mehrabian, V. Weiss (Eds.), Advances in Metal Processing, Plenum Press, New York, 1978: pp. 13–43.

[137] D. Gianoglio, N. Ciftci, S. Armstrong, V. Uhlenwinkel, L. Battezzati, On the Cooling Rate-Microstructure Relationship in Molten Metal Gas Atomization, Metall Mater Trans A Phys Metall Mater Sci 52 (2021) 3750–3758. https://doi.org/10.1007/s11661-021-06325-2.

[138] A. Aissa, M. Abdelouahab, A. Noureddine, M. El Ganaoui, B. Pateyron, B. Pateyron Ranz, by Abderrahmane AISSA, M. EL Ganaoui, Ranz and Marshall Correlations Limits on Heat Flow Between a Sphere and its Surrounding Gas at High Temperature, 19 (2015) 1521–1528. https://doi.org/10.2298/TSCI120912090Aï.

[139] W.E. Ranz, W.R. Marshall, Evaporation from drops: Part I, Chem Eng Prog 48 (1952) 141–146.

[140] S. Whitaker, Forced convection heat transfer correlations for flow in pipes, past flat plates, single cylinders, single spheres, and for flow in packed beds and tube bundles, AIChE Journal 18 (1972) 361–371. https://doi.org/10.1002/aic.690180219.

[141] J.A. Lewis, W.H. Gauvin, Motion of Particles Entrained in a Plasma Jet, AIChE Journal 19 (1973) 982–990. https://doi.org/10.1002/aic.690190515.

[142] J.K. Fiszdon, Melting of powder grains in a plasma flame, Int J Heat Mass Transf 22 (1979) 749–761. https://doi.org/https://doi.org/10.1016/0017-9310(79)90122-4.

[143] N. Ellendt, A.M. Lumanglas, S.I. Moqadam, L. Mädler, A model for the drag and heat transfer of spheres in the laminar regime at high temperature differences, International Journal of Thermal Sciences 133 (2018) 98–105. https://doi.org/10.1016/j.ijthermalsci.2018.07.009.

[144] Z. Duan, B. He, Y. Duan, Sphere Drag and Heat Transfer, Sci Rep 5 (2015). https://doi.org/10.1038/srep12304.

[145] N. Ellendt, R. Schmidt, J. Knabe, H. Henein, V. Uhlenwinkel, Spray deposition using impulse atomization technique, Materials Science and Engineering A 383 (2004) 107–113. https://doi.org/10.1016/j.msea.2004.02.067.

[146] J.B. Wiskel, K. Navel, H. Henein, E. Maire, Solidification study of aluminum alloys using Impulse Atomization: Part II. Effect of cooling rate on microstructure, 2002. https://doi.org/10.1179/cmq.2002.41.2.193.

[147] F. Pengjun, X. Yi, L. Xinggang, C. Ya, Influence of Atomizing Gas and Cooling Rate on Solidification Characterization of Nickel-based Superalloy Powders, Xiyou Jinshu Cailiao Yu Gongcheng/Rare Metal Materials and Engineering 47 (2018) 423–430. https://doi.org/10.1016/s1875-5372(18)30082-1.

[148] R.M. Young, E. Pfender, Nusselt Number Correlations for Heat Transfer to Small Spheres in Thermal Plasma Flows, Plasma Chemistry and Plasma Processing 7 (1987) 211–229. https://doi.org/https://doi.org/10.1007/BF01019179.

[149] D. Poulikakos, J.M. Waldvogel, Heat Transfer and Fluid Dynamics in the Process of Spray Deposition, Adv Heat Transf 28 (1996) 1–74. https://doi.org/10.1016/S0065-2717(08)70139-4.

[150] Y.Y. Zhao, A simplified model for velocity and temperature evolution of alloy droplets in Centrifugal Atomisation and Spray Deposition, Materials Science Forum 475–479 (2005) 4261–4265. https://doi.org/10.4028/0-87849-960-1.4261.

[151] F. Li, Y. Liu, W. Xiao, J. Xie, Simulation of metal droplet events during gas horizontal atomization stage in the spray rolling of 7050 aluminum alloy, Reviews on Advanced Materials Science 33 (2013) 291–297.

[152] Y. Liu, Z. Liu, S. Guo, Y. Du, B. Huang, J. Huang, S. Chen, F. Liu, Amorphous and nanocrystalline Al82Ni10Y8 alloy powder prepared by gas atomization, Intermetallics (Barking) 13 (2005) 393–398. https://doi.org/10.1016/j.intermet.2004.07.026.

[153] M. Yan, J.Q. Wang, G.B. Schaffer, M. Qian, Solidification of nitrogen-atomized Al86Ni6Y 4.5Co2La1.5 metallic glass, J Mater Res 26 (2011) 944–950. https://doi.org/10.1557/jmr.2011.13.

[154] N. Ciftci, N. Yodoshi, S. Armstrong, L. Mädler, V. Uhlenwinkel, Processing soft ferromagnetic metallic glasses: on novel cooling strategies in gas atomization, hydrogen enhancement, and consolidation, J Mater Sci Technol 59 (2020) 26–36. https://doi.org/10.1016/j.jmst.2020.03.077.

[155] B.J. Yang, J.H. Yao, Y.S. Chao, J.Q. Wang, E. Ma, Developing aluminum-based bulk metallic glasses, Philosophical Magazine 90 (2010) 3215–3231. https://doi.org/10.1080/14786435.2010.484401.

[156] J.J. Dunkley, J.D. Palmer, Factors affecting particle size of atomized metal powders, Powder Metallurgy 29 (1986) 287–290. https://doi.org/10.1179/pom.1986.29.4.287.

[157] O.D. Neikov, Atomization and Granulation, in: O.D. Neikov, S.S. Naboychenko, G. Dowson (Eds.), Handbook of Non-Ferrous Metal Powders, First Edition, Elsevier, 2009: pp. 1–620.

[158] O.D. Neikov, Advanced Aluminum Alloy Powders, in: O.D. Neikov, S.S. Naboychenko, G. Dowson (Eds.), Handbook of Non-Ferrous Metal Powders, First Edition, Elsevier, 2009.

[159] Q. Li, Formation of ferromagnetic bulk amorphous Fe40Ni40P14B6 alloys, Mater Lett 60 (2006) 3113–3117. https://doi.org/10.1016/j.matlet.2006.02.054.

[160] A. Castellero, S. Bossuyt, M. Stoica, S. Deledda, J. Eckert, G.Z. Chen, D.J. Fray, A.L. Greer, Improvement of the glass-forming ability of Zr55Cu30Al10Ni5 and Cu47Ti34Zr11Ni8 alloys by electro-deoxidation of the melts, Scr Mater 55 (2006) 87–90. https://doi.org/10.1016/j.scriptamat.2006.03.032.

[161] T. Wayne Wilson, T. Wayne, Trace: Tennessee Research and Creative Exchange Processing, Structure, and Properties of Amorphous Aluminum Alloys Recommended Citation, 2008. http://trace.tennessee.edu/utk_graddiss/354.

[162] I. Otsuka, K. Wada, Y. Maeta, T. Kadomura, M. Yagi, Magnetic properties of Fe-based amorphous powders with high-saturation induction produced by spinning water atomization process (SWAP), IEEE Trans Magn 44 (2008) 3891–3894. https://doi.org/10.1109/TMAG.2008.2002249.

[163] M.G. Ozden, N.A. Morley, Laser additive manufacturing of Fe-based magnetic amorphous alloys, Magnetochemistry 7 (2021) 1–24. https://doi.org/10.3390/magnetochemistry7020020.

[164] W. Wu, X. Li, Q. Liu, J.Y. Hsi Fuh, A. Zheng, Y. Zhou, L. Ren, G. Li, Additive manufacturing of bulk metallic glass: Principles, materials and prospects, Mater Today Adv 16 (2022). https://doi.org/10.1016/j.mtadv.2022.100319.